A study of the reduction and formation of gold nanoparticles in the solid state using mechanochemical aging


A thesis submitted to McGill University
in partial fulfillment of the requirements of the
degree of Master's in Chemistry


by


Austin James Richard


Department of Chemistry

McGill University

Montréal, Québec, Canada

December 2022

# Table of Contents

# Abstract

Gold nanoparticles (AuNPs) synthesized through common solvothermal methods have well studied formation conditions, growth mechanisms, and kinetics. Known for their optical activity, electrical conductivity, chemical inertness, low toxicity, and high surface-to-volume ratio, these characteristics have made AuNPs useful in applications ranging from sensing to drug delivery to catalysis. With many kinds of nanomaterials, mastery over their synthesis has provided precise control over their size, shape, composition, and surface functionalization. However, solvothermal methods for nanoparticle synthesis are troubled by large volumes of liquid waste, energy loss through heating, low yields, and high pH and ion concentration sensitivities. Reactions in the solid state may be achieved through mechanochemistry, a method that has exhibited novel reactivity and advantages such as reduced reaction times, improved selectivities, efficient yields, and reduced chemical waste when compared to select solvothermal routes. Widespread adoption of nanoparticle mechanosynthesis is restricted by our grasp of bottom-up reductive-growth mechanisms and kinetics in the solid state. Following an introductory literature review on mechanochemistry, nanoparticle mechanosynthesis, and chemical aging, this thesis examines the development of a modified solid-state aging-based Turkevich reaction as a model synthesis to study metal-salt reduction and nanoparticle formation in the solid state. By choosing to briefly activate the reaction with mechanical energy and allow the AuNP product to develop in a controlled static environment, the solid-state reduction and formation behaviors were carefully monitored over a period of days to weeks. A general characterization of the aging mechanosynthesis was performed at different aging temperatures and the thermal dependence of reduction and formation was analysed. From the quantization of formation kinetics, an activation energy for the formation of AuNPs in the solid state was calculated. A study of the early reduction period was carried out using electron microscopy and *in situ* elemental analysis techniques. Morphological and chemical compositional changes in the metal-salt precursor were observed, offering a unique perspective on the reactivity of the milled solid and the mobility of precursor species in the solid state.

# Résumé

Les nanoparticules d'or (NPsAu) synthétisées par des méthodes solvothermiques courantes ont des conditions de formation, des mécanismes de croissance, et une cinétique bien étudié. Connu pour leur activité optique, leur conductivité électrique, leur inertie chimique, leur faible toxicité, et leur rapport de superficie à volume élevé, ces caractéristiques ont rendu les NPsAu utiles en applications qui varient de la détection chimique, à l'administration de médicaments, en passant par la catalyse. Pour de nombreux nanomatériaux, la maîtrise de leur synthèse nous a donné un contrôle précis de leur taille, de leur forme, de leur composition, et de leur fonctionnalisation de surface. Cependant, les méthodes solvothermiques pour la synthèse de nanoparticules sont troublées par de grands volumes de déchets liquides, de pertes d'énergie à travers le chauffage, de faibles rendements, et des sensibilités élevées au pH et à la concentration d'ions. Les réactions à l'état solide peuvent être accomplies à travers la mécanochimie, une méthode qui a démontrée de nouvelle réactivité et des avantages telles que des temps de réaction réduits, des meilleures sélectivités chimiques, des meilleurs rendements, et des réductions de déchets chimiques par rapport à certaines voies solvothermiques. L'adoption généralisée de la mécanosynthèse des nanoparticules est limitée par notre compréhension des mécanismes ascendante de croissance réductrice et de la cinétique à l'état solide. Suite à une revue de littérature introductive sur la mécanochimie, la mécanosynthèse des nanoparticules, et le vieillissement chimique, cette thèse examine le développement d'une réaction Turkevich modifiée avec le vieillissement chimique à l'état solide comme synthèse modèle pour étudier la réduction chimique des sels métalliques et la formation de nanoparticules à l'état solide. En choisissant d'activer brièvement la réaction avec l'énergie mécanique et de permettre au produit nanoparticulaire de se développer dans un environnement statique contrôler, les comportements de réduction et de formation à l'état solide ont été soigneusement surveillé sur une période de quelques jours à quelques semaines. Une caractérisation générale de la mécanosynthèse vieillissante a été effectuée à différentes températures de vieillissement et la dépendance thermique de la réduction et de la formation a été analysée. À partir de la quantification de la cinétique de formation, une énergie

d'activation pour la formation des NPsAu à l'état solide a été calculée. Une étude de la période de réduction précoce a été réalisée à l'aide de la microscopie électronique et l'analyse élémental sur place. Des changements morphologiques et compositionnelles du précurseur d'or ont été observés, offrant une perspective unique sur la réactivité de la poudre fraisée et sur la mobilité des espèces précurseurs à l'état solide.

# Acknowledgments

# Contribution of Authors

All sections of this thesis were written and assembled by Austin Richard, unless noted below, with edits and feedback from Dr. Audrey Moores, Dr. Tomislav Friščić, and Dr. Michael Ferguson. All experiments and data analysis were performed by Austin Richard, unless noted below.

Chapter 2

Dr. Ferguson helped perform the triplicate reactions with me by loading and unloading the chilled milling jars. He also performed PXRD analysis while I simultaneously performed the XPS and DRS analyses. Dr. Ferguson also contributed to data presentation and plotting, and to figure design. Dr. Ferguson along with Dr. Titi were responsible for conducting the variable temperature PXRD (VT-PXRD) experiments and the calculation of the activation energy and entropy for gold nanoparticle (AuNP) formation. Dr. Valdez helped with the collection of the STEM data presented in this work. All authors played a role in the editing of the manuscript prepared by me and Dr. Ferguson.

Chapter 3

Dr. Valdez was responsible for operation of the electron microscope in electron energy loss spectroscopy (EELS) experiments. Collection of the EELS data was performed jointly, and I was present to guide the experiment at all times. Dr. Valdez and Dr. Ferguson contributed to data analysis of the elemental maps. Dr. Ferguson also contributed to data plotting and presentation, and to figure design. All authors played a role in the editing of the manuscript prepared by me and Dr. Ferguson.

# List of Figures

# List of Tables

# 1	Introduction

This chapter will lay the groundwork for introducing the motivations, scientific principles, and necessary background for the research presented in the two subsequent chapters. Broadly, the topics covered in this introduction include fundamental principles of mechanochemistry, mechanochemical tools and techniques, comminution for mechanical activation, nanoparticles made by mechanochemistry, and lastly nanoparticle mechanosyntheses that incorporated chemical aging. This chapter should be sufficient to prepare the reader for Chapters 2 and 3, the manuscript-based chapters of this thesis. The underlying rational to the research presented herein stems from a desire to better understand the mechanisms and kinetics that drive solid-state bottom-up nanoparticle mechanosynthesis. Objectives to achieving this goal were two-fold: first develop an aging gold nanoparticle (AuNP) mechanosynthesis that would be used to study solid-state nanoparticle synthesis in detail, and secondly characterize this reaction as much as possible. The bulk of this introduction consists of a comprehensive review of relevant literature centered around themes of mechanical forces and energy, nanoparticles in the solid state, and chemical aging transformations.

## 1.1    An Overview of Mechanochemistry

In mechanochemical reactions, mechanical energy is transformed into chemical energy with which existing bonds are broken and new bonds are formed.[a] Although mechanochemistry is most commonly associated with solids and solid-state reactions, it is possible to use mechanical energy to trigger chemical reactions in liquid or gaseous or mixed state systems as well.[5-7] Mechanochemistry has been recognized as a growing and promising method for synthesizing all kinds of materials including nanomaterials, active pharmaceutical ingredients, co-crystals, biomass-waste-derived products, ceramics, metal alloys, carbon-rich π-conjugated materials,[8] high energy-density materials, and advanced polymers.[9] Mechanochemistry is known to conceivably provide advantages such as reduced reaction times, improved selectivity, higher yields, and reduced chemical waste.[10] Further, mechanochemistry has led to the discovery of alternate reaction pathways and has even achieved reactivity in systems where poor solubility had made chemical reactivity difficult or impossible.[11, 12] Take for example Theophrastus's treatise entitled *On Stones*, a 4th century BCE text popular amongst mechanochemists.[13] Theophrastus described the production of quicksilver (mercury, Hg) from the mixing of cinnabar (mercury(II) sulfide, HgS) and vinegar (aqueous acetic acid) using a copper mortar and pestle. It is now known that the reported mechanochemical reaction was a single displacement reaction that saw mercury (II) sulfide react with copper in an acidic medium to produce liquid mercury and solid copper sulfide (Equation 1.1).[14] This is a mechanochemical pathway to liquid mercury from cinnabar; the thermal decomposition of cinnabar in the presence of oxygen also leads to liquid mercury but with sulfur dioxide gas as a by-product (Equation 1.2).[15] Therefore while both routes produce mercury, the side product species depends on whether the cinnabar is ground or heated in air.

$$HgS_{(s)} + Cu_{(s)} \xrightarrow{\therefore} Hg_{(l)} + CuS_{(s)}$$    **Equation 1.1**[b]

---
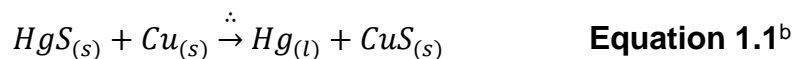
[a] The International Union of Pure and Applied Chemistry (IUPAC) defines a mechanochemical reaction as a "chemical reaction that is induced by the direct absorption of mechanical energy".[1] There are some who prefer a broader definition as to what constitutes a mechanochemical reaction.[2-4]

[b] $\therefore$ is recognized as a symbol denoting a reaction initiated with mechanical energy

$$HgS_{(s)} + O_{2\,(g)} \xrightarrow{T=310\,°C} Hg_{(l)} + SO_{2\,(g)}$$ **Equation 1.2**
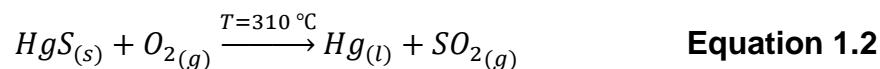
Fullerenes, carbon nanotubes, and graphene/graphite materials have notoriously poor solubility in both organic solvents and water.[16] The dimerization of $C_{60}$ was a sought-after process once-upon a time, though only fullerenes linked by a furan group ($C_{120}O$),[17] a cyclopentane ring ($C_{121}H_2$),[18] or a cyclobutane ring with two oxygen bridges ($C_{120}O_2$)[19] had been found. However, with mechanochemistry Komatsu and co-workers discovered a route to synthesize $C_{120}$ dimers through ball-milling of $C_{60}$ and KCN under solvent-free and air-free conditions (Figure 1.1).[20] These examples demonstrate that mechanochemical reactions can be unique from pathways that use different kinds of energy transformations.



**Figure 1.1** Komatsu and co-workers' proposed reaction mechanism for the formation of the fullerene dimer through neat ball-milling. Reproduced from Ref. 20 with permission from Springer Nature.[20]

There are many devices with which to perform mechanochemical reactions (Figure 1.2). This diversity reflects the different kinds of mechanical forces such as compression, shear, and tensile forces, and the various ways and scales at which those forces can be applied to achieve different chemical transformations.[21] Those devices already mentioned in the examples above, the mortar and pestle, as well as the ball mill, are two of the oldest and most recognizable instruments of mechanochemistry. Nowadays, automated mortar and pestle instruments known as grinder mortars are used to increase the reproducibility and extend grinding time. Vibrational ball mills are devices that uniaxially shake chemical reagent(s) and grinding media together in a milling jar. Grinding media are additive elements used to deliver mechanical energy; grinding media come in various sizes, compositions, and shapes. Vibrational mills are commonly used for many gram-scale laboratory reactions while planetary mills are often used as a kind-of scale-up tool for reactions of tens to hundreds of grams. Planetary ball mills spin milling jars filled with reagent(s) and grinding media around a central axis much like planets orbit the Sun; the central plate is commonly called a Sun wheel. Though by default these devices are manufactured to be operated at room temperature, certain designs or device adaptations

can be made to control the temperature of milling. Vessel jackets with liquid cooling or heating can be fitted to maintain a specific temperature or simply to draw away the heat produced by friction and exothermic reactions. Cryo-mills are specially designed to operate at low temperatures with a built-in fluidic cooling system.



**Figure 1.2** Various mechanochemical devices. (A) Planetary mills (vessels and equipment). (B) Mixer mill (vessels and equipment). (C) Grinder mortar. (D) Drum mill. (E) Cryomill. (F) High energy mill (Emax).[22]

Resonant acoustic mixing (RAM) is a recently introduced mechanochemical technique where the reagent vessel is vibrated at a high frequency, generating heavy frictional forces between particles.[23] Twin-screw extrusion (TSE) is a technique that differs from the mills mentioned so far in that it is a continuous flow technique rather than a batch technique.[24] A twin-screw extruder is a device consisting of two long co-rotating and intermeshing screws that mix and push solid powder from one end to the other. Ultrasonic horns are devices that vibrate a shapely metal piece at ultrasonic frequencies to deliver mechanical energy. Normally employed in solutions and sometimes referred to as sonochemistry, this device induces cavitation bubbles that lead to high energy shock waves upon collapse.[6] Below is included a chart of different mechanical devices that may be seen in laboratory or industrial settings and some comparable characteristics such as the applied mechanical forces generated by each machine, whether the device is capable of batch or flow processing, and the compositions and scales of milling vessels offered for each device (Table 1.1.1).

**Table 1.1** Various mechanical devices and their characteristics.[25-28,c]

| Device Name (ref#) | Operation style | Grinding media? | Applied forces | Material options | Vessel scales | Milling frequency |
|---|---|---|---|---|---|---|
| **Mortar & pestle (25)** | Manual-batch | No | Pressure, friction | Porcelain, agate, glass, $Al_2O_3$, sapphire, polypropylene, | 1.5 – 1900 mL | User-dependent |
| **Vibrational ball mill (25)** | Automated-batch | Yes | Impact, friction | Hardened steel (HS), stainless steel (SS), WC, agate, $ZrO_2$, PTFE, PMMA | 1.5 – 50 mL | 3 – 30 Hz |
| **Planetary mill (25)** | Automated-batch | Yes | Impact, friction | HS, SS, WC, agate, sintered $Al_2O_3$, $Si_3N_4$, $ZrO_2$ | 12 – 500 mL | 30 - 650 $min^{-1}$ |
| **Grinder mortar (25)** | Automated-batch | No | Pressure, friction | HS, SS, WC, agate, sintered $Al_2O_3$, $ZrO_2$, hard porcelain | 700 mL | 100 $min^{-1}$ |
| **Cryo-mill (25)** | Automated-batch | Yes | Impact, friction | HS, SS, $ZrO_2$, PTFE | 5 – 50 mL | 5-30 Hz |
| **Drum mill (25)** | Automated-batch | Yes | Impact, friction | HS, SS | 5 – 43.3 L | 1 - 80 $min^{-1}$ |
| **Resonant acoustic mixer (26)** | Automated-batch | No | Friction | Polypropylene, polyethylene | 4 – 8 oz | 0 - 60 Hz |
| **Twin-screw extruder (27)** | Automated-flow | No | Friction, shearing | SS | 120 – 1000 kg/h | 3 – 37 rpm |
| **Centrifugal mill (25)** | Automated-batch | No | Impact, shearing | SS, titanium | 300 – 4500 mL | 6000 – 23,000 $min^{-1}$ |
| **Knife mill (25)** | Automated-batch | No | Cutting | Holder: autoclavable plastic PC, SS. Blade: SS | 5000 mL | 500 - 4000 $min^{-1}$ |
| **Ultrasonic horn (28)** | Automated-batch/flow | No | Tension, pressure | Horn: SS, titanium, $Al_2O_3$ | N.A. | 15 – 40 kHz |

[c] Note that numerical values were taken from specific company sites for informational purposes and that values may vary between suppliers.

Michael Faraday, best-known for his scientific contributions to the study of electromagnetism and electrochemistry, was by all accounts also a pioneer of mechanochemistry. In 1820, Faraday reported on the successful decomposition of silver chloride by triturating (i.e., grinding) dry silver chloride powder with a pure metal such as zinc, iron, copper, or tin.[29] He was originally attempting to reproduce the decomposition of silver chloride with hydrogen, a reaction previously communicated to him by M. Arfwedson. Only after several unsuccessful experiments with hydrogen as a free-flowing gas and then as a nascent species in solution did he suppose that this reaction may have been caused by something other than hydrogen. While Faraday found that heating the silver chloride with zinc in a glass tube would cause the reaction to proceed, he also found that a room temperature trituration achieved the same result albeit with a strong exothermic effect.

Following Faraday's experiments, mechanochemistry developed into a field of its own with significant technological, scientific, and recognition achievements made throughout the last two centuries.[3] Borchardt and co-workers laid out a timeline of events and noted some of the most important advances such as the invention of the vibrational ball mill, the development of *in situ* X-ray analysis,[30] and the first mechanochemical hydrogenation reaction using nascent hydrogen (Figure 1.3).[31, 32] There are also the many foundational works of M. Carey Lea,[33] W. Spring,[34] Ling & Baker,[35] P. A. Thiessen and P. A. Rebinder.[36] Some of the first meetings of 20th century mechanochemists occurred within the Soviet Union during the late 1960's.[36] After the creation of the International Mechanochemical Association (IMA) in 1984, an organization that would shortly thereafter become an IUPAC affiliate, a fully international conference entitled the International Conference on Mechanochemistry and Mechanical Alloying (INCOME) was held for the first time in 1993.
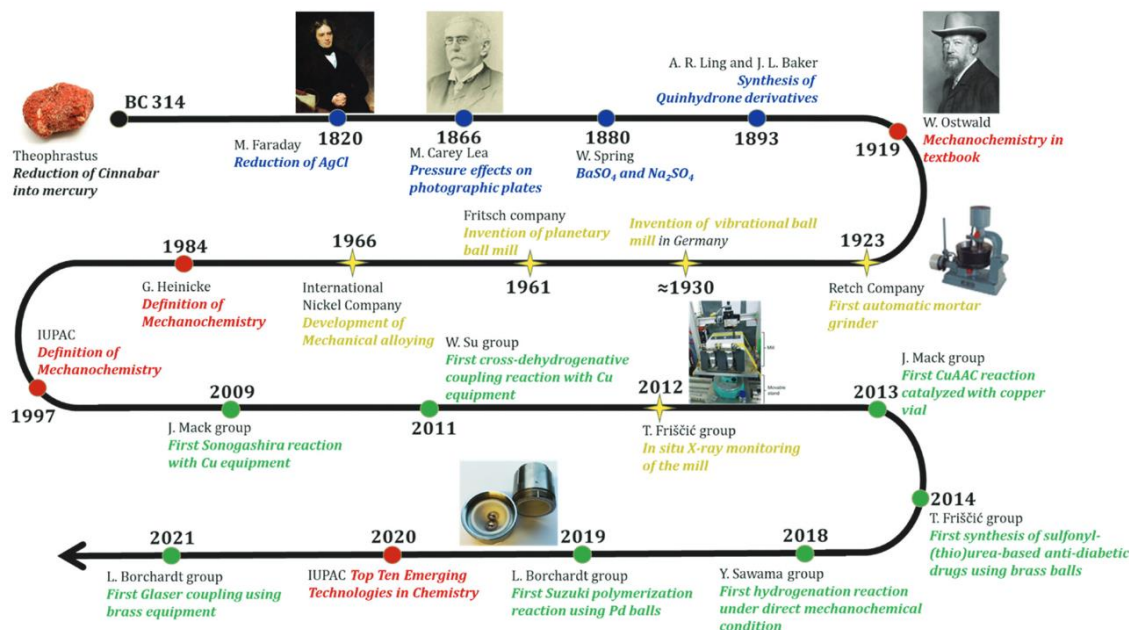
**Figure 1.3** Timeline of mechanochemistry and "direct mechanocatalysis". Blue: pre-modern time; red: important milestones of official recognition for mechanochemistry; yellow: major technological development; green: first reports of specific direct mechanocatalytic reactions. Reproduced with permission from the Royal Society of Chemistry.[32]

Although Faraday did not comment directly on the use of mechanical energy in 1820, a decade later he wrote on comminution: i.e., the process of breaking up solid bits of matter into smaller fractions. He wrote, "*No merely mechanical division can bring a solid body into a state, comparable as to physical properties, with the same body when it has had freedom of motion given to its particles by fusion or solution.*" (page 144).[37] In essence, a solid that has been melted or dissolved will not have the same properties or behavior as if that solid were finely divided into an enormously large number of tiny solid units. This writing was insightful and raised questions as to what reaction parameters and system properties may hold different importance in the solid state compared to solution. For example, variables such as pH, solution density, and solution concentration are important solution properties that have no direct analogue in solid mixtures. In solution a solute is said to be homogenously dispersed in a solvent, whereas a mixture of two solids is imperfectly dispersed due to the limited freedom of motion in the solid state.[d] There may

---

[d] Solid solutions such as bulk metal alloys did at one time have the freedom of motion to homogeneously mix as liquids, before resolidifying below the new material's melting point. Here we are considering the mixing of two or more solids while in the solid state.

be localized regions of a solid with a higher concentration of one substance than another, resulting in a density that varies locally in space as well. Consequently, because pH is defined using the concentration of hydronium ions in solution, there is no solid-state pH of which to speak.[38] In a mechanochemist's repertoire the set of parameters for a solid-state system may share some general elements with solution chemistry. Other elements, however, appear unique to mechanochemistry. The remainder of Section 1.1 is dedicated to discussing mechanochemical techniques in detail with accompanying literature examples.

Liquid-assisted grinding (LAG) is a unique mechanochemical reaction technique whereby a small amount of a liquid is introduced to a milling vessel with the solid materials.[39, 40] The amount of the liquid additive in a mechanochemical system is described by the parameter $\eta$, which I defined as the ratio of solvent volume to solid mass, often in µL/mg.[41] If there is no added liquid, then the reaction is said to be a 'neat grind'. The LAG range of η-values is mostly accepted to fall between 0.1 – 1 or 0.1 – 2 µL/mg, anywhere beyond that is said to be a slurry until about 10 or 12 µL/mg where the system behaves like a homogenous solution.[41, 42] Jones and co-workers discovered that anthranilic acid (AA) could selectively interconvert between different polymeric forms when ground either neatly or with different LAG additives, depending on the starting polymorph (Figure 1.4).[43] The interconversion of the three different forms of AA was performed through mechanical grinding at 30 Hz over 60 minutes. The conversion to AA III was historically only reported from either sublimation or from the melt, both of which are high temperature processes beyond 140 °C.[44] When performed mechanochemically with either neat or LAG grinding from polymorphs AA I or AA II respectively, room temperature operation was sufficient to achieve significant conversion to AA III as measured by powder X-ray diffraction (PXRD).
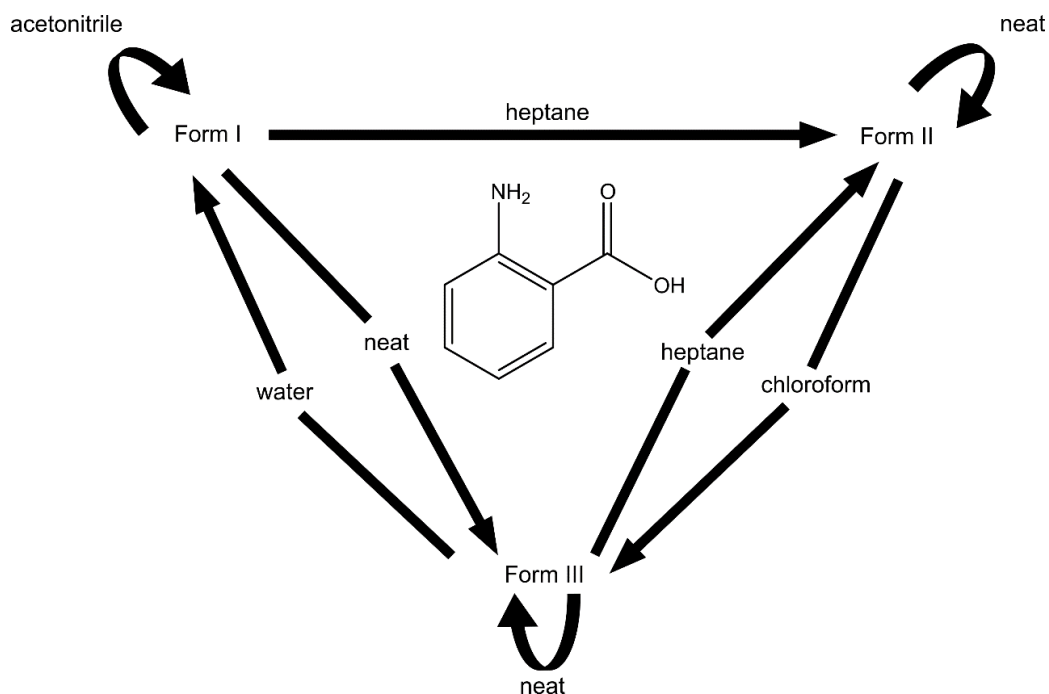
**Figure 1.4** Summary of observed polymorph transformations among three AA crystal forms via LAG. Adapted from Ref. 43 with permission from the Royal Society of Chemistry.[43]

Hardacre and co-workers used LAG to phosphitylate nucleosides and 2-deoxynucleosides with a few different chlorophosphoramidites, reagents that are known to have stability and solubility issues.[45] Though previous work from several of the same authors had shown that the use of ionic liquids (ILs) could aid in the room temperature preparation of moisture sensitive chlorophosphoramidites,[46] this new work took the logical next step of using ILs as stabilizing solvent additives in LAG reactions. The mechanochemical process helped to overcome the low solubility of the reagent materials in dichloromethane (DCM) and various ILs, increasing the percent yield in one instance by 25% and in another by 67%.

Mechanical energy is a distinctive form of energy that may be transferred through the momentum of grinding media, the vibration of ultrasonic waves, the compression between surfaces, the tension from a cantilever, etc., and may be applied across broad energy ranges and size scales. Diamond anvil cells (DACs) are used to study phase changes and chemical changes of substances under extremely high pressures, in excess of 10 GPa.[47, 48] Single molecule mechanochemistry encompasses experiments on a small force scale, generally using an atomic force microscopy (AFM) cantilever tip to study the

mechanical properties of inter and intra molecular bonds.[49] For example, Xia and co-workers used single molecule force spectroscopy (SMFS) to characterize the force–extension behavior and measure the threshold forces of multicyclic mechanophores (Figure 1.5).[50]
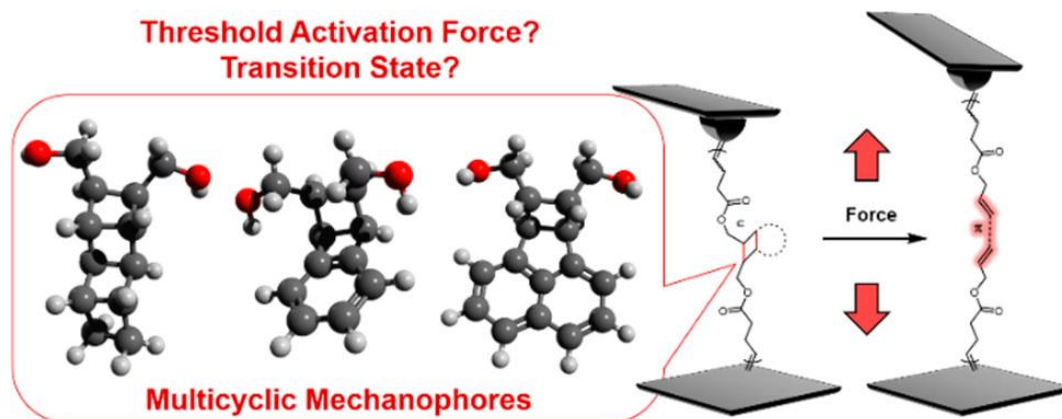


**Figure 1.5** Abstract figure for the paper of Xia and co-workers depicting a single molecule attached to a substrate and cantilever tip being stretched through a stereochemical transition. Reprinted with permission from Ref. 50. Copyright 2021 American Chemical Society.[50]

There have been efforts to use computational tools such as density functional theory (DFT) and molecular dynamics (MD), in combination with experimental work, to model and compute energies and kinetics of mechanochemical systems.[51, 52] Yan and co-workers modelled the decomposition of many chlorinated, brominated, and fluorinated persistent organic pollutants (POPs) via mechanochemistry.[53] By summarizing multiple milling parameters into a single total effective impact energy, they successfully predicted reaction rates for different operating conditions if given a known reagent ratio. Tysoe and co-workers investigated sliding solid-solid interfaces and their ability to accelerate mechanochemical reactions.[54] The group studied the shear-induced rate of methane formation from the decomposition of adsorbed methyl thiolate species on copper in ultrahigh vacuum (UHV). Through DFT, changes in the activation barrier were calculated as a function of force. MD simulations revealed that only a small proportion of the adsorbed thiolates experienced sufficiently high forces as to reduce the activation barrier.

Fiss *et al.* calculated real energy-draw and mass intensity (total mass of process / total mass of product) metrics, comparing hydrogen evolution reaction (HER) capabilities of photo-catalysts made by mechanochemistry and those made via thermal pathways. In

one instance, the group developed a milder and lower temperature approach for the synthesis of catalytically active graphitic phosphorus-linked triazine network (g-PCN) materials.[55] A room-temperature mechanochemical reaction of sodium phosphide and cyanuric chloride was combined with a 1 hour annealing of the milled material at 300 °C. In photo-catalytic water-splitting experiments, the energy draw was improved from 1.87 kWh g$^{-1}$ to 1.07 kWh g$^{-1}$, a reduction of 43% over the hotter and longer furnace method.

In a separate work, the group used sodium phosphide as a phosphorus source to mechanochemically synthesize ultrasmall nickel phosphide nanoparticles, used to catalyze HER while mounted onto a graphitic carbon nitride (g-CN) support (Figure 1.6).[56] This mechanochemical approach afforded mass intensity values over 2.5 times lower and an energy demand decrease of 2.4 – 18.6 times that of cited thermal decomposition processes. Fortunately, scaling the reaction up from roughly 0.3 to 2.5 g in a planetary mill resulted in an even better mass intensity, 3 times lower than the traditional methods.



**Figure 1.6** Abstract figure for the mechanosynthesis of nickel phosphide nanoparticles and the HER catalyzation application. Reprinted with permission from Ref. 56. Copyright 2020 American Chemical Society.[56]

Mack and Andersen investigated the relationship between mechanical energy and thermal energy using the reduction of 4-tert-butylcyclohexanone as a model system.[57] They studied the ability of these different energy types to influence the diastereomeric product selectivity. Milling frequencies of 12, 15, 18, and 21 Hz were used in conjunction with milling temperatures of -6, 7, 13, 23, and 39 °C (Figure 1.7). It was found that at the high and low temperature extremes there was little to no mechanochemical influence on

the selectivity, being almost completely dictated by the thermal energy. However, between these extremes the variable use of mechanical energy through different milling frequencies had a strong effect on the diastereomer selectivity, up to a 20% difference at 13 °C. It was found that the higher milling frequencies tended to reduce the selectivity of the product. The group proposed three different possibilities as to why this phenomenon was observed. First, the higher milling speeds took advantage of the exothermic character of the reaction and increased the thermal energy from reaction. However, external temperature measurements of the jars at different milling frequencies did not show any notable variation. Second, the act of milling could have altered the rheological properties of the material enough as to cause small changes in the energetics of the mechanochemical environment. This effect has been previously reported on by James and co-workers, who used a model Knoevenagel reaction to investigate sigmoidal feedback kinetics observed in mechanochemical reactions.[58] The rheological principle being that the milling process progressively affects the material such that its physical properties are altered to favour further reaction progression. The final proposal made to explain the mechanochemical influence on diastereomer selectivity was if higher frequencies imparted more energy, thus lowering stereoselectivity. Though no definitive answer was given, the impact that mechanical energy had on selectivity was undeniable and showed that the two forms of energy are not interchangeable.
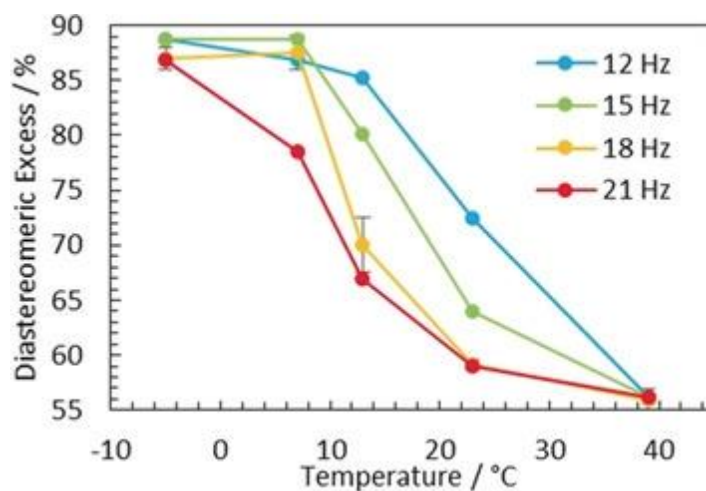


**Figure 1.7** Effect of varying milling frequency and milling temperature on the diastereomeric product selectivity from the reduction of 4-tert-butylcyclohexanone. Reproduced from Ref. 57 with permission from John Wiley and Sons.[57]

Hernández and co-workers studied the cooperative use of mechanical and electromagnetic energy, having chosen the photocatalyzed borylation of aryldiazonium salts as a model system.[59] This system had been previously studied in a MeCN solution by Yan and co-workers.[60] Hernández sought to reproduce those results under solid state conditions, by using a transparent polymethyl methacrylate (PMMA) milling jar to allow light from coiled light-emitting diodes (LEDs) to reach the reactants in the jar (Figure 1.8). An equimolar mixture of benzenediazonium tetrafluoroborate and bis(pinacolato)diboron (B$_2$pin$_2$), with the photocatalyst eosin Y (5.0 mol%) was milled for 2 h at 25 Hz. Hernández found that the reaction was optimal when milling and light were used synergistically and not in sequence or individually. Using proton nuclear magnetic resonance ($^1$H NMR) and Fourier-transform infrared (FTIR) spectroscopy, the amount of borylated product to aryldiazonium salt was recorded. Milling in opaque Teflon$^{TM}$ jars, or even under ambient light in PMMA jars, did not induce any measurable reaction. Milling with LEDs but without the eosin Y photocatalyst also did not produce a reaction. These controls proved that a sole mechanochemical, photolytic, or thermal pathway was not feasible. In one experiment, a pre-milled mixture of reactants was subsequently irradiated with LED light. While this did produce some borylated product (6%), this conversion paled in comparison to the conversion achieved when the two energy inputs were used synergistically (85%).
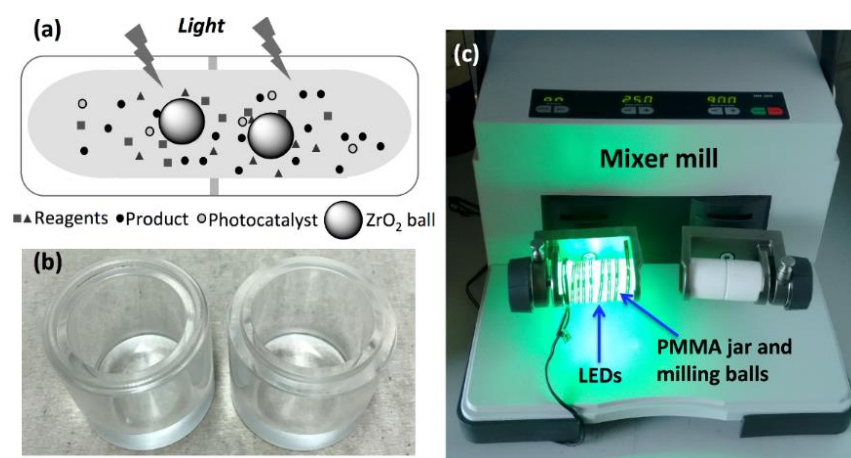


**Figure 1.8** (a) Cartoon representing the merging of light and mechanical energy. (b) 25 mL transparent PMMA milling jar. (c) Experimental setup for simultaneous photo- and mechanical-activation with an external light source. Reproduced from Ref. 59 with permission from the Beilstein-Institut.[59]

Mechanochemistry encourages the exploitation of the reaction vessel, specifically the material of which the vessel is made. While much of solution chemistry is run with

glassware, an impact-frail material not suitable for mechanical processes, the vessels of mechanochemistry are often made of metals, ceramics, or plastics. Some common vessel and grinding media materials include agate, stainless steel, zirconium oxide, aluminum oxide, polytetrafluoroethylene, polymethyl methacrylate, and tungsten carbide. Material property considerations include hardness, optical transparency, resistance to corrosive agents and solvents, and chemical inertness. A harder vessel material will result in a higher impact-force during milling, increasing the deformation and comminution capabilities. A transparent vessel may allow for cooperative photo-mechano-reactions and enables *in situ* analysis with techniques such as Raman,[61] or synchrotron powder X-ray diffraction (PXRD).[30] Some reactions employ or produce chemical agents that may react aggressively with certain jar materials. To not endanger the integrity vessel and grinding media, it may be important to select a material that is compatible and chemically inert with all chemical species involved. Because milling and grinding naturally involve wear and abrasion, vessel and grinding media material may contaminate a sample. Contamination may worsen the longer the milling time and the higher the milling frequency. If certain kinds of contamination, say metal contamination, are undesirable then it may be sensible to select a ceramic or plastic vessel.

The geometric design of the reaction vessel and grinding media play an important role as well. Traditional designs of vibrational mill jars include dome-capped cylinders for the vessels and spheres for the grinding media; planetary mills commonly utilize cylindrically shaped milling vessels. Simulated and experimental variations on the size and shape of these tools have been shown to affect the resulting particle size and the energy exchange efficiency. For example, de Camargo and co-workers demonstrated that the size and shape of grinding media in wet grinding planetary mill operation influenced the average size and size distribution of the milled solid.[62] On size, they found that smaller media produced smaller milled particles, provided there is still sufficient kinetic energy in the grinding media to comminute the solid material. On shape, they found that cylindrical media produced a coarser powder with a narrower distribution, while spherical media led to smaller particle sizes. Furthermore, D'Incau and co-workers modelled different jar designs for planetary mill reaction vessels.[63] They redesigned the

classic cylindrical shape into a half-moon geometry by adding a flat wall down the axis of the cylinder. It was found that this new geometry increased the number of high-velocity collisions, generating a more uniform and finer end-product; however, experimental PXRD analysis of the average crystallite size and defect content showed that the classic cylindrical design, under optimal conditions, produced more defects in a homogeneously ground powder and globally exchanged more energy from media to powder.

Milling vessels may be designed to allow for gas exchange. In that context, Schüth and co-workers used a modified ball mill with a gas inlet and outlet to run a continuously flowing gas into and out of an operational ball mill (Figure 1.9).[64] The goal of this setup was to mechanochemically selectively oxidize CO to $CO_2$ from a gas mixture of 1 % CO, 1 % $O_2$, 50 % $H_2$, and 48 % $N_2$ using a milled Cu and $Cr_2O_3$ based CO oxidation catalyst: under mechanochemical conditions, selectivities beyond 95% were achieved.
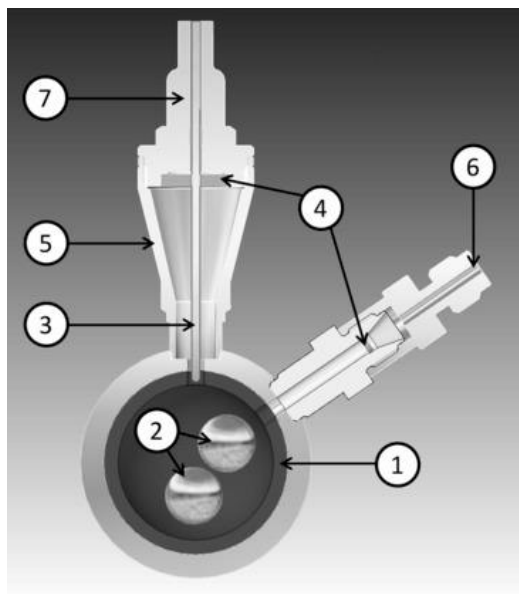


**Figure 1.9** Modified milling vial: (1) inner wall made of tungsten carbide, (2) 10 mm tungsten carbide milling balls, (3) thermocouple, (4) frits, (5) funnel, (6) gas inlet with 3 mm Swagelok connection, (7) gas outlet with 3 mm Swagelok connection (located behind picture plane). Reproduced from Ref. 64 with permission from John Wiley and Sons.[64]

It is important to consider the filling ratio, expressed as the total volume of reagent solids divided by the total volume of the grinding media. In the case where grinding media were absent, filling ratio is defined as the volume of solid reagents to the volume of the vessel. Filling ratios that are both too small or too large can have negative impacts on the

efficiency of the chemical reaction and/or on the integrity of the milling vessel. Burmeister and co-workers used the Knoevenagel condensation of barbituric acid and vanillin as a model reaction and varied, the volume of their spherical grinding media, the volume fraction of grinding media, and the material of the media.[65] It was found that the time to achieve nearly complete conversion as a function of ball volume fraction, was optimized between 0.26−0.30 and that a ball volume fraction too high or too low was suboptimal (Figure 1.10).
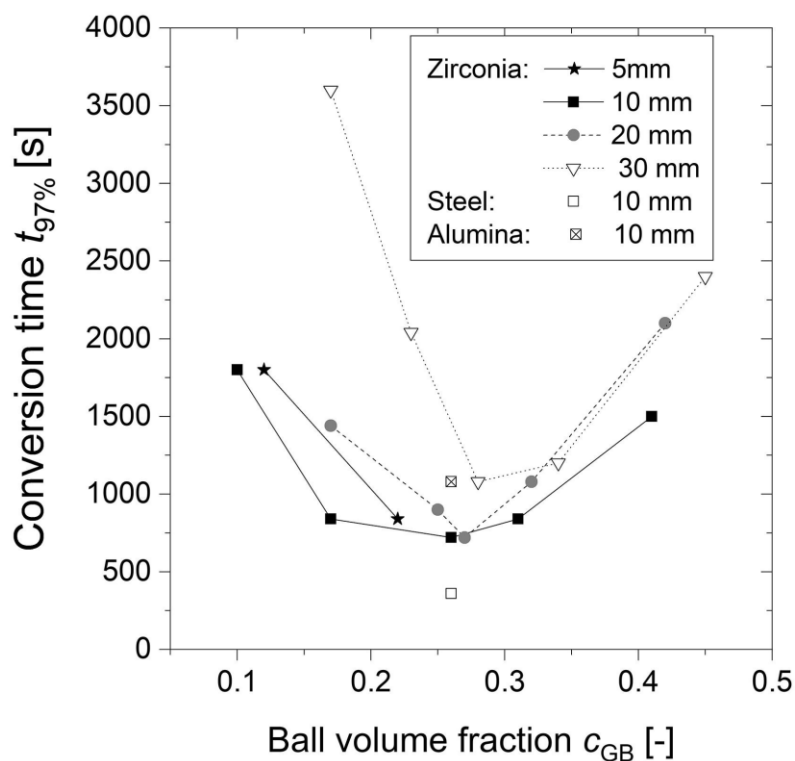


**Figure 1.10** Conversion time $t_{97\%}$ to reach full conversion as a function of ball volume fraction for varied ball sizes. This figure was published in Ref. 65, Copyright Elsevier 2020.[65]

The parameters discussed above will affect the comminution process. The choices made by a mechanochemist are reflected in the resulting degree of mixing, the particle size lower limit, the solid texture and consistency, the total available surface area and the total system energy, the number of crystal defects and the degree of amorphization. These are important considerations that influence the reactivity of a solid state mechanochemical system. In this next section these effects of comminution will be discussed in more detail and the concept of mechanical activation will be explored as it relates to the comminution of solid material.

## 1.2    Comminution Effects and Mechanical Activation

Comminution, the process of using mechanical energy to fragment solids, has always been and remains a very important part of solid-state mechanochemistry. Faraday said as much when he wrote that "*The division of matter is often highly advantageous in facilitating chemical action…*" (page 144).[37] Some of the earliest work with high-energy mills was performed in the mining and metallurgy fields where the comminution of large ore chunks and the mechanical mixing of different metals was heavily studied.[66-68]  For example, ultrafine milling with an attritor mill was used in the recovery of microscopic refractory gold ores encapsulated by sulfides.[69] High energy ball-milling was also employed to cold-weld mixtures of nickel and chromium powder, thorium and yttrium oxides, and a Ni-Al-Ti master alloy, producing a nickel-base superalloy that combined fine particle dispersion strengthening and age hardening.[70] The latter example of cold-welding is also known as mechanochemical alloying, a solid-state process whereby different powders are milled to create a new composite powder made of composite particles.[71]

Mathematical models for comminution theory have been developed that analyze the probability of a breakage event, given a particle of some starting size, and the resulting distribution of fragment sizes and imparted mechanical energy.[72, 73] That probability of breakage is dependent upon the binding strength of the target particle, the total mechanical energy available to cause breakage, and the size of the particle relative to the size of the grinding media. For breakage to occur, the total mechanical energy must exceed the binding strength of the particle. Figure 1.11 presents an illustration of how a feed of N particles of varying sizes will break given N number of breakage events. Interestingly, even after an impractically long milling time the lower particle size will always reach a plateau below which the grinding media are ineffective at further comminution.
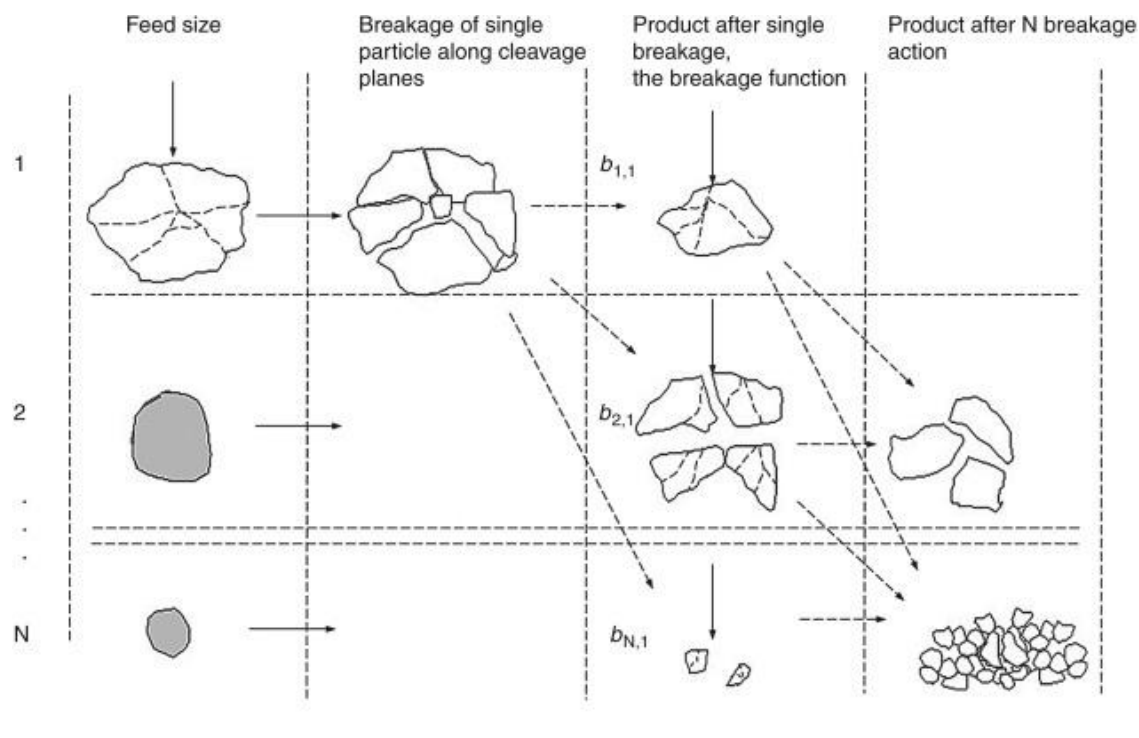
**Figure 1.11** Representation of the distribution of particles after breakage. Solid arrows represent the applied force for breakage and dotted arrows indicate the distribution of fragments of breakage to the same or lower sizes. The fragments shown represent breakage of an original single size particle. This figure was published in Ref. 72, Copyright Elsevier 2016.[72]

Smaller particles are less likely to experience breakage events because they are less likely to be hit and contain fewer, shorter cracks.[74] Moreover, small particles that are products of breakage events tend to have increased strength owing to the formation of structural defects and high-stress grain boundaries, thus increasing the internal binding strength of the particle. Large particles are more likely to be hit and broken apart because of their larger cross-sectional area, more deformable surfaces, and weak cleavage planes. Particles have both an internal binding energy and a surface energy; when a particle is given enough energy to overcome its internal binding energy it will break and create fragments with new surfaces, increasing the total surface energy of the system.

Researchers have modelled the way the ballistic energy is delivered during a collision event involving a crystalline material. It is distributed amongst different components where the proportional value for each component may depend on the milling conditions and the type of crystal being milled.[75] There is the energy used to overcome the internal binding energy of the original particle, the energy converted to heat and lost

from friction, the energy maintained by the object that contacted the particle, the energies of the new surfaces and the new internal energies of the fragments. Some of this new energy acquired by the fragmentation products is used in deformative processes, both elastic and plastic. Elastic deformation will reversibly stretch a material but will not cause a permanent rupture, while plastic deformation causes irreversible damage beyond the point of recovery: these deformative processes induce strain, crystal defects, and amorphization.[e,f] Amorphization is the disruption of long-range crystalline order through the production of short-range disorder, metastable regions of the crystal where atoms have been moved from their ideal configuration. Crystal defects are interruptions in the perfect ordering of a crystal, they are diverse and may occur as point, line, or surface features. These imperfections can exist both internally, and on the surface where they increase the internal stress and surface energy respectively.

Among different types of defects, there are vacancies and interstitial atoms, where atoms are either missing or squeezed into an irregular position (Figure 1.12a,b). Furthermore, there are small and large substitutions where an atom has been replaced with another atom of a different size (Figure 1.12c,d). A Frenkel defect is the jumping of an ion from a regular site to an interstitial site, creating a vacancy and interstitial atom pair (Figure 1.12e). A Schottky defect is a unique defect to ionic crystals where a stoichiometric number of cations and anions are absent from their regular atomic positions (Figure 1.12f). There are one-dimensional (1D) defects known as dislocations or line defects. There are two kinds of basic line defects: edge and screw dislocations (Figure 1.13a,b). An edge dislocation can be understood as the partial insertion of an extra plane of atoms along an axis that becomes the dislocation line. A screw dislocation can be described as the skewing of a partially cut crystal by shear, such that the planes along the dislocation line are one unit apart. Both defects can be mathematically understood using a Burgers vector b, shown in Figure 1.13a and Figure 1.13b, a special

---

[e] Irreversible deformations are only permanent so long as no changes to the system are applied. Increasing the temperature for example would induce annealing, allowing atoms in defective positions to reorder themselves.

[f] Elastic deformation may create or rearrange defects without rupturing the material. Plastic deformation occurs when the concentration and magnitude of defects is strong enough to create microcracks or tears in the material.

loop around the crystal that begins and ends in the same x-y position. A perfect crystal would follow a symmetrical loop no matter how you look at it, however a Burgers vector loses symmetry along at least one angle of view. Grain boundaries are 2D defects that consist of high-stress surfaces between crystallites of different orientations (Figure 1.13c). Twin boundaries are a special case of grain boundary where the two adjacent orientations are mirror planes of one-another (Figure 1.13d). There are also stacking faults, 2D plane patterning defects that are commonly found in FCC metals (Figure 1.13e). The regular FCC patterning of ABC planes may be interrupted by an HCP AB patterning. Crystal defects can be dynamic and may move under conditions such as externally applied stress and high surrounding temperatures. For example, an edge dislocation can be pushed from the inside of a crystal to the surface by means of a shear stress (Figure 1.14).
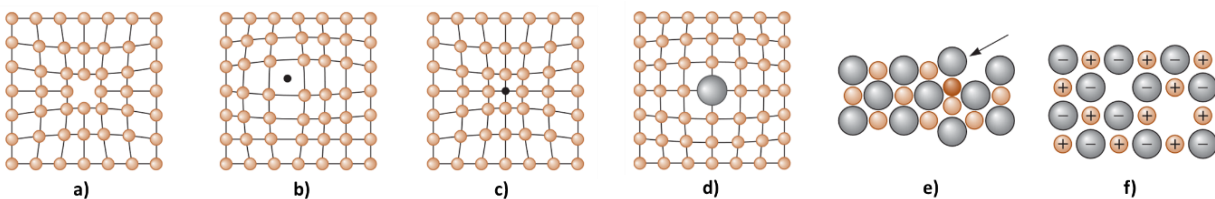


**Figure 1.12** A variety of 0D point defects: (a) vacancy, (b) interstitial atom, (c) small substitutional atom, (d) large substitutional atom, (e) Frenkel defect, and (f) Schottky defect. Cengage Learning Inc. Reproduced by permission. www.cengage.com/permissions.[76]
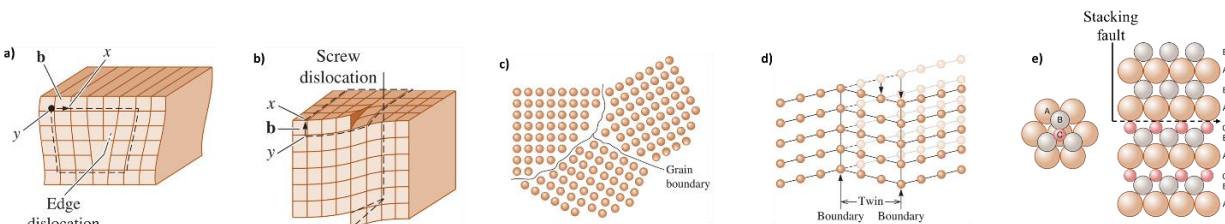


**Figure 1.13** (a-b) 1D crystal defects known as screw and edge dislocations. A Burgers vector b is required to close a loop of equal atom spacings around the dislocation. (c) A 2D surface defect known as a grain boundary defines a change in crystal orientation. (d) A twin boundary is a special case of boundary where adjacent grains have symmetrical orientations as defined by a mirror plane. (e) A stacking fault is an interruption of the regular patterning of planes from one sequence to another. Cengage Learning Inc. Reproduced by permission. www.cengage.com/permissions.[76]
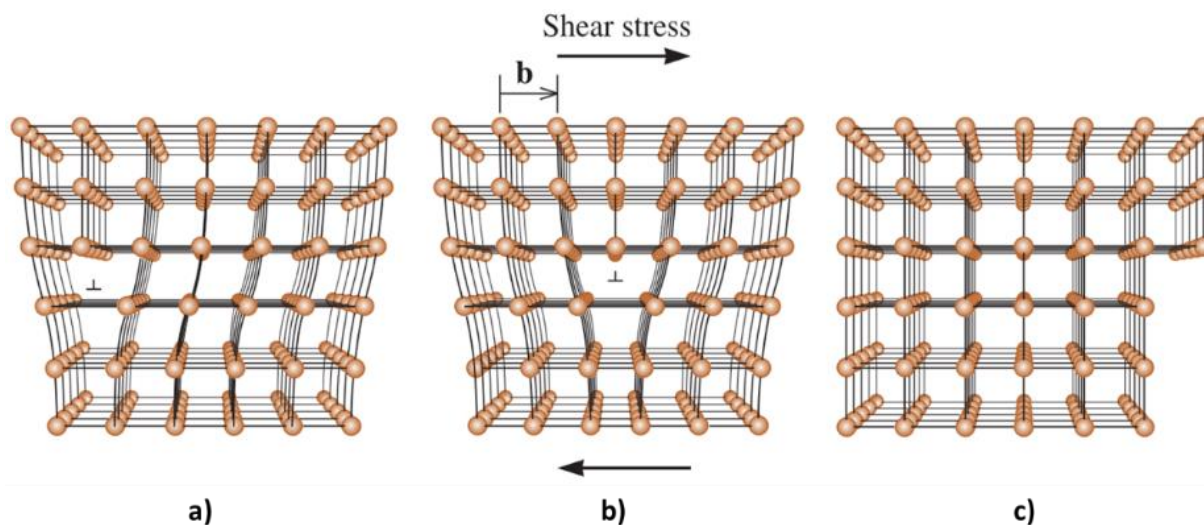
**Figure 1.14** A shear stress is applied to the dislocation in (a), the atoms are displaced, causing the dislocation to move one Burgers vector in the slip direction (b). Continued movement of the dislocation eventually creates a step (c), and the crystal is deformed. Cengage Learning Inc. Reproduced by permission. www.cengage.com/permissions.[76]

Comminution facilitates chemical action, in part because it increases the total available surface area and total surface energy, values which are positively correlated to reactivity.[77] Regions with surface defects and surface strain may even act as catalytic centers for promoting reactivity. From the molecular perspective, it is known that the internal energy of a molecular species may be destabilized upon introduction of strain. Gilman presented a simple Walsh diagram of a triatomic molecule to explain this concept of strain-induced destabilization, and likened it to a reverse Jahn-Teller effect.[g, 78] When the linear structure of this molecule is bent with strain, the gap between the HOMO and LUMO states is diminished and results in a less stable molecule with a higher reactivity.

A 2015 review by Bickelhaupt and Wolters argued how the activation strain model could be used to model chemical reactivity of molecules. In the activation strain model the change in total energy ($\mathit{\Delta E}$) of a chemical system is viewed as a sum of the change in molecular strain ($\mathit{\Delta E}_{strain}$) and the change in chemical interactions ($\mathit{\Delta E}_{int}$).[79] Briefly,

---

[g] The Jahn-Teller effect is the energetically favourable distortion of mostly transition metal coordination complexes. The lower overall electronic energy of the metal's valence electrons may prompt a spontaneous distortion of the coordination polyhedron, depending on the filling of the valence orbital and the net spin of the electrons. An inverse Jahn-Teller effect implies that rather than a spontaneous electronic state change causing crystal deformation, the mechanical deformation of a crystal will induce a change in the electronic energy states.

$\mathit{\Delta E}_{strain}$ is the destabilizing energy that must be overcome to geometrically deform a reference geometry to some transition state geometry. $\mathit{\Delta E}_{int}$ is the stabilizing energy from all chemical interactions that arise when the structurally deformed reactants are brought from infinity to their positions in the transition state geometry. This model was used to analyse the oxidative addition of a methane C–H bond onto a palladium catalyst that was either uncoordinated, coordinated with one ligand, or coordinated with two identical ligands (Figure 1.15). As the reaction progresses through stretching of the C–H bond, the amount of strain that must be overcome to deform the reference geometry increases with metal center coordination. This is logical, at first the only deformation is that of the C–H bond but as ligands are coordinated to the metal center there are additional deformation owing to the ligand to metal bond(s). Further, these ligand deformations can be viewed using molecular orbital theory by analyzing the HOMO-LUMO states of the Pd-PH$_3$ bond.
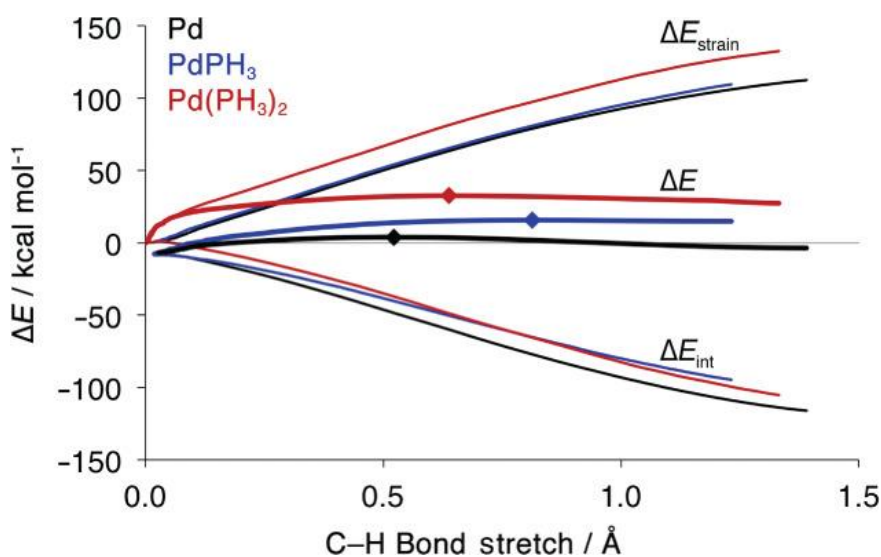


**Figure 1.15** Activation strain analyses for the oxidative addition of methane to Pd (black), PdPH$_3$ (blue), and Pd(PH$_3$)$_2$ (red). A dot designates a transition state. Energies and bond stretch are relative to reactants. Reproduced from Ref. 79 with permission from John Wiley and Sons.[79]

In solids, rather than discuss HOMO-LUMO gaps it is common to discuss energy states using band theory, where an equivalent energy gap is known as a band gap. Gilman also presented a general qualitative analysis of the effect that shear-strain has on the band gap in solids.[80] Using a simple two-dimensional square lattice and the nearly-free-electron approximation, he demonstrated that a sheared lattice with a minimum band

gap of $E_g$ will acquire a new minimum band gap of $E_g^*$ upon shear deformation (Figure 1.16).
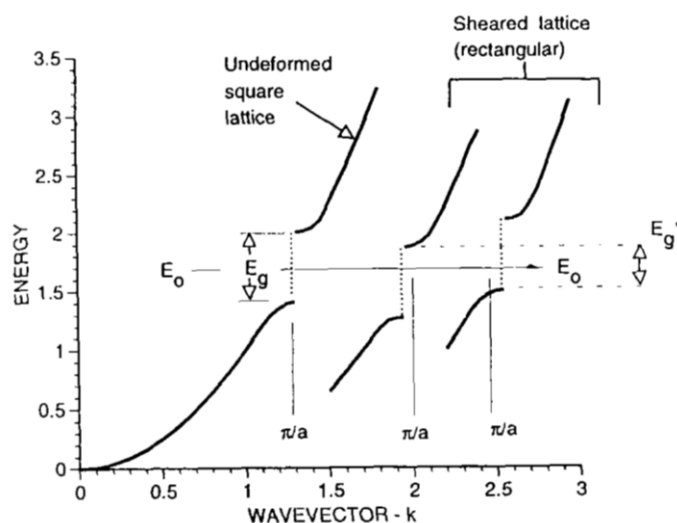


**Figure 1.16** A band diagram showing that shear reduces the minimum [indirect] band gap in the nearly-free-electron approximation. $E_o$ is the mid-point of the gap, $E_g$ is the undeformed gap energy, and $E_g^*$ is the shear-strained gap energy. Reproduced from Ref. 80 with permission from Springer Nature.[80]

These phenomena have been observed in many mechanically driven chemical systems and form the basis for what has come to be known as mechanical activation.[81-83] Mechanical activation is described as a mechanical treatment, whereby a reactant or a reaction mixture is exposed to mechanical energy in a fashion that aims to help with subsequent transformation but is not solely responsible for said chemical change. Mechanical activation can exhibit a catalyst-like effect that lowers the activation energy to reaction. To achieve conversion from reactants to products, either the activation energy demand must be met, or the activation energy barrier must be lowered such that the available ambient energy is enough to cause the reaction to proceed spontaneously. The latter condition elucidates the motivation behind the use of catalysts, substances that increase the rate of reaction ($\kappa$) by lowering the activation energy ($E_A$); the catalytic effect can be understood from the Arrhenius relationship in equation 3. A simple reaction profile diagram in Figure 1.17 displays the activation energies for catalyzed and uncatalyzed systems.

$$\kappa(T) = A\,exp(\frac{-E_A}{k_B T}) \tag{3}$$

23
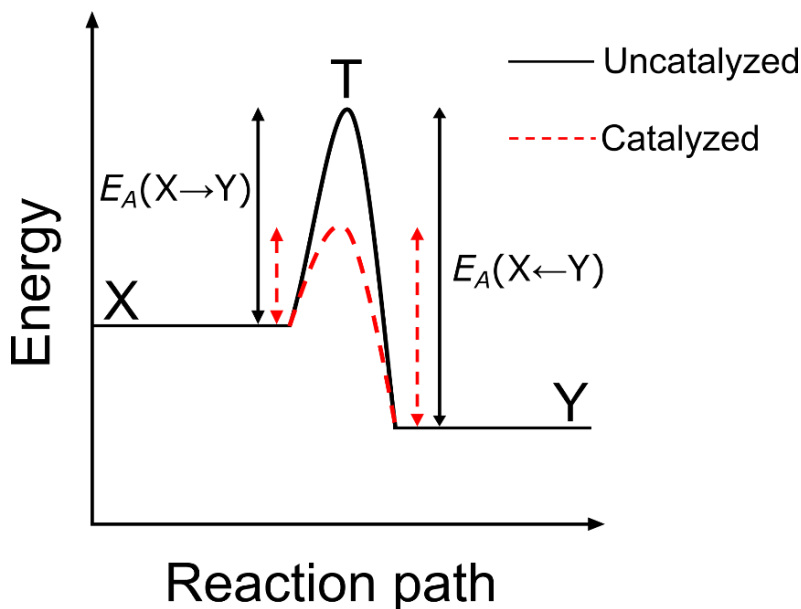
**Figure 1.17** A reaction profile diagram showing the activation energy ($E_A$) of uncatalyzed (smooth black) and catalyzed (dashed red) systems. Reactants (X) with enough energy are excited to a transition state (T) and then relax to products (Y).

Mechanical activation has been described as an energy input followed by prolonged energy damping, in what are viewed as distinct dynamic and static periods of activation, respectively (Figure 1.18).[84] In the dynamic period, the total mechanical energy and the entropy both increase; however, once milling reaches its lowest affectable size limit agglomeration may begin to take place. Highly excited short-lived ($10^{-7}$ to $10^{-3}$ s) states created in the dynamic period are quickly lost as soon as the mechanical action is halted. Metastable states with longer lifespans ($10^{-3}$ to $10^6$ s) will persist into the static period and dissipate at rates dependent on the material specific properties. This energy input can fundamentally change the mechanical, thermal, and other properties of a material.
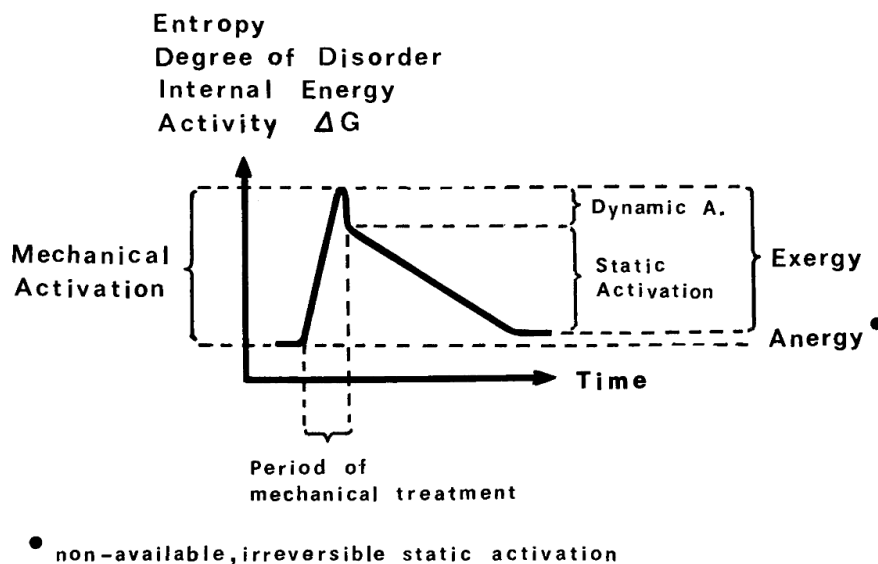
**Figure 1.18** An illustrative plot as to the time-dependence of mechanical energy derived from mechanical activation. Exergy is defined as the reversible usable amount of stored energy that can be transformed into other kinds of energy. Anergy is the irreversible inaccessible amount of stored energy. Reproduced from Ref. 84 with permission from Springer Nature.[84]

Take for example the mechanical activation of ores obtained from mining operations. Barry and co-workers investigated the properties of milled and unmilled aluminosilicate ores used to extract aluminum via acid leaching.[85] The ore itself contained mostly pyrophyllite [$Al_2Si_4O_{10}(OH)_2$], quartz [$SiO_2$], kaolinite [$Al_2Si_2O_5(OH)_4$], muscovite [$KAl_2(AlSi_3O_{10})(F, OH)_2$], and distene [$Al_2SiO_5$]. These minerals were identified by PXRD in the unmilled ore and their corresponding X-ray reflection intensities were monitored as a function of milling time (Figure 1.19). From the PXRD patterns, information about the degree of amorphization was obtained. The amorphization of quartz, evaluated at 28% after 30 min, was quite small in comparison to the amorphization of pyrophyllite and kaolinite, which were evaluated at 86% and 71% after 30 min, respectively. The thermal properties of the ore were also modified by the mechanical treatment, as indicated by thermogravimetric analysis (TGA) data (Figure 1.19). The region of greatest observed mass loss in the unmilled ore, between 400 to 1000 °C, occurred primarily due to dehydration and dehydroxylation of the minerals. The peak of the dehydroxylation process shifted to lower temperatures after milling, from roughly 650 °C to just over 500 °C. Further, the onset temperature of major dehydroxylation was noted to decrease with increasing milling time.
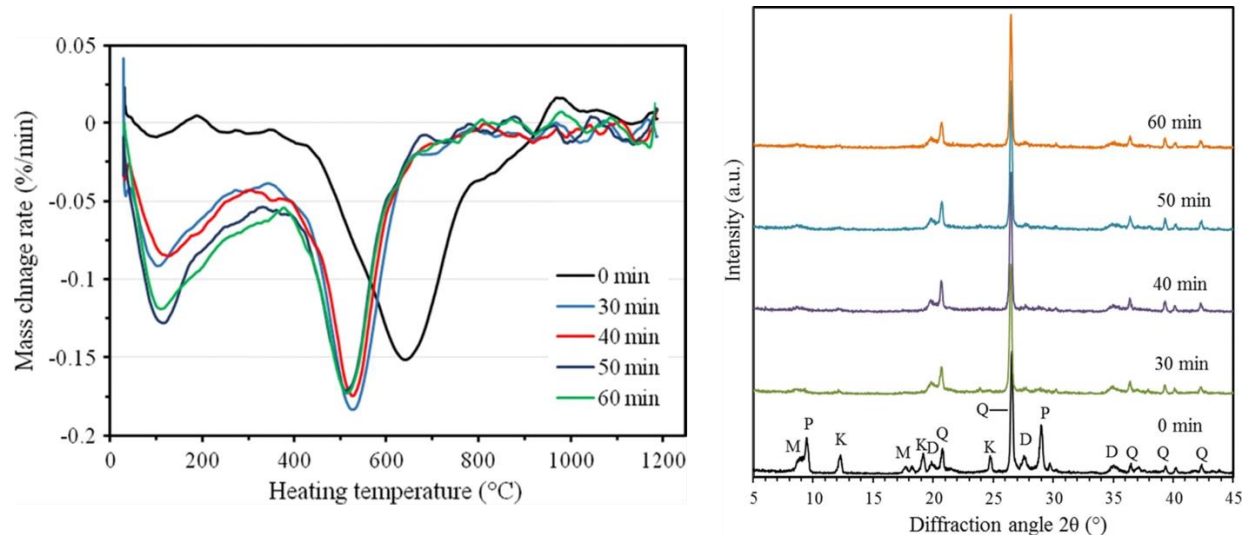
**Figure 1.19** (Left) Derivative thermogravimetric (DTG) curves of the unmilled and milled pyrophyllite ore obtained from TGA data. (Right) Comparison of XRD patterns of the unmilled and milled ore samples for various time. P pyrophyllite, Q quartz, K kaolinite, M muscovite, D distene. Reproduced from Ref. 85 with permission from Springer Nature.[85]

Visually, scanning transmission microscopy (SEM) micrographs revealed the change in microstructure of the mineral particles (Figure 1.20). Sharp edges and clean surfaces of lamellar-shaped layered minerals were destroyed and rounded upon milling. Fine particles observed after 30 minutes of milling were seen aggregating more and more upon additional milling time. The size and surface area changes seen by SEM were supported by BET specific surface area (SSA) measurements. Unmilled ore with an SSA of 0.27 $m^2$/g peaked at 55.73 $m^2$/g after 50 min of milling, and then decreased to 44.55 $m^2$/g after 60 min. These changes in material properties are reflected in the resulting extraction potential of aluminum from the unmilled and milled ore. When unmilled, acid leaching was successful at recovering only 12.57% of the aluminum: however, with an optimal milling time the recovery peaked at 73.09%.
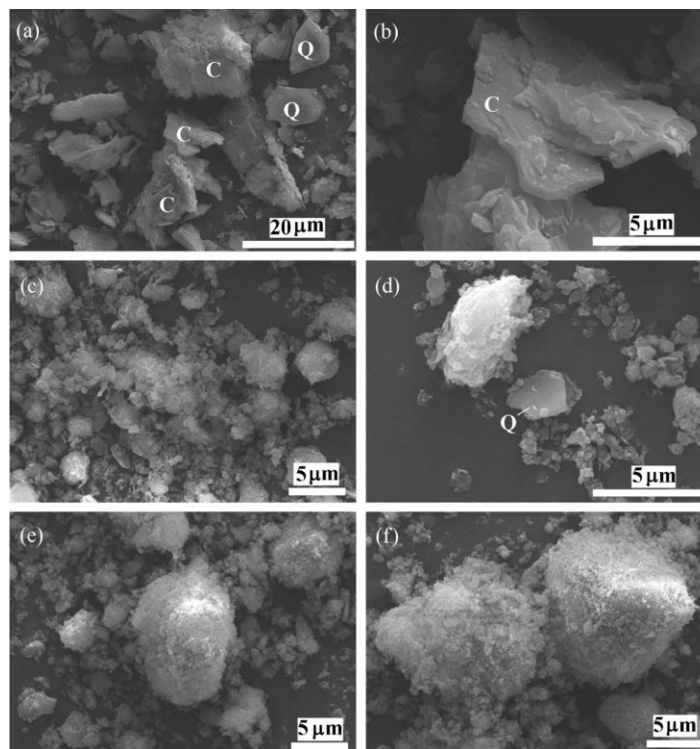
**Figure 1.20** SEM micrographs for the unmilled (a, b), and milled ore for 30 (c), 40 (d), 50 (e) and 60 (f) min. Q quartz and C clay mineral particle, pyrophyllite or kaolinite. Reproduced from Ref. 85 with permission from Springer Nature.[85]

Mechanical activation has been performed across a range of length scales. In 2015 Grzybowski and co-workers established that charged and radical species formed on the sticky surface of Scotch tape when mechanically pulled.[86] By immersing the mechanically activated tape into aqueous solutions of Au, Cu, Ag, or Pd salts, they successfully induced reduction and formation of metal nanoparticles (MNPs) on the sticky surface. A combination of AFM, Kelvin force microscopy (KFM), and magnetic force microscopy (MFM) were used to map the distribution of surface charges and radicals on the tape through analysis of the surface potentials and long-range magnetostatic coupling interactions, respectively (Figure 1.21). To confirm the presence of reduced MNPs post-immersion, further analysis was employed: UV–visible absorption measured the broad absorption of the localized surface plasmon resonance (LSPR) bands, SEM images confirmed the presence of nano-sized particles, X-ray photoelectron spectroscopy (XPS) was used to verify the valence state of the metals, and XRD was used to detect the formation of characteristic metallic crystal planes. It was also possible to pattern the

deposition of the MNPs onto the tape surface, creating novel functionalized surface micropatterns.
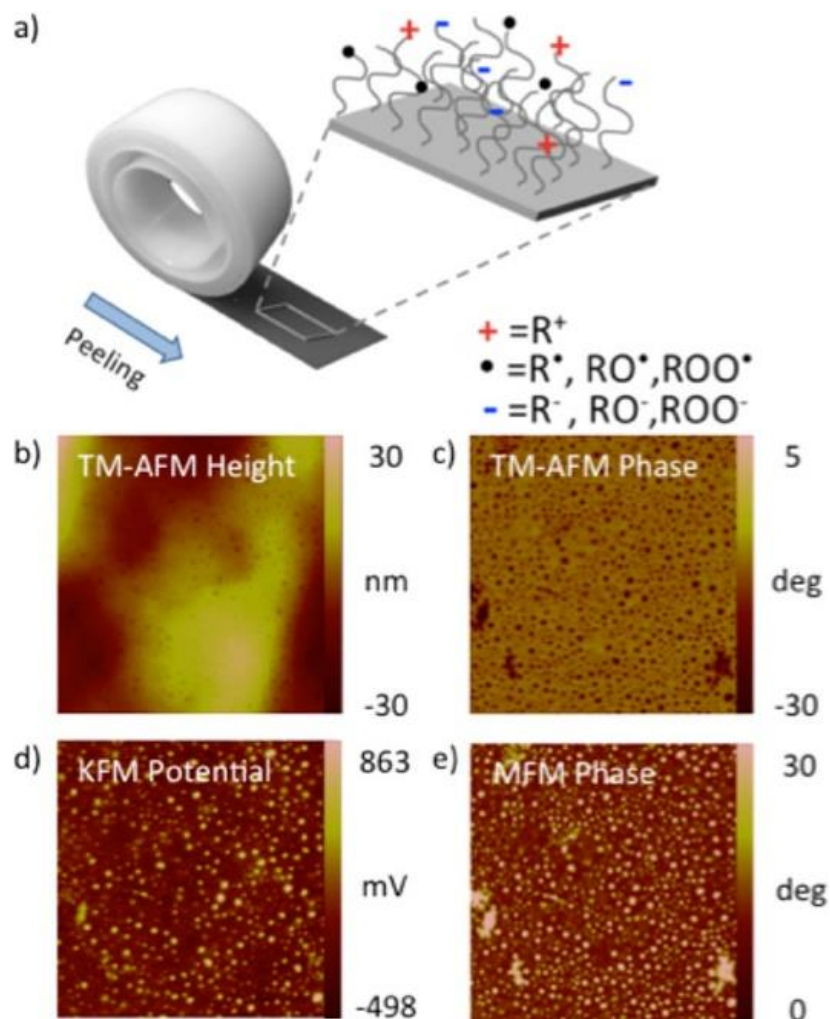


**Figure 1.21** (a) Formation of charged species as well as mechanoradicals on the sticky side of the adhesive tape upon peeling. (b) AFM height image, (c) AFM phase image, and (d) KFM map illustrating the charge mosaics comprising both positive and negative regions. (e) MFM map evidencing the presence of mechanoradicals (white spots). Reprinted with permission from Ref. 86. Copyright 2015 American Chemical Society.[86]

The mechanical activation of MNPs in the solid state has been computationally investigated as well. A 2021 publication by the Provatas group on the development of a thermodynamic model for a solid state ball-milling synthesis demonstrated that the activation energy is lowered when a ballistic term (i.e., mechanical energy) was added to a free-energy equation (Figure 1.22).[87] The team modelled the evolution of a homogeneous solid mixture of $Au^0$ atoms in a sea of octadecylamine (ODA) molecules,

both with and without mechanical activation. The initial disordered phase ($l_1$), where Au$^0$ atoms were isolated, proceeded toward an ordered phase ($l_2+\alpha$) where AuNPs formed if the energy in the system met or exceeded the activation energy ($\Delta G_A$). It was shown that with the inclusion of ballistic energy, in one instance the activation energy was reduced by 29.28%. Further, they noted that by increasing the value of the ballistic energy term the activation energy could be lowered even more. Because the simulated system is configured to be molecularly homogenous from the beginning, there is no need to consider mixing or comminution when adding the mechanical energy. However, in a real solid-state system the materials do not start as perfectly disordered and divided units. As stated in section 1.1, solid mixing does not produce a state like those achieved from melting or dissolution. In this next section, nanomaterials made through mechanochemical means will be discussed with an emphasis placed on our current understanding of the mechanisms and models that drive bottom-up nanostructure growth.
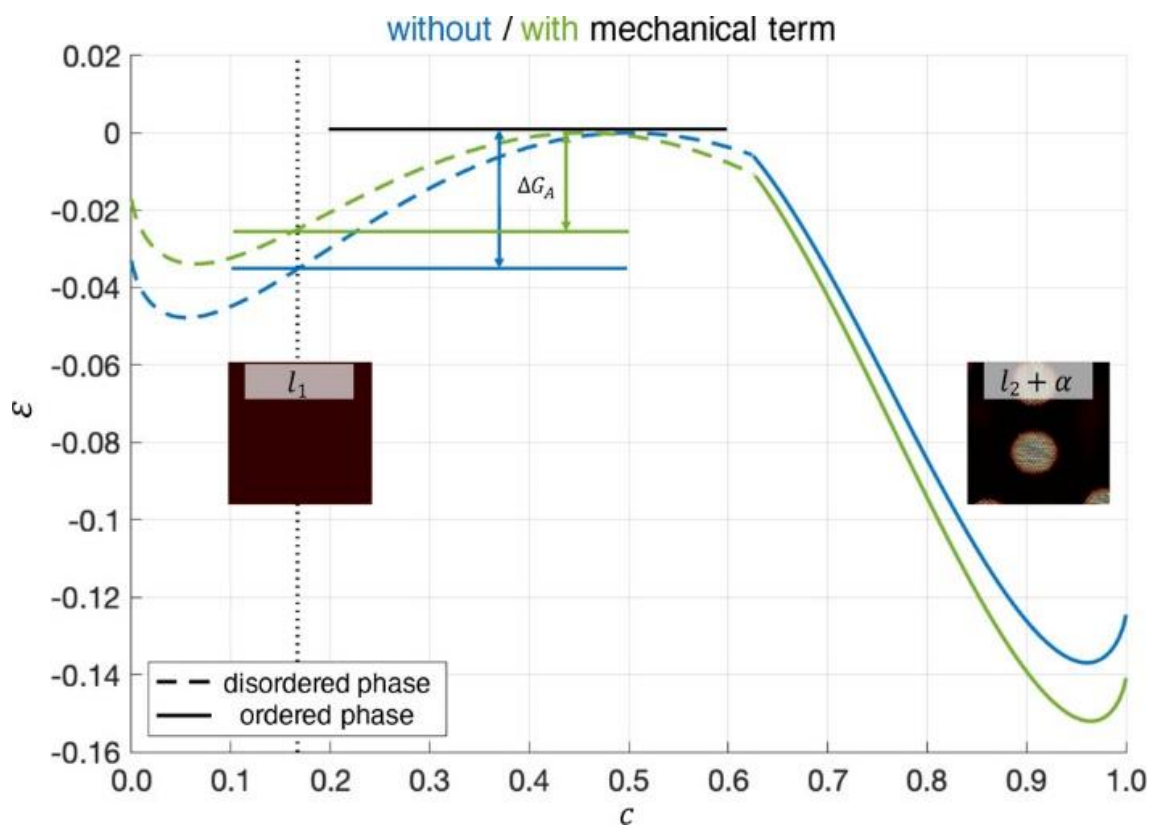


**Figure 1.22** Dimensionless free energy landscape of a Au$^0$–ODA system. The blue curves correspond to a free-energy profile with no mechanical energy, and the green curves correspond to a free-energy profile with a non-zero ballistic energy term. The x-axis variable $c$ is the fraction of the local volume occupied by gold atoms. Reprinted with permission from Ref. 87. Copyright 2021 American Chemical Society.[87]

## 1.3    Nanoparticles Through Bottom-Up Mechanochemistry

Nanomaterials, widely considered to be structures wherein at least one dimension is between 1 – 100 nm in size,[88, 89] have occupied a progressively larger space within the expanse of mechanosynthesis products. Functionally relevant nanomaterials, including those made mechanochemically, have been utilized in applications where they have acted as catalysts,[22, 90] as antibacterial materials,[91-93] as optical tools,[94, 95] as magnetic materials for theranostics,[96] imaging,[97] and data storage,[98] and as nano-sensors.[99-101] In classic nanoparticle synthesis there are two broad categories into which fit different synthesis approaches: top-down and bottom-up. In a top-down mechanochemical approach, nanoparticles are made by comminutive milling or mechanochemical alloying.[71, 102] In a bottom-up mechanochemical approach, nanoparticles are made via electron or ion exchanges.[103] Bottom-up mechanosyntheses allow for higher morphological control and lower size limits because the nanoparticles must go through a nucleation phase.[104] Differences between the two mechanical approaches, and a rough behavioral description of a material's surface area as a function of milling time, are illustrated in Figure 1.23.
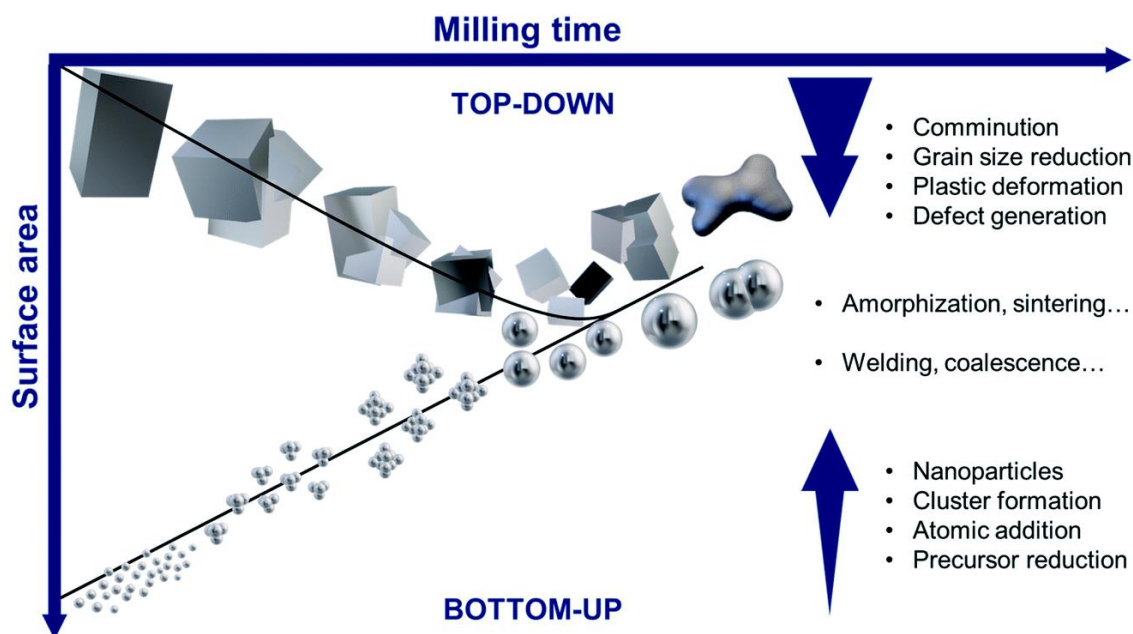


**Figure 1.23** Mechanochemical synthesis of nanoparticles: top-down and bottom-up approaches. Reproduced from Ref. 104 with permission from the Royal Society of Chemistry.[104]

Bottom-up syntheses involve an ion exchange stage, a nucleation stage, and a growth stage. For MNP and binary nanoparticle (BNP) mechanosyntheses, the electron and ion exchange processes have been reviewed by Moores and co-workers, who also produced generalized reaction schemes for three different bottom-up pathways (Figure 1.24).[103] In the top-most scheme of Figure 1.24, MNPs made from electron exchanges require a metal precursor, a reducing agent, and a ligand to passivate the particle surface and prevent agglomeration. Metal precursors are transformed through a reductive nucleation process which is proceeded by MNP self-assembly. BNPs made from electron-exchange nucleation utilize neutral valency precursors, one reagent for each of the two constituent species. Mechanochemical mixing of the two reagents in the presence of a ligand leads to the energetically favourable electron exchange reaction between the two reagents and their subsequent self-assembly. BNPs made via an ion exchange utilize charged valency reagent compounds, where the energetically favourable exchange of ions between the compounds drives the reaction. Note here that although this is not a redox reaction, reduction in precursor size at the expense of product formation and growth is still achieved.

Electron exchange for metal NP synthesis
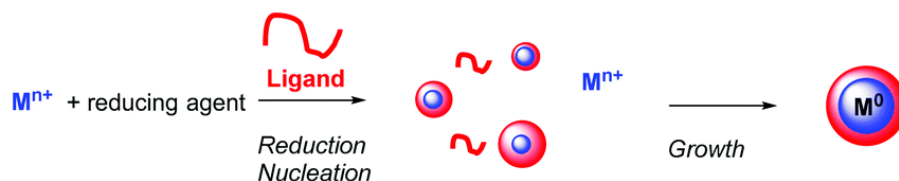
$M^{n+}$ + reducing agent $\xrightarrow[\substack{\textit{Reduction} \\ \textit{Nucleation}}]{\textbf{Ligand}}$ ... $M^{n+}$ $\xrightarrow{\textit{Growth}}$ $M^0$

Electron exchange for binary compound NP synthesis

$M + Z$ $\xrightarrow[\substack{\textit{E-exchange} \\ \textit{Nucleation}}]{\textbf{Ligand}}$ $Z^{x-}$ ... $M^{n+}$ $\xrightarrow{\textit{Growth}}$ $M_xZ_n$

Ion exchange for binary compound NP synthesis

$M^{n+} + Z^{x-}$ $\xrightarrow[\substack{\textit{Ion metathesis} \\ \textit{Nucleation}}]{\textbf{Ligand}}$ $Z^{x-}$ ... $M^{n+}$ $\xrightarrow{\textit{Growth}}$ $M_xZ_n$
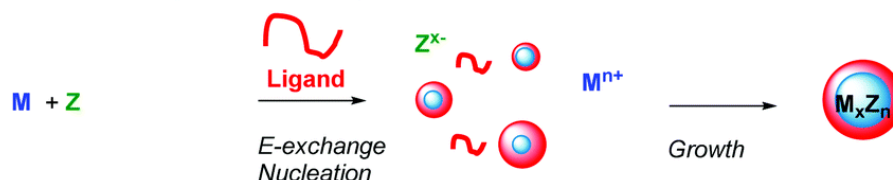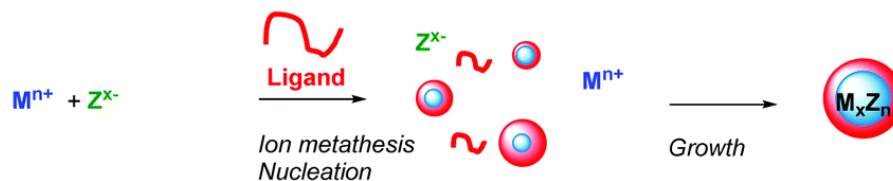
**Figure 1.24** Bottom-up nanomaterial synthesis by mechanochemistry for metal (via electron exchange) and binary material (via electron or ion exchanges). Reproduced from Ref. 103 with permission from the Royal Society of Chemistry.[103]

In a review on the bottom-up mechanosynthesis of noble metal nanoparticles (NMNPs), Camargo and co-workers segregated the types of products into two categories: unsupported NMNPs and supported NMNPs.[104] To prevent aggregation, nanoparticles must either by capped or thoroughly dispersed. Ligands work by passivating the nanoparticle surface, limiting contact between two adjacent nanoparticles.[105] Supports work by dispersing the nanoparticles over and/or within a solid matrix, effectively preventing aggregation through distancing. Both are effective stabilizers, however choosing whether to passivate nanoparticles with a ligand or to mount them onto a support, and selecting which ligand or support to use, will affect the chemical and physical properties of the system. To help convey the kinds of MNP products that are possible with bottom-up mechanochemistry, select examples are presented below with a strong focus on AuNPs.

Carbon nanotubes (CNTs) are well known for their electrical conductivity and mechanical strength.[106] Connell and co-workers used multi-walled CNTs (MWCNTs) as supports in the mechanochemical preparation of ultrasmall silver nanoparticles

(AgNPs).[107] Ag(I) acetate was ball-milled with MWCNTs at a 1 mol% Ag:C ratio; the resulting powder was characterized with SEM, high-resolution TEM (HRTEM), and PXRD (Figure 1.25). Particles found on the AgNP@MWCNT product had an estimated average size of ~2.5 nm were recorded. This reaction procedure was extended to other metal-salts, such as Au(III) acetate, Pd(II) acetate, and Pt(II) acetylacetonate, and to other carbon-based supports including single-walled CNTs (SWCNTs), expanded graphite (EG), and hexagonal boron nitride (h-BN).
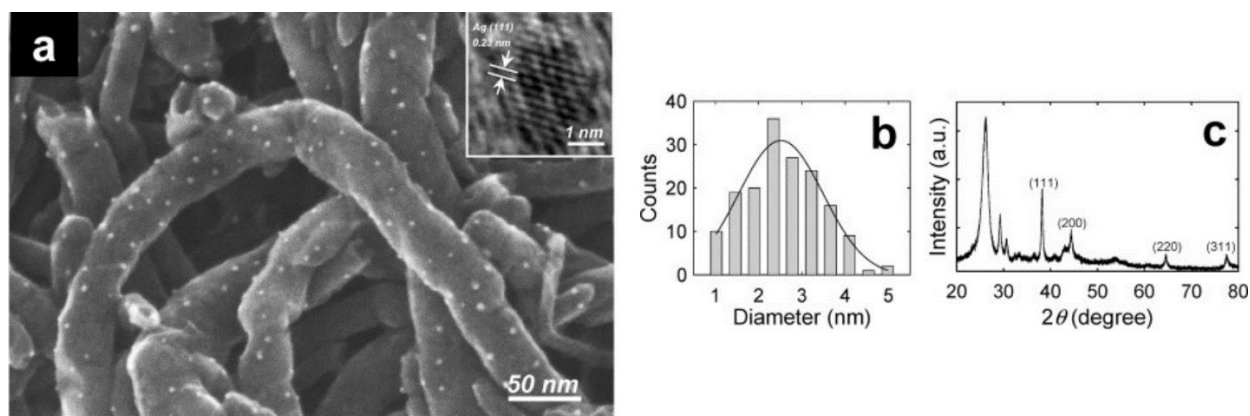


**Figure 1.25** Ag nanoparticle-decorated MWCNTs from 10 min of ball-milling of MWCNTs (diameter ~10−30 nm) and silver acetate ([Ag]$_{feed}$ ~1 mol %): (a) a SEM image and (inset) a HR-TEM image; (b) Ag nanoparticle size-distribution plot; and (c) XRD pattern. The crystal planes of Ag metal are noted on the corresponding X-ray reflections. Reprinted with permission from Ref. 107. Copyright 2009 American Chemical Society.[107]

Ceramic metal oxides such as $TiO_2$ and $Al_2O_3$ have been readily used as supports for MNPs.[108, 109] Metal-organic frameworks (MOFs) are a distinct class of coordination polymers known for their high porosity and surface area, qualities that are desirable for a solid support matrix.[110, 111] Chen and co-workers employed planetary ball-milling to synthesize palladium nanoparticles (PdNPs) supported on a zeolitic imidazolate framework (ZIF), a sub-class of MOF, and used the product (Pd@ZIF-8) as a catalyst for the hydrogenation of olefins.[112] A sacrificial synthesis mechanism was used whereby $PdCl_2$ was dispersed onto ZnO through milling, reduced under $H_2$, and then remilled with 2-methylimidazole (Hmim) to begin the sacrificial growth of ZIF-8 around the PdNPs (~4.5 nm) at the expense of ZnO (Figure 1.26). This way, the PdNPs that formed on the surface of the original metal-oxide support are then encapsulated within the newly grown MOF. Pd@ZIF-8 presented a high catalytic selectivity for the hydrogenation of 1-hexene and

styrene (> 95%) but negligeable activity for cyclooctene and tetraphenyl ethylene (< 5%). The sieving effect of ZIF-8 promoted high size and shape selectivity towards reactants introduced into the system.
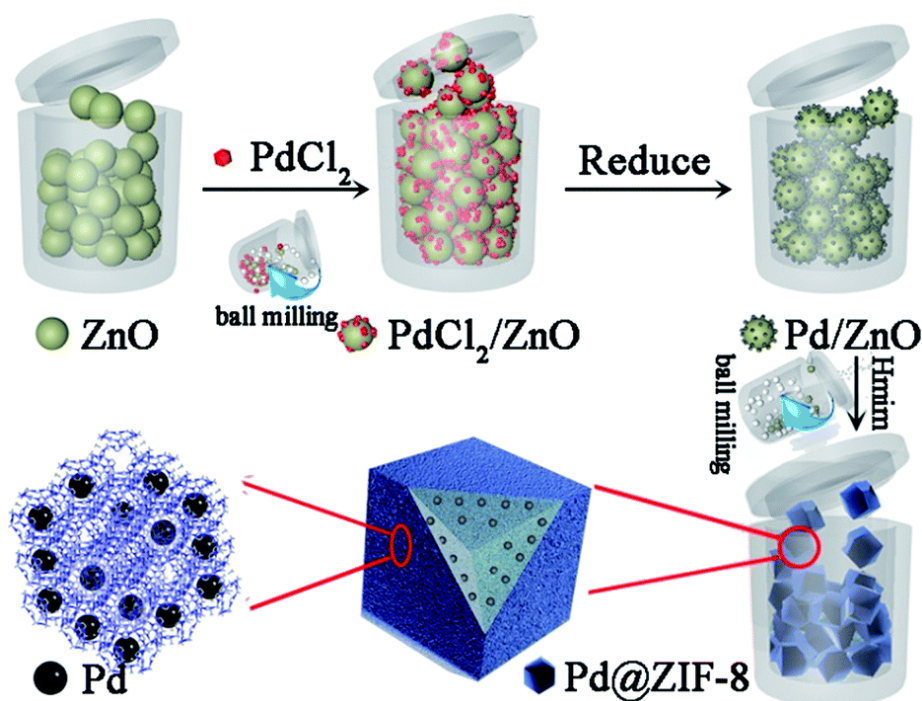


**Figure 1.26** Synthesis procedure of Pd@ZIF-8 via the mechanochemistry-assisted approach. Reproduced from Ref. 112 with permission from the Royal Society of Chemistry.[112]

Several different bio-based supports such as lignin,[113] eggshell-derived $CaCO_3$,[114] and cellulose nanocrystals have been used to mount MNPs.[115] The benefits of using bio-based materials are their low cost, high abundance, and bio-compatibility. Baláž and co-workers used three different plant species, *Thymus serpyllum L.* (SER), *Sambucus nigra L.* (SAM) and *Thymus vulgaris L.* (TYM) as both a reducing agent for $AgNO_3$ and a support for the resulting AgNPs (Figure 1.27).[91] Various Ag:plant mass ratios (1:1, 1:10, 1:50 and 1:100) were investigated and the antibacterial activity of the products were tested. They found that the higher the mass ratio the more rapid the reduction which led to smaller AgNPs; however, only the lowest ratio had a high enough AgNP concentration to be applied effectively as an antibacterial product.
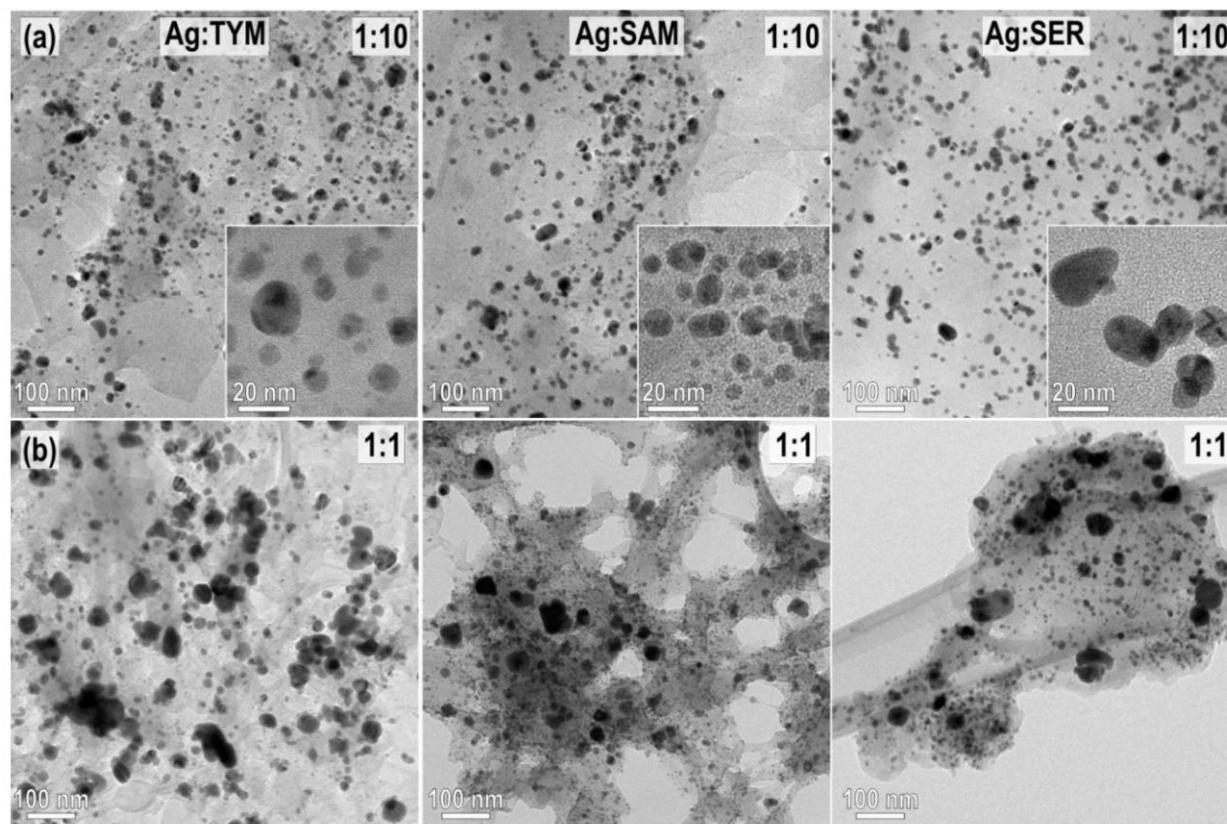
**Figure 1.27** TEM images of the Ag:plant W samples (a) 1:10 and (b) 1:1. Insets in the (a) are magnifications showing the presence of AgNPs with sizes below 10 nm. Reproduced from Ref. 91 with permission from MDPI.[91]

The first solid-state route to produce AuNPs was published in 2009 by Geckeler and co-workers.[116] The team used a bottom-up mechanosynthesis method wherein they milled the gold-salt potassium tetrachloroaurate (III) with the ligand poly(vinylpyrrolidone) (PVP), and the reducer sodium borohydride (NaBH$_4$) in a vibrational mill at 1500 rpm at ambient temperature. Investigating different conditions such as reagents mass ratios, ligand molecular weight, and milling time, statistically relevant values for the tunable average particle diameter were recorded (Table 1.2). Along with TEM analysis that enabled quantization of particle diameters and particle size dispersity, a combination of FTIR, UV-visible spectroscopy, and PXRD techniques helped confirm the growth of AuNPs in the solid powder. It was found that the average particle diameter trended towards larger sizes if shorter ligand chains or high gold-salt concentrations were employed. Likewise, longer ligand chains and lower gold concentrations produced smaller

particle on average. Milling time was found to correlate positively with particle size and particle size dispersity in all cases.

**Table 1.2** The experimental conditions for the synthesis of the gold nanoparticle samples and their corresponding sizes.[116]

| Sample | Mass ratio of KAuCl$_4$ : PVP : NaBH$_4$ | PVP[a] (kg mol$^{-1}$) | Time (min) | Particle diameter (nm) |
|---|---|---|---|---|
| A | 10 : 25 : 1 | 10 | 15 | 8.8 ± 2.8 |
| B | 10 : 25 : 1 | 10 | 30 | 10.7 ± 1.1 |
| C | 10 : 25 : 1 | 10 | 60 | 13.4 ± 2.4 |
| D | 10 : 25 : 1 | 10 | 120 | 23.3 ± 5.0 |
| E | 10 : 25 : 1 | ~30 | 15 | 6.3 ± 2.1 |
| F | 10 : 25 : 1 | ~30 | 30 | 7.5 ± 2.4 |
| G | 10 : 25 : 1 | ~30 | 60 | 8.4 ± 2.7 |
| H | 10 : 25 : 1 | ~30 | 120 | 8.8 ± 3.4 |
| I | 5 : 25 : 1 | 10 | 15 | 7.6 ± 2.3 |
| J | 5 : 25 : 1 | 10 | 30 | 8.3 ± 2.9 |
| K | 5 : 25 : 1 | 10 | 60 | 8.6 ± 2.3 |
| L | 5 : 25 : 1 | 10 | 120 | 11.8 ± 4.4 |
| M | 15 : 25 : 1 | 10 | 15 | 27.9 ± 6.2 |
| N | 15 : 25 : 1 | 10 | 30 | N.A.[b] |
| a) Mass average molar mass. b) Aggregation of particles was observed. | | | | |

Moores and co-workers reported a galvanic reduction pathway to produce ultrasmall spherical AuNPs from a Au(III) salt milled in a 1:5 ratio with various long chain amine ligands (Figure 1.28).[117] The steel assembly of the milling jar and balls provided the necessary transfer of electrons that enabled the transformation of AuCl$_4^-$ to Au$^0$. By varying certain parameters such as ligand length and species, milling time, and the ligand to gold ratio, the group was able to create a size-tunable mechanosynthesis. Relationships such as those between particle size and ligand length or milling time were found to mirror trends first observed by Geckeler and co-workers. Using ligands of shorter lengths such as C15 (4.2 ± 1.2 nm) and C16 (1.8 ± 0.3 nm) resulted in larger average particle sizes, while longer ligands like C17 (1.5 ± 0.2 nm) and C18 (1.3 ± 0.2 nm) amines produced smaller particles on average. Experimenting with ODA, a higher ligand to gold

ratio of 5:1 resulted in smaller particles of 1.3 ± 0.2 nm, while lower ratios of 3:1 and 2:1 produced larger particles of 1.6 ± 0.2 nm and 1.9 ± 0.3 nm, respectively. Investigation of milling time found that longer times are associated with larger final particle sizes. A reaction with ODA in a 5:1 ligand to gold ratio milled at 29.5 Hz was run for 15, 30, 60, 90, and 180 minutes and resulted in particles with a mean diameter of 1.2 ± 0.2 nm, 1.3 ± 0.2 nm, 1.4 ± 0.2 nm, 1.6 ± 0.2 nm, and 3.9 ± 1.0 nm, respectively. Ligands other than long chain amines were tested with relatively poor results. 4-dimethylaminopyridine (DMAP) and 4,4′-bipyridine (4,4′ BIPY) resulted in incomplete reduction, imidazole and 1-methylimidazole produced large irregular particles, benzyl disulfide caused irregular aggregation, ω-mercaptododecanoic acid formed films on the TEM grids and citrate generated large particles ~500 nm across. The reaction was successfully scaled up from 200 mg to 1 g of solid material, and characterization with mass spectrometry (MS) was reported to be the first for amine-stabilized AuNPs.
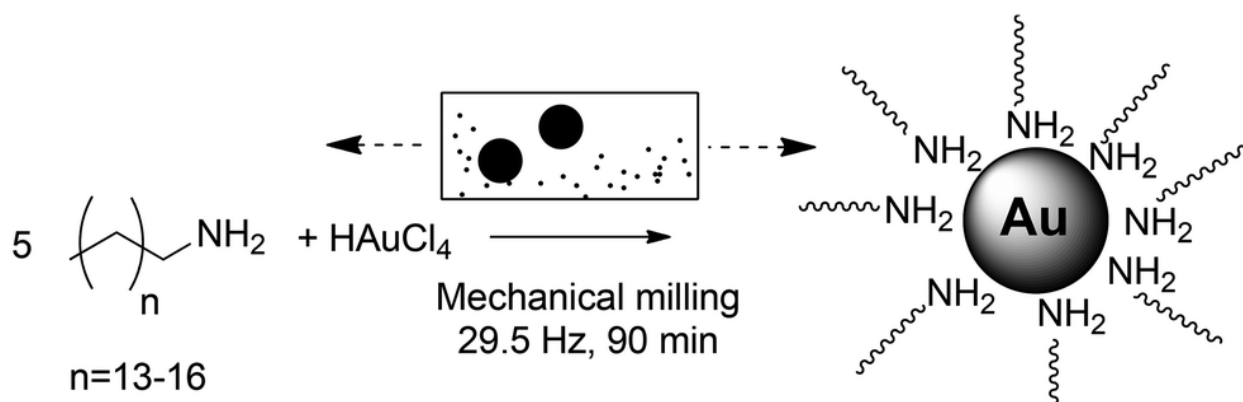


**Figure 1.28** Mechanosynthesis of amine gold nanoparticles based on the galvanic reduction of HAuCl$_4$. Reproduced from Ref. 117 with permission from the Royal Society of Chemistry.[117]

Camargo and co-workers published a combined mechano-colloidal method to synthesize a unique nanotadpole morphology of MNPs.[118] Using AuNPs as a foundation and later expanding into AgNPs, the team directly imaged different growth stages of the nanotadpoles using TEM (Figure 1.29). To produce this morphology, AuCl, PVP, and sodium citrate were first milled together at room temperature in a vibrational ball mill to generate small AuNPs in the solid state. The milled powder, containing some reduced Au$^0$ product and some unreduced Au$^+$ precursor, was then dispersed into water where the solution environment prompted a seeded-style growth of the unreduced material. The

nanocrystals of Au grown in solution began to self-assemble through oriented attachment into 1D chains that were anchored onto the surface of the larger AuNPs synthesized from milling. The head size and tail length of the nanotadpoles could be controlled through milling time, whereby a longer mill resulted in less unreduced material to be dispersed in solution therefore leading to larger head sizes and shorter chain lengths. To gauge the extent of reaction as a function of milling time, chemical transformation was tracked through PXRD, X-ray absorption near edge structure (XANES) spectroscopy, and diffuse reflectance spectroscopy (DRS). It was suggested that the MNP tadpoles may find use in areas such as catalysis, self-assembly, surface-enhanced Raman scattering, sensing, and the development of nanomotors.
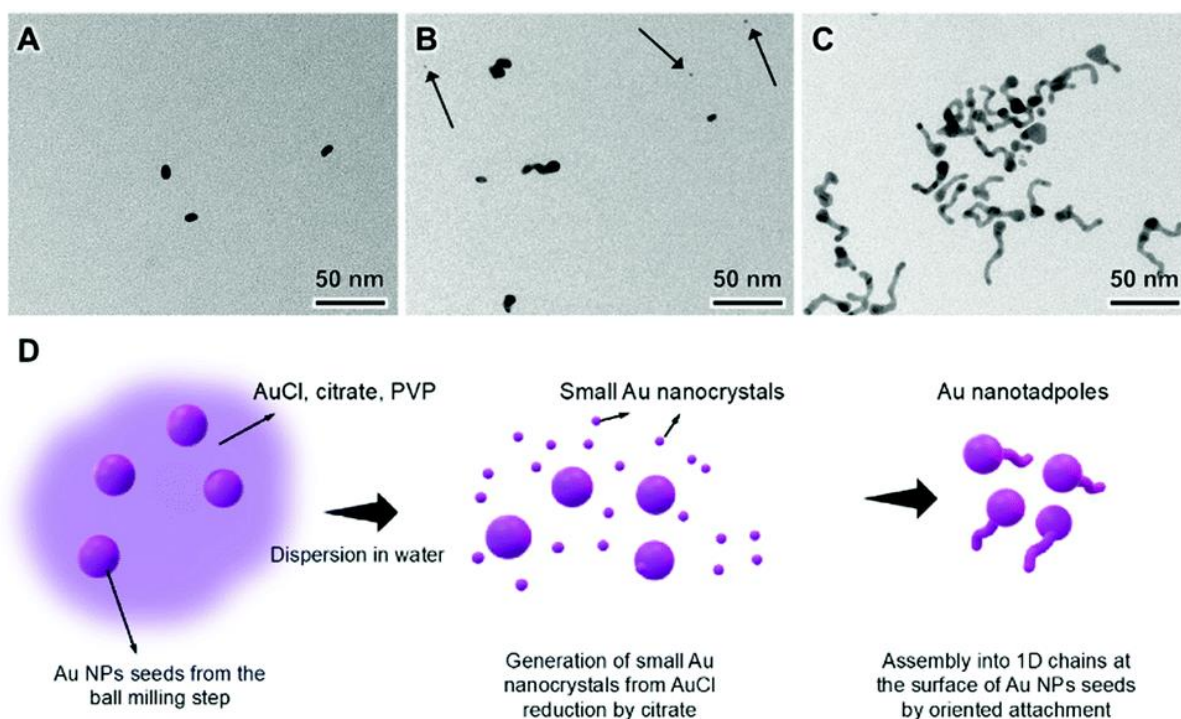


**Figure 1.29** (A–C) TEM images depicting the morphological evolution of the samples during the solution-phase step following ball-milling. Here, aliquots were isolated from the reaction suspension after (A) 5, (B) 15 and (C) 30 min during the solution-phase step following ball-milling (30 min of milling, ball-to-powder ratio 95:1; Au:citrate and Au:PVP molar ratios corresponding to 1:1 and 1:8, respectively). (D) Proposed mechanism for the formation of the nanotadpoles during the solution phase step involving seeded growth. Here, the reduction of AuCl by citrate leads to the formation of small Au nanocrystals (as denoted by the black arrows in B and D), that can assembly into 1D chains from the surface of the Au NPs seeds leading to the formation of the nanotadpoles. Reproduced from Ref. 118 with permission from the Royal Society of Chemistry.[118]

Mechanochemically synthesized AuNPs were explored further by Emmerling and co-workers, who used a tandem X-ray absorption spectroscopy (XAS) and PXRD analysis setup to probe the *in situ* environment of solid-state transformations of $AuCl_4^-$ to $Au^0$ in the presence of PVP and a reductant.[119] Alternating between the chemical reductants hydroquinone (HQ), ascorbic acid (AA), and $NaBH_4$, the group collected time-resolved *in situ* PXRD (TRIS-PXRD) and time-resolved *in situ* XANES (TRIS-XANES) profiles (Figure 1.30). The benefit of this tandem analysis was the ability to simultaneously acquire complimentary information on the changing valent state of the Au species and the formation of the crystalline $Au^0$ species, all while milling. Reduction-onset of $AuCl_4^-$ as measured by TRIS-XANES was observed within 15 minutes of milling when using the HQ and AA, and within 23 minutes when using $NaBH_4$. Reduction with HQ was described as initially rapid however quickly slowing, and eventually stagnating without completing the reduction of all $Au^{3+}$ species even after 360 minutes of milling. Under HQ and AA reduction, TRIS-PXRD revealed $Au^0$ formation after 15 minutes, matching the kinetics obtained from TRIS-XANES. Growth of the reduced $Au^0$ species was similarly described as being initially rapid and progressively slower. Reactions run with $NaBH_4$ behaved in much the same way, however with relatively slower observed rates of transformation. Studying the dynamic electronic and crystalline behaviors of the milled powder, the team demonstrated a powerful analysis technique to study the kinetics of bottom-up

mechanochemical　　　nanoparticle　　　reduction　　　and　　　formation.
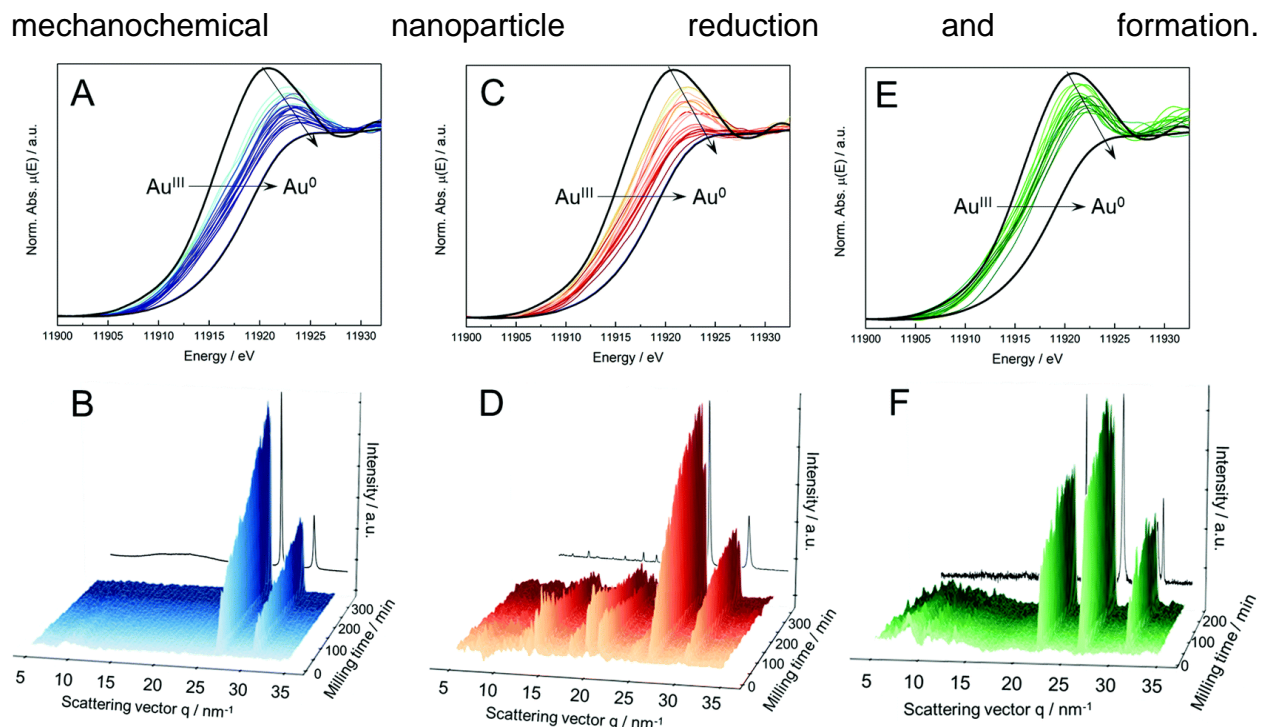


**Figure 1.30** TRIS-XANES (Au-L$_{III}$ edge) (top) and TRIS-PXRD patterns (bottom) for the synthesis of AuNPs under ball-milling conditions using HQ (A and B), AA (C and D) and NaBH$_4$ (E and F) as reducing agents. The black spectra in A, C and E correspond to the Au$^{3+}$ (HAuCl$_4$·3H$_2$O) and Au$^0$ (foil) standards. The PXRD patterns shown as the black traces in B, D, and F are data from ex situ measurements after the milling period. Reproduced from Ref. 119 with permission from the Royal Society of Chemistry.[119]

Emmerling and co-workers' tandem TRIS-XANES and TRIS-PXRD study was a strong step forward in studying bottom-up nanoparticle synthesis in the solid state; however, certain observables such as direct monitoring of particle size growth was not possible. Only long after nucleation and much growth were the particles, most very large and above 100 nm, directly imaged. To further explore bottom-up solid-state reactions, and to develop models for nanoparticle mechanosynthesis, more must be learned about the mechanisms that guide particle formation. For example, through theory and experiment a great deal has been learned about nanoparticle synthesis in solution.[120, 121] In classical nucleation theory (CNT) there is the often-cited work of LaMer and Dinegar that describe so-called short-lived instantaneous burst nucleation events.[122] This was a qualitative model proposed to explain the observation of tightly sized controlled populations of particles produced in solution. A detailed discussion of its origins, assumptions, and complications was published in 2019 by Finke and co-workers.[123]

LaMer's description of diffusion-controlled growth was taken a step further by Wilhelm Ostwald, who employed a thermodynamic argument for a surface area to volume minimization process coined 'Ostwald ripening'.[124] He proposed that smaller particles would tend to redissolve back into solution and deposit onto larger particles, since smaller particles have higher surface energies relative to the amount of volume they occupy. An antithetical theory of digestive ripening was proposed whereby the larger particles redissolve at the expense of growth of smaller particles.[125] A recent publication by Zheng and co-workers used *in situ* atomic resolution imaging with liquid cell TEM to directly observe the ripening of core-shell Cd-$CdCl_2$ nanoparticles.[126] They found that particles grew when crack defects were formed in the shell. Generation of these defects was followed by healing mediated through an ion diffusion at the expense of other nearby particles. The team described the observed growth as driven by the repeated formation and annihilation of crack defects (Figure 1.31).
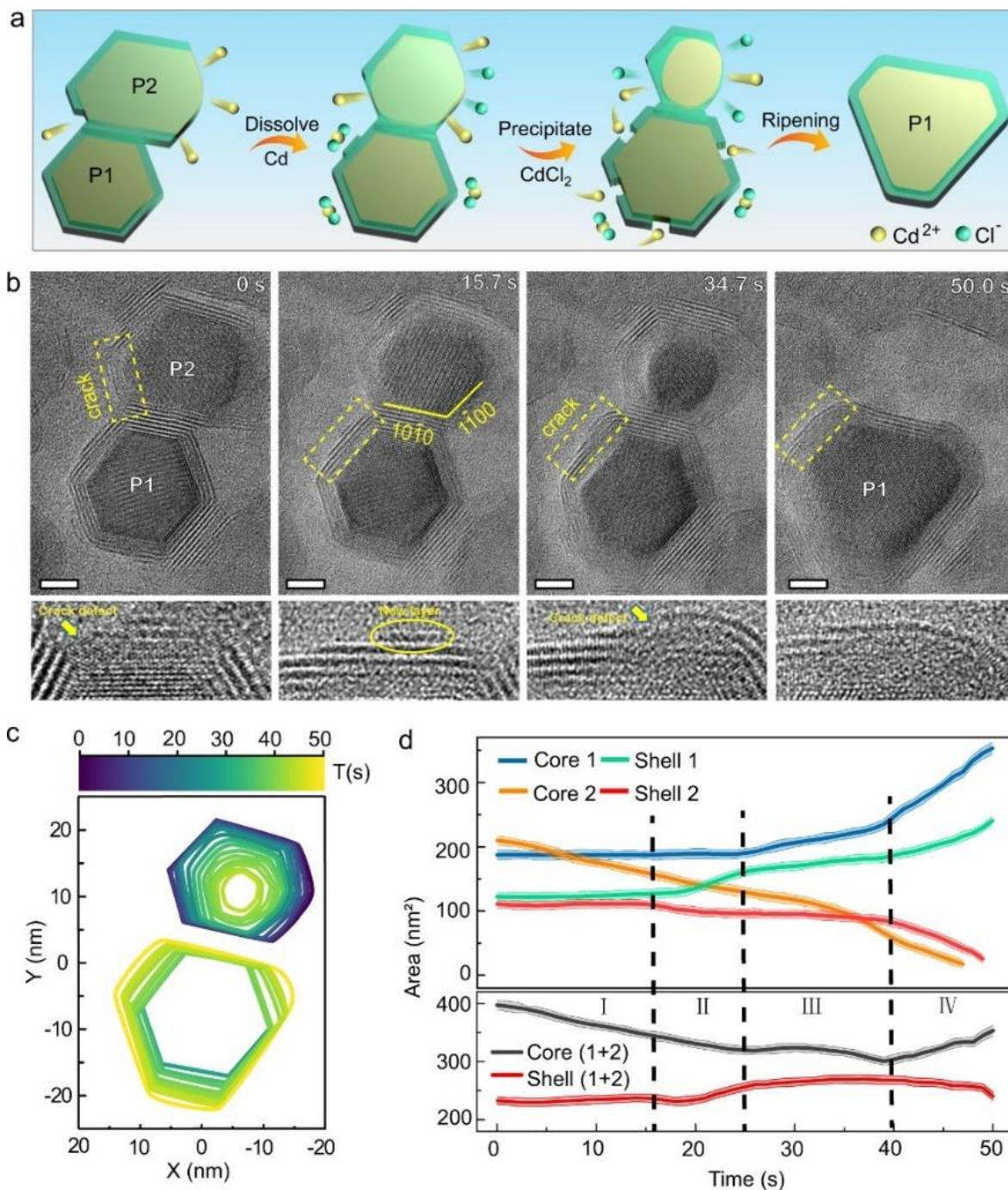
**Figure 1.31 (**a) Schematic illustration of the evolution pathway of Cd-CdCl₂ core-shell nanostructures during the defects-mediated ripening. (b) Sequential images show the ripening process after two Cd-CdCl₂ core-shell particles are connected. P1 and P2 mark out the two particles. Scale bar, 5 nm. The enlarged images of the yellow square areas listed below highlight an incomplete shell, a new CdCl₂ layer, a new crack defect and healing of the shell. (c) The colored contours indicate the shape evolution of the two cores. (d) The measured projected areas of the core and shell for P1 and P2 as a function of time. I, II, III, and IV refer to the four intervals of the dynamic process. The transparent lines around the solid lines indicate the standard deviation error of the measurement. Reproduced from Ref. 126 with permission from Springer Nature.[126]

The Finke-Watzky two-step mechanism is a proposed theory of nucleation and growth where both regimes occur simultaneously.[127] The first step describes a slow continuous nucleation, followed by an autocatalytic surface growth which is not diffusion controlled. There exists also DLVO theory (named for Boris Derjaguin, Lev Landau, Evert Verwey, and Theodoor Overbeek), developed in 1948 to quantitatively describe the colloidal stability of species with surface charges.[128] This theory assumes that the total force between two colloidal species is the sum of their van der Waals and electric double layer interactions, interactions which depend on the species' size, surface potential, concentration, and ion type. Coalescence and oriented attachment both describe particle growth mechanisms where different particles come together and join, creating either many randomly oriented fused crystallites or a single larger ordered domain, respectively.[129, 130] Gold nanoparticles have been shown to adopt different nucleation and growth pathways depending on the conditions in which they are grown.[131] From experimental studies with *in situ* small-angle X-ray spectroscopy (SAXS) and XANES techniques, Kraehnert and co-workers proposed a four-step nucleation and growth process based on a Turkevich synthesis of gold nanoparticles (Figure 1.32).[132]
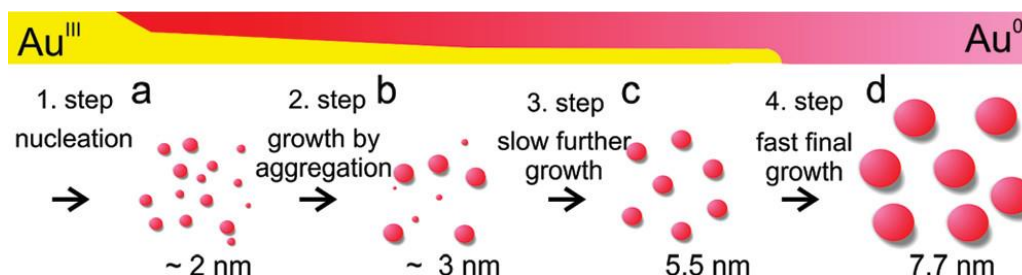


**Figure 1.32** Schematic illustration for the deduced process of gold nanoparticle formation. Reprinted with permission from Ref. 132. Copyright 2010 American Chemical Society.[132]

Unfortunately, there currently exists no widely accepted or relayed models for nanoparticle growth in solid-state mechanochemical systems. Further study of the kinetics and mechanistics of reduction and formation hopes to uncover mechanisms and develop models for nanoparticles in the solid state, just as was done for the solution state. In this next section, the topic of chemical aging will be discussed as it pertains to the mechanosynthesis of nanoparticles. By the end the reader should understand what chemical aging is and why it may be useful in studying the evolution of bottom-up nanoparticle mechanosynthesis.

## 1.4   Chemical Aging & Solid-State Mechanosynthesis

Chemical aging is the static treatment of a chemical system over a prescribed length of time. Aging processes may be implemented to simplify reaction design and scale-up, minimize energy and solvent use, and exploit nanoparticle self-assembly through static transformations.[133, 134] Aging mechanochemical reactions, distinct from LAG and neat grinding methods, often feature a brief pre-aging mechanical activation step and strict aging environments where temperature, atmosphere, solid wetness, vapour concentrations, and light exposure are tightly controlled. Accelerated aging is a sub-set of aging reactions with the aim of increasing system reactivity while minimizing energy and solvent usage. Friščić and co-workers broadly defined accelerated aging reactions as diffusion-controlled, directed only by mild or short-lasting environmental changes, and occurring between initially solid reagents.[135, 136] By restricting the amount of energy put into a system, aging may also be used to observe reaction progression at a slower pace. These two kinds of aging are reminiscent of weathering processes, which serve as the original inspiration for such reaction designs. Friščić and Huskić noted the surprising complexity of organic minerals produced through chemical and physical weathering, and the remarkable similarity these materials had with advanced artificial organic and metal–organic materials.[137]

Among other things, aging has been used to synthesize CuI-pyrazine hybrid materials,[138] hemicucurbiturils,[139] paceite and its cadmium analogue,[140] co-crystals,[141] and terephthalic acid through a solid-state ambient hydrolysis of waste polyethylene terephthalate.[142] Numerous MOFs have been synthesized using aging methods; the combination of highly porous structures and high vapour concentrations being markedly exploitable.[143-145] In 2012, Friščić and co-workers presented a proof-of-principle study demonstrating the potential of accelerated aging for synthesizing metal-organic materials, using the transformation of ZnO into various ZIFs as a model.[146] Using catalytic amounts of ammonium sulfate salt, ZnO was manually ground with different imidazole-based ligands, imidazole (Him), 2-methylimidazole (HMeim)**,** 2-ethylimidazole (HEtim), and benzimidazole (HBim), and aged at mild temperatures under high humidity (Figure 1.33). Different ZIF products were synthesized depending on the aging time, temperature,

vapour solvent, humidity, and inclusion of the salt catalyst. Using methanol or ethanol vapours, certain closed-packed ZIF products of accelerated aging were converted to the commercially relevant open structure ZIF-8. Selected reactions were scaled up from 0.5 g to 10 g with accelerated aging. Reported advantages of these solid-state accelerated aging syntheses include not requiring soluble transition metal salts, use of common and stable reagents, scalable reactions, and low thermal and electrical energy usage.
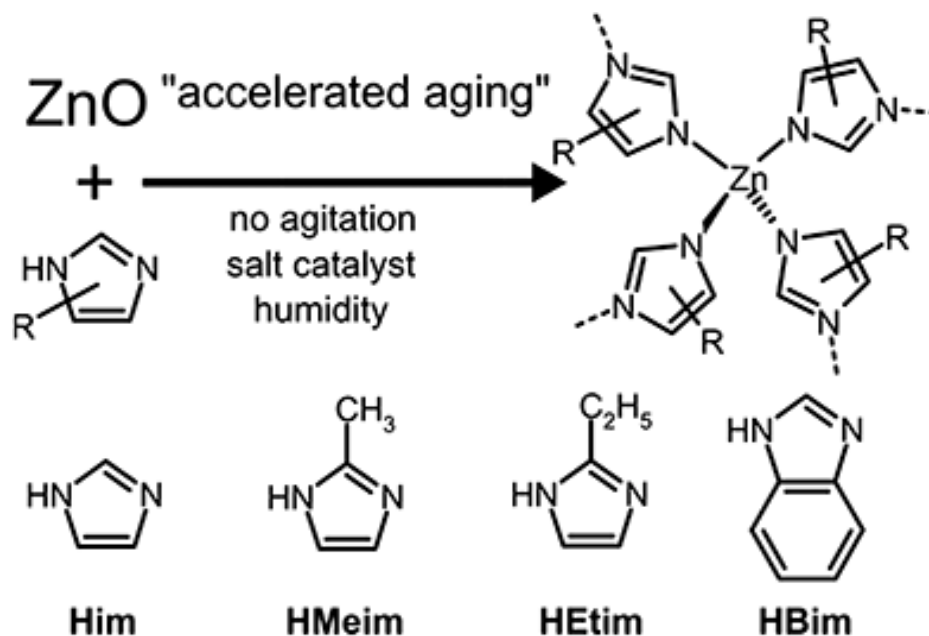


**Figure 1.33** The proposed reactivity by accelerated aging (top) and the selected model ligands (bottom). Reproduced from Ref. 146 with permission from the Royal Society of Chemistry.[146]

Aging has also been used in the transformation of biopolymers into functional materials. In 2019 Moores and co-workers published a mechanochemical aging method to transform chitin, the world's second most abundant biopolymer, into chitosan while maintaining a high molecular weight (MW).[147] The team took commercial chitin with a 4% degree of deacetylation (DDA), ball-milled the material for 30 minutes, milled another 5 minutes with NaOH in a 1:5 chitin:NaOH ratio, and then transferred the milled powder to different aging chambers (Figure 1.34). For commercial applications, chitin with a DDA above 70% is desired; in high humidity (98% RH), DDA values over 70% were achieved after aging for 6 days at room temperature or after 24 h at 50 °C. Exploring different aging temperature, humidity, and time conditions lead to DDA values up to 98% while retaining high MW. The optimized deacetylation by aging was successfully scaled-up from 200 mg

to 10 g using a planetary mill, and energy consumption values over 9 times lower per gram of chitin were recorded when compared to a solvothermal process. More recently, the same group developed a mechanochemical aging approach to extracting chitin from European Green Crabs as a biomass waste valorization project.[148]
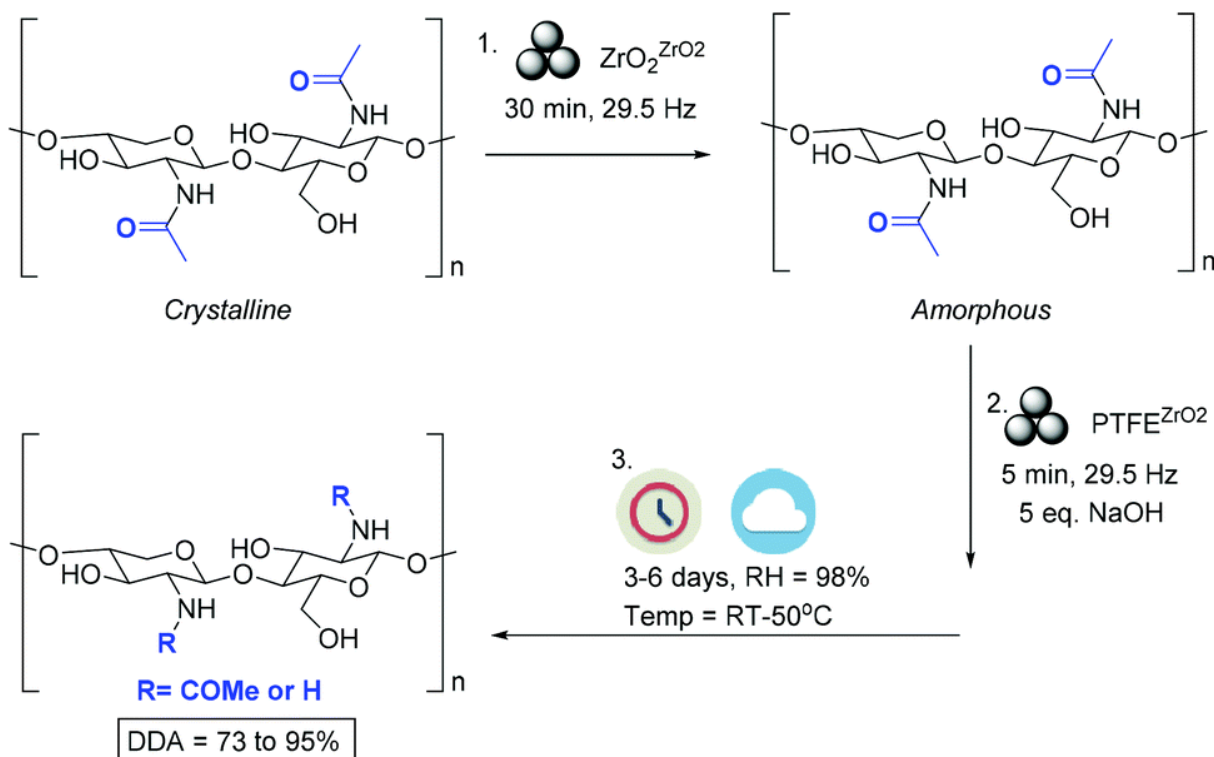


**Figure 1.34** Amorphization/aging-based chitin deacetylation experiments. DDA = [H]/([COMe] + [H]) × 100. Typical experimental conditions: chitin (200 mg) amorphized in a $ZrO_2$ jar with a $ZrO_2$ ball. Then chitin (105 mg), NaOH, 5 eq. (95 mg) based on the glucosamine unit, loaded into a PTFE jar with a $ZrO_2$ ball, followed by aging at 98% RH for 6 days. Reproduced from Ref. 147 with permission from the Royal Society of Chemistry.[147]

The mechanosynthesis of nickel phosphide,[56] iron selenide,[149] and iron nanoparticles have all reported success with aging techniques.[150] Moores, Friščić and co-workers reported a one-pot room-temperature mechanosynthesis of ultrasmall monodisperse bismuth sulfide nanoparticles ($Bi_2S_3$ NPs) through ball-milling $Bi(NO_3)_3 \cdot 5H_2O$ and L-cysteine in the presence of oleyamine (OA) or sodium 6-aminohexanoate (AHA) for organic or aqueous solubility, respectively (Figure 1.35).[151] When milled for 90 minutes and aged for 12 hours, particles of 2.09 ± 0.31 nm were observed by TEM; composition and ligand-shell structure were studied through XPS, PXRD, TGA, UV-visible spectroscopy, and matrix-assisted laser desorption ionization

time-of-flight mass spectroscopy (MALDI-TOF MS). Upon investigating the milled powder immediately after milling, the solid was found as a yellow paste that did not contain nanoparticles. Modifying the milling time or mechanical activation method did not appear to significantly affect the self-assembly of the nanoparticles. Milling only 5 minutes, hand grinding in a mortar and pestle, and scaling-up with a planetary ball mill all reproduced similar particles with only small variations in the average recorded size. This inexpensive and low-energy route to functional $Bi_2S_3$ NPs is a notable improvement over longer, hotter, and solvent-intensive hydrothermal methods.
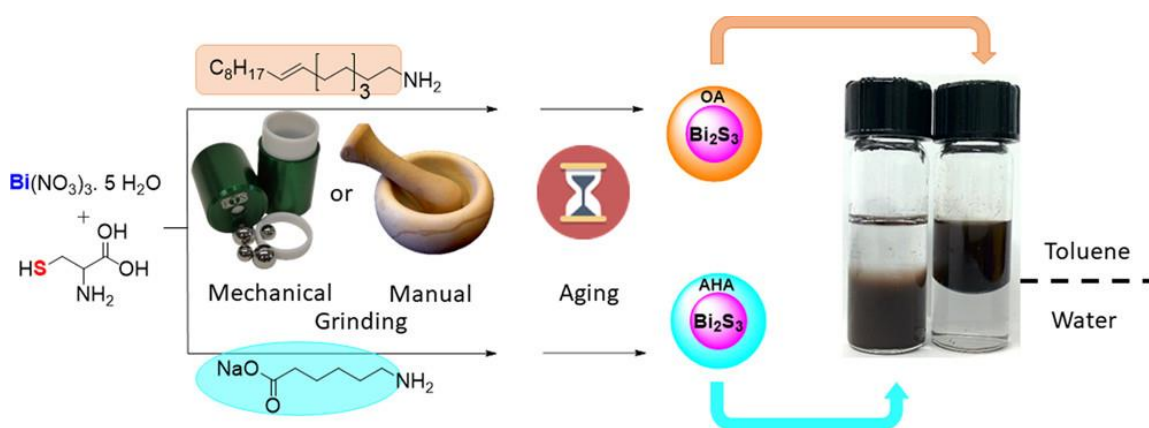


**Figure 1.35** Abstract figure for the mechanically activated solvent-free assembly of ultrasmall $Bi_2S_3$ NPs. Bismuth and sulfur reagents are milled with either a water-soluble or organic-soluble ligand, aged, and the resulting particles are dispersed into an aqueous or organic phase, respectively. Reprinted with permission from Ref. 151. Copyright 2017 American Chemical Society.[151]

As seen throughout this section, aging can be a powerful tool to modify reactivity, inducing novel chemical change or promoting pathways not achievable with solventless and solvent-based systems. The interest of aging to this thesis is perhaps unusual, as it centers on designing a solid-state bottom-up mechanosynthesis with aging not to accelerate but to decelerate reaction kinetics. A synthesis where nanoparticles grow out of a solid mixture at rest over some aging period would allow a much more extensive investigation than could be performed with an *in situ* milling reaction. The following two chapters are based on manuscripts from the research that I have undertaken during my master's degree here at McGill. Hopefully this introduction, that has covered topics of mechanochemistry and nanoparticle mechanosynthesis and chemical aging, has well prepared the reader to fully understand the work presented hereafter.

**1.5 References**

1. *IUPAC. Compendium of Chemical Terminology, 2nd ed. (the "Gold Book"). Compiled by A. D. McNaught and A. Wilkinson. Blackwell Scientific Publications, Oxford (1997). Online version (2019-) created by S. J. Chalk. ISBN 0-9678550-9-8.* [https://doi.org/10.1351/goldbook](https://doi.org/10.1351/goldbook)*.*

2. S. L. James and T. Friščić, *Chem. Soc. Rev.*, 2013, **42**, 7494-7496.

3. L. Takacs, *Chem. Soc. Rev.*, 2013, **42**, 7649-7659.

4. A. Michalchuk, E. Boldyreva, A. Belenguer, F. Emmerling and V. Boldyrev, *Front. Chem.*, 2021, DOI: 10.3389/fchem.2021.685789.

5. M. Bilke, P. Losch, O. Vozniuk, A. Bodach and F. Schüth, *J. Am. Chem. Soc.*, 2019, **141**, 11212-11218.

6. H. Xu, B. W. Zeiger and K. S. Suslick, *Chem. Soc. Rev.*, 2013, **42**, 2555-2567.

7. C. Bolm and J. G. Hernández, *Angew. Chem. Int. Ed.*, 2019, **58**, 3285-3299.

8. M. Xuan, C. Schumacher, C. Bolm, R. Göstl and A. Herrmann, *Adv. Sci.*, 2022, **9**, 2105497.

9. F. Gomollón-Bel, *Chem. Int.*, 2019, **41**, 12-17.

10. Joseph L. Howard, Q. Cao and D. L. Browne, *Chem. Sci.*, 2018, **9**, 3080-3094.

11. F. Cuccu, L. De Luca, F. Delogu, E. Colacino, N. Solin, R. Mocci and A. Porcheddu, *ChemSusChem*, **n/a**, e202200362.

12. J.-L. Do and T. Friščić, *ACS Cent. Sci.*, 2017, **3**, 13-19.

13. E. R. Caley and J. F. C. Richards, *Theophrastus On Stones*, Ohio State University, United States of America, 1956.

14. L. Takacs, *JOM*, 2000, **52**, 12-13.

15. S. Wu, M. A. Uddin, S. Nagano, M. Ozaki and E. Sasaoka, *Energy Fuels*, 2011, **25**, 144-153.

16. S.-E. Zhu, F. Li and G.-W. Wang, *Chem. Soc. Rev.*, 2013, **42**, 7535-7570.

17. S. Lebedkin, S. Ballenweg, J. Gross, R. Taylor and W. Krätschmer, *Tetrahedron Lett.*, 1995, **36**, 4971-4974.

18. A. B. Smith, H. Tokuyama, R. M. Strongin, G. T. Furst, W. J. Romanow, B. T. Chait, U. A. Mirza and I. Haller, *J. Am. Chem. Soc.*, 1995, **117**, 9359-9360.

19.  A. Gromov, S. Lebedkin, S. Ballenweg, A. G. Avent, R. Taylor and W. Krätschmer, *ChemComm*, 1997, DOI: 10.1039/A606794H, 209-210.

20.  G.-W. Wang, K. Komatsu, Y. Murata and M. Shiro, *Nature*, 1997, **387**, 583-586.

21.  A. A. L. Michalchuk, I. A. Tumanov, V. A. Drebushchak and E. V. Boldyreva, *Faraday Discuss.*, 2014, **170**, 311-335.

22.  M. J. Muñoz-Batista, D. Rodriguez-Padron, A. R. Puente-Santiago and R. Luque, *ACS Sustain. Chem. Eng.*, 2018, **6**, 9530-9544.

23.  H. M. Titi, J.-L. Do, A. J. Howarth, K. Nagapudi and T. Friščić, *Chem. Sci.*, 2020, **11**, 7578-7584.

24.  D. E. Crawford, L. A. Wright, S. L. James and A. P. Abbott, *ChemComm*, 2016, **52**, 4215-4218.

25.  Retsch, LABORATORY MILLS, GRINDERS & CRUSHERS for primary and fine size reduction, https://www.retsch.com/products/milling/, (accessed 2022-09-01, 2022).

26.  ResodynAcousticMixersInc., Lab RAM II, https://resodynmixers.com/product/labram-2/, (accessed 2022-09-01, 2022).

27.  ThermoFisherScientific, Lab Scale Twin-Screw Extrusion, https://www.thermofisher.com/ca/en/home/industrial/manufacturing-processing/extrusion-compounding-equipment/lab-scale-twin-screw-extruders.html, (accessed 2022-09-01, 2022).

28.  BransonUltrasonics, Ultrasonic Horn Catalog, https://www.emerson.com/documents/automation/catalog-ultrasonic-horn-branson-en-us-160126.pdf, (accessed 2022-09-01, 2022).

29.  B. Royal Institution of Great, *Quarterly Journal of Science, Literature and the Arts*, London, 1820.

30.  T. Friščić, I. Halasz, P. J. Beldon, A. M. Belenguer, F. Adams, S. A. J. Kimber, V. Honkimäki and R. E. Dinnebier, *Nat. Chem.*, 2013, **5**, 66-73.

31.  Y. Sawama, N. Yasukawa, K. Ban, R. Goto, M. Niikawa, Y. Monguchi, M. Itoh and H. Sajiki, *Org. Lett.*, 2018, **20**, 2892-2896.

32.  S. Hwang, S. Grätz and L. Borchardt, *ChemComm*, 2022, **58**, 1661-1671.

33.  L. Takacs, *J. Mater. Sci.*, 2004, **39**, 4987-4993.

34.   W. V. Spring, *Published in 1885 in Bruxelles by Hayez*, 1885.

35.   A. R. Ling and J. L. Baker, *J. Chem. Soc., Trans.*, 1893, **63**, 1314-1327.

36.   L. Takacs, *J. Mater. Sci.*, 2018, **53**, 13324-13330.

37.   M. Faraday, *Chemical manipulation : being instructions to students in chemistry, on the methods of performing experiments of demonstration or of research, with accuracy and success*, London : Murray, 1830.

38.   J. Andersen and J. Mack, *Green Chem.*, 2018, **20**, 1435-1443.

39.   P. Ying, J. Yu and W. Su, *Adv. Synth. Catal.*, 2021, **363**, 1246-1271.

40.   T. Friščić and W. Jones, *Cryst. Growth Des.*, 2009, **9**, 1621-1637.

41.   T. Friščić, S. L. Childs, S. A. A. Rizvi and W. Jones, *CrystEngComm*, 2009, **11**, 418-426.

42.   T. Friščić, *J. Mater. Chem.*, 2010, **20**, 7599-7605.

43.   A. V. Trask, N. Shan, W. D. S. Motherwell, W. Jones, S. Feng, R. B. H. Tan and K. J. Carpenter, *ChemComm*, 2005, DOI: 10.1039/B416980H, 880-882.

44.   W. H. Ojala and M. C. Etter, *J. Am. Chem. Soc.*, 1992, **114**, 10288-10293.

45.   C. Hardacre, H. Huang, S. L. James, M. E. Migaud, S. E. Norman and W. R. Pitner, *ChemComm*, 2011, **47**, 5846-5848.

46.   E. J. Amigues, C. Hardacre, G. Keane, M. E. Migaud, S. E. Norman and W. R. Pitner, *Green Chem.*, 2009, **11**, 1391-1396.

47.   A. Jayaraman, *Rev. Mod. Phys.*, 1983, **55**, 65-108.

48.   B. A. Steele, N. Goldman, I. Feng W. Kuo and M. P. Kroonblawd, *Chem. Sci.*, 2020, **11**, 7760-7771.

49.   W. Zhang and X. Zhang, *Prog. Polym. Sci.*, 2003, **28**, 1271-1295.

50.   M. Horst, J. Yang, J. Meisner, T. B. Kouznetsova, T. J. Martínez, S. L. Craig and Y. Xia, *J. Am. Chem. Soc.*, 2021, **143**, 12328-12334.

51.   B. S. Pladevall, A. de Aguirre and F. Maseras, *ChemSusChem*, 2021, **14**, 2763-2768.

52.   M. Ferguson, M. S. Moyano, G. A. Tribello, D. E. Crawford, E. M. Bringa, S. L. James, J. Kohanoff and M. G. Del Pópolo, *Chem. Sci.*, 2019, **10**, 2924-2929.

53.   Z. Chen, S. Lu, Q. Mao, A. Buekens, Y. Wang and J. Yan, *Environ. Sci. Pollut. Res.*, 2017, **24**, 24562-24571.

54.    H. L. Adams, M. T. Garvey, U. S. Ramasamy, Z. Ye, A. Martini and W. T. Tysoe, *J. Phys. Chem. C*, 2015, **119**, 7115-7123.

55.    B. Fiss, G. Douglas, M. Ferguson, J. Becerra, J. Valdez, T.-O. Do, T. Friščić and A. Moores, *ChemRxiv*, 2022, **This content is a preprint and has not been peer-reviewed.**

56.    B. G. Fiss, N.-N. Vu, G. Douglas, T.-O. Do, T. Friščić and A. Moores, *ACS Sustain. Chem. Eng.*, 2020, **8**, 12014-12024.

57.    J. Andersen and J. Mack, *Angew. Chem. Int. Ed.*, 2018, **57**, 13062-13065.

58.    B. P. Hutchings, D. E. Crawford, L. Gao, P. Hu and S. L. James, *Angew. Chem. Int. Ed.*, 2017, **56**, 15252-15256.

59.    J. G. Hernández, *Beilstein J. Org. Chem.*, 2017, **13**, 1463–1469.

60.    J. Yu, L. Zhang and G. Yan, *Adv. Synth. Catal.*, 2012, **354**, 2625-2628.

61.    D. Gracin, V. Štrukil, T. Friščić, I. Halasz and K. Užarević, *Angew. Chem. Int. Ed.*, 2014, **53**, 6193-6197.

62.    I. L. de Camargo, J. F. P. Lovo, R. Erbereli and C. A. Fortulan, *Mat. Res.*, 2019, **22**, (6).

63.    M. Broseghini, M. D'Incau, L. Gelisio, N. M. Pugno and P. Scardi, *Mater. Des.*, 2016, **110**, 365-374.

64.    R. Eckert, M. Felderhoff and F. Schüth, *Angew. Chem. Int. Ed.*, 2017, **56**, 2445-2448.

65.    C. F. Burmeister, R. Schmidt, K. Jacob, S. Breitung-Faes, A. Stolle and A. Kwade, *J. Chem. Eng.*, 2020, **396**, 124578.

66.    P. Baláž, 2008, DOI: 10.1007/978-3-540-74855-7_5, 257-296.

67.    P. G. McCormick and F. H. Froes, *JOM*, 1998, **50**, 61-65.

68.    J. S. Benjamin, *Sci. Am.*, 1976, **234**, 40-49.

69.    I. J. Corrans and J. E. Angove, *Miner. Eng.*, 1991, **4**, 763-776.

70.    J. S. Benjamin, *Metall. Mater. Trans. B.*, 1970, **1**, 2943-2951.

71.    C. Suryanarayana, *Prog. Mater. Sci.*, 2001, **46**, 1-184.

72.    in *Mineral Processing Design and Operations (Second Edition)*, eds. A. Gupta and D. Yan, Elsevier, Amsterdam, 2016, DOI: https://doi.org/10.1016/B978-0-444-63589-1.00011-3, pp. 317-355.

73.     E. T. Stamboliadis, *Miner. Eng.*, 2007, **20**, 140-145.

74.     Elias Th. Stamboliadis, *J. Mech. Behav. Mater.*, 2005, **16**, 363-378.

75.     U. Steinike and K. Tkáčová, *J. Mater. Synth. Process.*, 2000, **8**, 197-203.

76.     D. R. Askeland and P.P. Fulay, *Essentials of Material Science and Engineering Second Edition*, Cengage Learning, 2009.

77.     M. Senna, *ChemTexts*, 2017, **3**, 4.

78.     J. J. Gilman, *Science*, 1996, **274**, 65-65.

79.     L. P. Wolters and F. M. Bickelhaupt, *Wiley Interdiscip. Rev. Comput. Mol. Sci.*, 2015, **5**, 324-343.

80.     J. J. Gilman, *Czechoslov. J. Phys.*, 1995, **45**, 913-919.

81.     A. Zoltán Juhász, *Colloids Surf. A Physicochem. Eng. Asp.*, 1998, **141**, 449-462.

82.     M. K. Beyer and H. Clausen-Schaumann, *Chem. Rev.*, 2005, **105**, 2921-2948.

83.     I. Tole, K. Habermehl-Cwirzen and A. Cwirzen, *Mineral Petrol*, 2019, **113**, 449-462.

84.     R. Hüttenrauch, S. Fricke and P. Zielke, *Pharm. Res.*, 1985, **2**, 302-306.

85.     M. Erdemoğlu, M. Birinci, T. Uysal, E. Porgalı Tüzer and T. S. Barry, *J. Mater. Sci.*, 2018, **53**, 13801-13812.

86.     H. T. Baytekin, B. Baytekin, S. Huda, Z. Yavuz and B. A. Grzybowski, *J. Am. Chem. Soc.*, 2015, **137**, 1726-1729.

87.     L. Yang, A. Moores, T. Friščić and N. Provatas, *ACS Appl. Nano Mater.*, 2021, **4**, 1886-1897.

88.     M. Vert, Y. Doi, K.-H. Hellwich, M. Hess, P. Hodge, P. Kubisa, M. Rinaudo and F. Schué, *Pure Appl. Chem.*, 2012, **84**, 377-410.

89.     J. Potočnik, *OJEU*, 2011, L 275.

90.     C. Xu, S. De, A. M. Balu, M. Ojeda and R. Luque, *ChemComm*, 2015, **51**, 6698-6713.

91.     M. Kováčová, N. Daneu, Ľ. Tkáčiková, R. Búreš, E. Dutková, M. Stahorský, Z. L. Bujňáková and M. Baláž, *Nanomaterials*, 2020, **10**, 2119.

92.     M. J. Rak, T. Friščić and A. Moores, *RSC Adv.*, 2016, **6**, 58365-58370.

93.     D. Debnath, C. Kim, S. H. Kim and K. E. Geckeler, *Macromol. Rapid Commun.*, 2010, **31**, 549-553.

94. G. Baffou and R. Quidant, *Chem. Soc. Rev.*, 2014, **43**, 3898-3907.

95. Z. Li and Y. Yin, *Adv. Mater.*, 2019, **31**, 1807061.

96. S. Khizar, N. M. Ahmad, N. Zine, N. Jaffrezic-Renault, A. Errachid-el-salhi and A. Elaissari, *ACS Appl. Nano Mater.*, 2021, **4**, 4284-4306.

97. J. A. Barreto, W. O'Malley, M. Kubeil, B. Graham, H. Stephan and L. Spiccia, *Adv. Mater.*, 2011, **23**, H18-H40.

98. Z. Ma, J. Mohapatra, K. Wei, J. P. Liu and S. Sun, *Chem. Rev.*, 2021, DOI: 10.1021/acs.chemrev.1c00860.

99. M. Holzinger, A. Le Goff and S. Cosnier, *Front. Chem.*, 2014, **2**, 63.

100. J. Bai and B. Zhou, *Chem. Rev.*, 2014, **114**, 10131-10176.

101. T. Xiao, J. Huang, D. Wang, T. Meng and X. Yang, *Talanta*, 2020, **206**, 120210.

102. N. Baig, I. Kammakakam and W. Falath, *Adv. Mater.*, 2021, **2**, 1821-1871.

103. B. G. Fiss, A. J. Richard, G. Douglas, M. Kojic, T. Friščić and A. Moores, *Chem. Soc. Rev.*, 2021, **50**, 8279-8318.

104. P. F. M. de Oliveira, R. M. Torresi, F. Emmerling and P. H. C. Camargo, *J. Mater. Chem. A*, 2020, **8**, 16114-16141.

105. A. Heuer-Jungemann, N. Feliu, I. Bakaimi, M. Hamaly, A. Alkilany, I. Chakraborty, A. Masood, M. F. Casula, A. Kostopoulou, E. Oh, K. Susumu, M. H. Stewart, I. L. Medintz, E. Stratakis, W. J. Parak and A. G. Kanaras, *Chem. Rev.*, 2019, **119**, 4819-4880.

106. A. Eatemadi, H. Daraee, H. Karimkhanloo, M. Kouhi, N. Zarghami, A. Akbarzadeh, M. Abasi, Y. Hanifehpour and S. W. Joo, *Nanoscale Res. Lett.*, 2014, **9**, 393.

107. Y. Lin, K. A. Watson, S. Ghose, J. G. Smith, T. V. Williams, R. E. Crooks, W. Cao and J. W. Connell, *J. Phys. Chem. C*, 2009, **113**, 14858-14862.

108. Y. Chen, L. Soler, M. Armengol-Profitós, C. Xie, D. Crespo and J. Llorca, *Appl. Catal. B*, 2022, **309**, 121275.

109. J. Chen, H. Cai and T. Zhao, *Mol. Catal.*, 2022, **528**, 112518.

110. J. Beamish-Cook, K. Shankland, C. A. Murray and P. Vaqueiro, *Cryst. Growth Des.*, 2021, **21**, 3047-3055.

111. T. Friščić, in *Encyclopedia of Inorganic and Bioinorganic Chemistry*, DOI: https://doi.org/10.1002/9781119951438.eibc2202, pp. 1-19.

112. X. Li, Z. Zhang, W. Xiao, S. Deng, C. Chen and N. Zhang, *J. Mater. Chem. A*, 2019, **7**, 14504-14509.

113. M. J. Rak, T. Friščić and A. Moores, *Faraday Discuss.*, 2014, **170**, 155-167.

114. V. Apalangya, V. Rangari, B. Tiimob, S. Jeelani and T. Samuel, *Appl. Surf. Sci.*, 2014, **295**, 108-114.

115. W. H. Eisa, A. M. Abdelgawad and O. J. Rojas, *ACS Sustain. Chem. Eng.*, 2018, **6**, 3974-3983.

116. D. Debnath, S. H. Kim and K. E. Geckeler, *J. Mater. Chem.*, 2009, **19**, 8810-8816.

117. M. J. Rak, N. K. Saadé, T. Friščić and A. Moores, *Green Chem.*, 2014, **16**, 86-89.

118. P. F. M. de Oliveira, J. Quiroz, D. C. de Oliveira and P. H. C. Camargo, *ChemComm*, 2019, **55**, 14267-14270.

119. P. F. M. de Oliveira, A. A. L. Michalchuk, A. G. Buzanich, R. Bienert, R. M. Torresi, P. H. C. Camargo and F. Emmerling, *ChemComm*, 2020, **56**, 10329-10332.

120. J. Polte, *CrystEngComm*, 2015, **17**, 6809-6830.

121. N. T. K. Thanh, N. Maclean and S. Mahiddine, *Chem. Rev.*, 2014, **114**, 7610-7630.

122. V. K. LaMer and R. H. Dinegar, *J. Am. Chem. Soc.*, 1950, **72**, 4847-4854.

123. C. B. Whitehead, S. Özkar and R. G. Finke, *Chem. Mater.*, 2019, **31**, 7116-7132.

124. W. Ostwald, *Lehrbuch der allgemeinen chemie*, 1910.

125. W.-r. Lee, M. G. Kim, J.-r. Choi, J.-I. Park, S. J. Ko, S. J. Oh and J. Cheon, *J. Am. Chem. Soc.*, 2005, **127**, 16090-16097.

126. Q. Zhang, X. Peng, Y. Nie, Q. Zheng, J. Shangguan, C. Zhu, K. C. Bustillo, P. Ercius, L. Wang, D. T. Limmer and H. Zheng, *Nat. Commun.*, 2022, **13**, 2211.

127. M. A. Watzky and R. G. Finke, *J. Am. Chem. Soc.*, 1997, **119**, 10382-10400.

128. C. E. Marshall, *J. Polym. Sci.*, 1949, **4**, 413-414.

129. H. Zheng, R. K. Smith, Y.-w. Jun, C. Kisielowski, U. Dahmen and A. P. Alivisatos, *Science*, 2009, **324**, 1309-1312.

130. M. Niederberger and H. Cölfen, *Phys. Chem. Chem. Phys.*, 2006, **8**, 3271-3287.

131. X. Ji, X. Song, J. Li, Y. Bai, W. Yang and X. Peng, *J. Am. Chem. Soc.*, 2007, **129**, 13939-13948.

132. J. Polte, T. T. Ahner, F. Delissen, S. Sokolov, F. Emmerling, A. F. Thünemann and R. Kraehnert, *J. Am. Chem. Soc.*, 2010, **132**, 1296-1301.

133. T. Friščić, C. Mottillo and H. M. Titi, *Angew. Chem. Int. Ed.*, 2020, **59**, 1018-1029.

134. A. Moores, *Curr. Opin. Green Sustain.*, 2018, **12**, 33-37.

135. C. Mottillo and T. Friščić, *Molecules*, 2017, **22**, 144.

136. I. Huskić, C. B. Lennox and T. Friščić, *Green Chem.*, 2020, **22**, 5881-5901.

137. I. Huskic and T. Friscic, *Acta. Crystallogr. B. Struct. Sci. Cryst. Eng. Mater.*, 2018, **74**, 539-559.

138. W. A. Lucas and F. Hou, *Cryst. Growth Des.*, 2022, **22**, 3128-3137.

139. S. Kaabel, R. S. Stein, M. Fomitšenko, I. Järving, T. Friščić and R. Aav, *Angew. Chem. Int. Ed.*, 2019, **58**, 6230-6234.

140. S. Li, I. Huskić, N. Novendra, H. M. Titi, A. Navrotsky and T. Friščić, *ACS Omega*, 2019, **4**, 5486-5495.

141. H. Veith, C. Luebbert, N. Rodríguez-Hornedo and G. Sadowski, *Cryst. Growth Des.*, 2021, **21**, 4445-4455.

142. V. Štrukil, *ChemSusChem*, 2021, **14**, 330-338.

143. F. Qi, R. S. Stein and T. Friščić, *Green Chem.*, 2014, **16**, 121-132.

144. K. Užarević, T. C. Wang, S.-Y. Moon, A. M. Fidelli, J. T. Hupp, O. K. Farha and T. Friščić, *ChemComm*, 2016, **52**, 2133-2136.

145. X. Feng, C. Jia, J. Wang, X. Cao, P. Tang and W. Yuan, *Green Chem.*, 2015, **17**, 3740-3745.

146. M. J. Cliffe, C. Mottillo, R. S. Stein, D.-K. Bučar and T. Friščić, *Chem. Sci.*, 2012, **3**, 2495-2500.

147. T. Di Nardo, C. Hadad, A. Nguyen Van Nhien and A. Moores, *Green Chem.*, 2019, **21**, 3276-3285.

148. F. Hajiali, J. Vidal, T. Jin, L. C. de la Garza, M. Santos, G. Yang and A. Moores, *ACS Sustain. Chem. Eng.*, 2022, **10**, 11348-11357.

149. K. F. Ulbrich and C. E. M. Campos, *AIP Adv.*, 2019, **9**, 045311.

150.    I. Bekri-Abbes and E. Srasra, *Mater. Sci. Semicond. Process.*, 2015, **40**, 543-549.

151.    M. Y. Malca, H. Bao, T. Bastaille, N. K. Saadé, J. M. Kinsella, T. Friščić and A. Moores, *Chem. Mater.*, 2017, **29**, 7766-7773.

# 2    *In situ* Study of Au Nanoparticle Growth in a Mechanochemical-Aging-Based Method

This chapter is based upon a submitted article and is reprinted with permission from all co-authors. This work was derived from the idea of developing a highly resolvable aging mechanosynthesis reaction using gold as a trackable precursor and nanoparticle product. The goal was always to further our understanding of the mechanisms and kinetics of solid-state mechanochemical nanoparticle reduction and formation. Motivation for the initial experiments came from a best of both worlds concept that sought to combine a mechanosynthesis of ultrasmall size-controlled AuNPs with an aging mechanosynthesis of $Bi_2S_3$ NPs, both of which existed as published literature at the time. Preliminary trial and error experiments, and an optimization period with different chemical and physical conditions, led us to the final reaction presented in this manuscript. The work in this chapter details an extensive characterization of the reduction and formation stages of the first known AuNP aging mechanosynthesis. A selection of spectroscopic, crystallographic, and microscopic analysis techniques was used to qualitatively and quantitatively investigate the solid-state transformation of $AuCl_4^-$ to $Au^0$. Concepts of solid-state reactivity, bottom-up reductive-growth, and aging are all critical to understanding the fundamental scientific principals employed in this work.

A. J. Richard[†], M. Ferguson[†], B. G. Fiss, H. M. Titi, J. Valdez, N. Provatas, T. Friščić and A. Moores, *ChemRxiv*, 2022, This content is a preprint and has not been peer–reviewed.

[†] These authors contributed equally to this work.

## 2.1   Abstract

As we strive to perform chemical transformations in a more sustainable fashion, enabling reactions in the solid phase through mechanochemistry has emerged as a highly successful approach. Due to the wide-ranging applications of gold nanoparticles (AuNPs), mechanochemical strategies have already been employed for their synthesis. However, we have yet to fully understand the underlying processes surrounding gold salt reduction, nucleation and growth of AuNPs in the solid state. Herein, we present a mechanically activated aging synthesis of AuNPs, through a solid-state Turkevich reaction. Solid reactants are only briefly exposed to mechanical energy before being aged statically for a period of six weeks at different temperatures. This system offers a unique opportunity for *in situ* analysis of both reduction and nanoparticle formation processes. During the aging period the reaction was monitored using a combination of X-ray photoelectron spectroscopy, diffuse reflectance spectroscopy, powder X-ray diffraction and transmission electron microscopy to gain meaningful insights into the solid-state formation of gold nanoparticles.

## 2.2   Introduction

Mechanochemistry, defined as chemical reactions activated or driven by mechanical energy, has emerged as a highly successful alternative to conventional solution-based techniques. With benefits including the avoidance of bulk solvent, reduced reaction times, and higher yields,[1-3] mechanical activation enables more efficient, green, and sustainable chemical processes.[4-6] As such, mechanochemistry has been applied with success to a broad range of materials, including coordination polymers,[7] pharmaceutical co-crystals,[8] perovskites,[9] small molecule organics,[10] solid-state electrolytes,[11] and nanoparticles.[12, 13]

With applications ranging from catalysis and electronics to photodynamic therapies, there is increasing interest in developing sustainable routes to gold nanoparticle (AuNP).[14-16] In 2009, Debnath *et al.* reported the first mechanosynthesis of AuNPs by reducing $KAuCl_4$ with $NaBH_4$ in the presence of polyvinylpyrrolidone (PVP), with size control of $6 - 30$ nm.[17] Previous work from our group showed that ultrasmall AuNPs, with sizes ~1.5-2 nm, are produced by galvanic reduction of Au(III) in the presence of long chain amines.[18] The

Camargo group then developed a strategy to grow nanotadpoles in solution from such mechanochemically-accessed AuNPs.[19]

The mechanisms of nanoparticle nucleation and growth in solution are well studied, with multiple different theories proposed.[20] Examples include, the LaMer theory of burst nucleation,[21] Ostwald's ripening,[22] the Finke-Watzky two-step of simultaneous nucleation and growth,[23] the Brust-Shiffrin method,[24] and a four-step mechanism for AuNP synthesis.[25] However, the scope of these mechanisms is limited to solution synthesis and cannot be directly applied to processes in the solid state.[26, 27] Conversely, in the solid state, there is a good understanding of the kinetics of mechanochemical gold reduction, from in depth *in situ* studied by powder X-ray diffraction (PXRD)[28] and X-ray absorption spectroscopy (XAS).[29] Our group has also presented the first theoretical model for AuNP nucleation under mechanochemical conditions, which introduced a ballistic term as a way to parametrize the role of mechanical energy in the formation of amine-stabilized AuNPs.[30] Yet data on NP formation and transformation is still lacking.
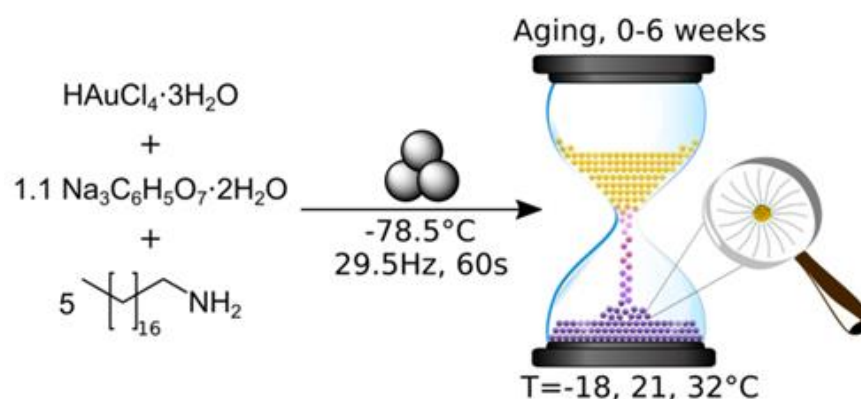


**Figure 2.1** Synthesis of amine-stabilized AuNPs through mechanical activation and subsequent aging.

Here, we provide direct, time-resolved, multi-scale information in the solid-state growth of AuNPs. This is achieved through a mechanically-activated aging process based on the brief introduction of mechanical energy followed by static equilibration. Such mechanochemically-activated aging approaches[31] have recently been used for the synthesis of metal-organic frameworks,[32] organometallic complexes,[33, 34] organic minerals,[35] polyaniline–clay nanocomposites,[36] as well as $Bi_2S_3$[37] and $Ag$[38] NPs.

The use of a mechanically-activated aging methodology enabled the observation of the solid-state growth process at the nanoparticle level, which is currently not possible using *in situ* methodologies while continuously milling. This granted us the opportunity to extract invaluable information on the mechanically-activated synthesis of amine-stabilized AuNPs using a modified solid-state Turkevich approach[39] (Figure 2.1), using X-ray photoelectron spectroscopy (XPS), diffuse reflectance spectroscopy (DRS), PXRD, transmission electron microscopy (TEM), and energy dispersive X-ray spectroscopy (EDXS). The judicious choice of reducing agent and modification of the environment allowed direct monitoring of AuNPs over a period of weeks, as well as the determination of underlying activation energy through variable temperature (VT) PXRD. This work represents the first extended nanoscale monitoring of AuNP growth in the solid state. Coupled with the determination of the underlying energetics it provides key insights for the understanding of mechanochemical reactivity.

## 2.3    Results and Discussion

In developing the optimal approach to AuNP synthesis by mechanically-activated aging, we explored ascorbic acid, hydroquinone, $NaBH_4$, and sodium citrate (NaCt) as reducing agents,[28] which were combined with the gold precursor $HAuCl_4 \cdot 3H_2O$ and octadecylamine (ODA) as the stabilizing ligand.[18] The reagents were milled for 90 min, aged for 1 day at room temperature (21°C), and analyzed by TEM. The best performing reducing agent was NaCt, providing the ability to reliably produce AuNPs after milling for 90 min and aging for one day at room temperature, in a reaction reminiscent of the solution-based Turkevitch method.[39] To capture the initial stages of the reaction, the milling time was reduced to 60 s to induce the reaction without driving the rapid formation of AuNPs. During aging, only background thermal energy is available to perpetuate the reaction. To understand its effect, freshly milled samples were stored in the dark at three different temperatures: -18 °C (low temperature, LT), 21 °C (room temperature, RT), and 32 °C (elevated temperature ET). The solid reaction mixtures were sampled on days, 0, 1, 4, 7, 15, 22, and 43 after milling, with each reaction performed in triplicate to ensure reproducibility.

Color changes of the milled powder provided qualitative information on reaction progress. Freshly milled powders exhibited a yellow color, which persisted for the LT aging sample (Supplemental Information (SI) Section 2.7 Figure 2.7a). The RT sample exhibited a gradual fading of the initial yellow color, and after seven days had a red/brown tinge (SI Section 2.7 Figure 2.7b). After two weeks, RT samples were purple in color, which deepened upon further aging. Such purple color is characteristic of the localized surface plasmon resonance (LSPR) exhibited by AuNPs.[40] For the ET sample, the yellow color had completely faded after one day, and after four days the characteristic purple color of AuNPs was attained (SI Section 2.7 Figure 2.7c). The purple color intensified upon aging, and after two weeks the powder was almost black. This indicates that the reaction was significantly accelerated with increased temperature.

XPS was employed to monitor the reduction of Au(III) to Au(0) by tracking intensity changes in the Au 4f doublets. Raw XPS spectra were deconvoluted into the $4f_{7/2}$ and $4f_{4/2}$ doublets for Au(III) and Au(0), normalized to the Au(III) $4f_{7/2}$ peak at ~87 eV of freshly milled powder. While the standard major-peak binding energy value for bulk Au(III) and Au(0) is 86 and 84 eV respectively, peak position may vary with the particle size and surroundings of the Au species.[41] Knowing that our XPS Au signal is up-shifted between 0.2 – 1 eV from the bulk standards, and knowing from DRS and TEM analyses that AuNPs are present in the milled powder, it may be concluded that the slight shift observed in XPS may be due to the fact gold is present as nanoparticles. RT samples showed a consistent, gradual decrease in the Au(III) signal accompanied by a proportional increase in Au(0) signal (Figure 2a), suggesting a slow, continuous reaction of $HAuCl_4 \cdot 3H_2O$ during the aging process. Little change is observed for the LT sample, whereas the ET sample exhibited a much faster progression of the Au(III) reduction (SI Section 2.7 Figure 2.11).
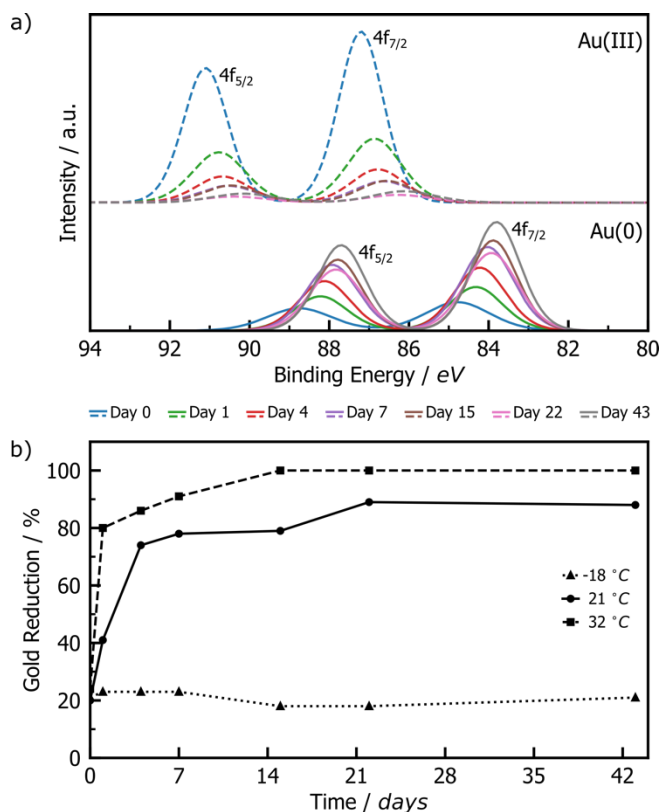
**Figure 2.2** a) Comparison of XPS data for Au(III) (dashed line) and Au(0) (solid line) 4f doublets of product AuNPs after aging at room temperature for 0 (blue), 1 (green), 4 (red), 7 (violet), 15 (brown), 22 (pink), and 43 (grey) days. A standard error of 0.74 percentage points in the percent Au(0) or Au(III) species was calculated. b) Plot of the percentage of Au(III) reduced to Au(0) upon aging at -18 °C (triangles), 21 °C (circles), 32 °C (squares).

Integration of the normalized doublets gave access to the Au(III)/Au(0) ratio by which the percentage reduction could be quantified (Figure 2.2b). For the ET sample, the reduction is initially rapid, reaching completion after 15 days, while the RT sample achieved ca. 90% reduction over the entire explored aging period of 43 days. Consistent with the visual inspection of the powders, little to no reduction occurred in the LT sample. All samples show ca. 20% reduction immediately after milling, which can be attributed to the previously reported photoreduction of Au(III) salts upon XPS analysis[42, 43] (SI Section 2.7.2b).

The growth of AuNPs in the bulk powder during aging was followed by DRS and PXRD. Specifically, DRS was used to follow changes in absorbance (converted from percent reflectance, SI 2.7.1) in the region 500 – 600 nm, where AuNPs, of a minimum diameter of 2 nm, exhibit characteristic absorption due to LSPR.[44-46] The LT samples did not show

significant absorbance in the visible region throughout the aging period (SI Section 2.7 Figure 2.14). Both RT and ET samples featured strong absorbance bands at ca. 550 nm, which appeared during aging (Figure 2.3a,b). The normalized absorbance intensity increased gradually for RT samples during the full 43 days aging period, whereas for the ET sample the intensity rose sharply, reaching its maximum at day four. The final position of the absorbance maximum for ET samples (545 nm) was found to be red-shifted by 4 nm compared to RT samples (541 nm), a shift that may be caused by one or multiple different sources including larger average NP sizes, agglomeration, a higher polydispersity, and a changing refractive index.[47-49] The ET samples exhibited strong broadening of the absorbance band for up to 15 days and were found by TEM to contain larger and more polydisperse AuNPs (SI Section 2.7 Figure 2.27). While nothing can currently be said on agglomeration or refractive index, they cannot be excluded as potential sources of red-shifting.
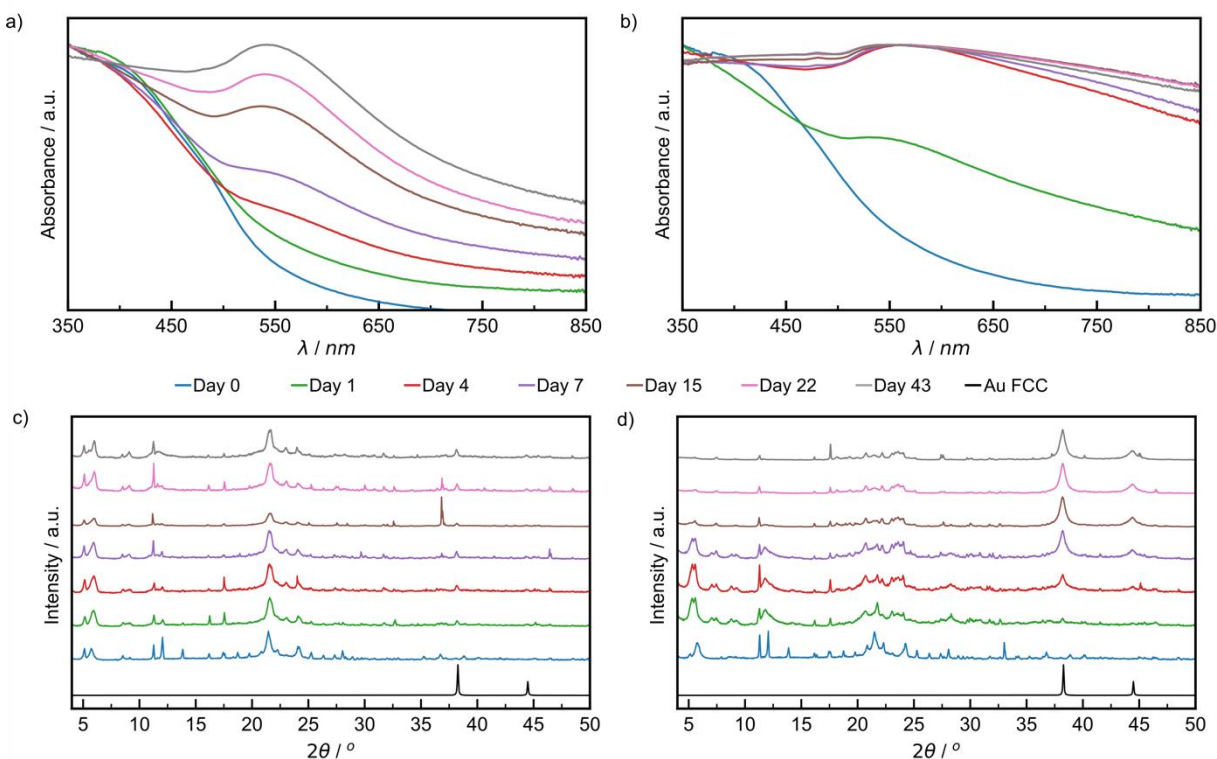


**Figure 2.3** Comparison of DRS data of: a) RT sample aged at 21 °C, b) ET sample aged at 32 °C. Comparison of PXRD patterns for: c) RT sample and d) ET sample. All samples were analyzed after 0 (blue), 1 (green), 4 (red), 7 (violet), 15 (brown), 22 (pink), and 43 (grey) days of aging. The simulated pattern for elemental gold in the FCC lattice in c) and d) is shown in black.[50]

Similar trends for AuNP growth were observed by PXRD, following the intensity of the (111) X-ray reflection of gold at $2\theta = 38.2°$.[50] This characteristic X-ray reflection was not evident for the LT sample (SI Section 2.7 Figure 2.18) indicating a lack of NP growth. For the RT samples (Figure 2.3c), the (111) X-ray reflection was observable after one day of aging and increased in intensity during the remaining six weeks of aging. The (111) reflection was observable after one day for ET samples and continued to increase in intensity substantially for the remainder of the aging period (Figure 2.3d). Consistent with visual inspection, XPS, and DRS, PXRD observations indicate a strong temperature dependence of the growth of NPs in a mechanically-activated aging process.

Notably, the (200) X-ray reflection of gold ($2\theta = 44.4°$) was observable for ET samples, permitting the investigation of particle morphology via the ratio of the intensities of (200) and (111) reflections ($I_{(200)}/I_{(111)}$).[51] It was previously shown that Au metal exhibits $I_{(200)}/I_{(111)}$ of 0.53, while nanocubes, icosahedrons and tetrahedrons exhibit values of 1.93, 0.31, and 0.25, respectively. The herein calculated $I_{(200)}/I_{(111)}$ ratio was 0.33, suggesting predominantly spherical AuNPs.[51] This morphology was directly observed under high resolution TEM in fully aged samples (SI Section 2.7 Figure 2.21). Therefore, the broadening of absorbance bands observed in DRS data is more likely due to polydisperse size distributions.

TEM analyses were used to probe the effect of aging temperature on the size and morphology of AuNPs to be investigated. We first selected the solution drop-cast method to prep TEM sample, because it is common, simple and leads to clean images through the efficient removal of excess material. Specifically, solid phase aged samples were dispersed rapidly in toluene and the resulting solution was drop-casted onto the TEM grid. First, we tested this method on samples without mechanical activation or aging. The three reactants were stirred in toluene, in which they are insoluble, for 120 s in a solid-to-liquid ratio of 1 mg mL$^{-1}$. Analysis of a sample taken from this solution revealed the presence of NPs with an average particle diameter (Ø) of 4.1 ± 1.7 nm (SI Section 2.7 Figure 2.22). Particles of Ø ≈ 5 nm observed by scanning transmission electron microscopy coupled with a high-angle annular dark field detector (STEM-HAADF) were confirmed to be AuNPs by energy dispersive X-ray spectroscopy (EDXS). Signals corresponding to Au

are correlated to the particles observed in the STEM-HAADF image (SI Section 2.7 Figure 2.23) whereas the Cl signal is evenly dispersed throughout the imaged area. Samples taken directly after milling showed a similar distribution of particles to the control study, though approximately 3 nm larger in diameter ($\varnothing$ = 7.0 ± 1.9 nm). As these two initial samples were featuring NPs, the particle sizing and analyses were contextualized with the trends observed in the solid-state analyses, XPS, DRS, and PXRD (Figure 2.2 and Figure 2.3). In particular, the absence of LSPR (DRS) and Au reduction (XPS) before aging suggests that the particles observed in the blank tests above are not made of Au(0).

For freshly milled powder and after one day of aging (Figure 2.4a and Figure 2.4b) images reveal a small number of large non-spherical particles whose diameter is approximately 20 nm (SI Section 2.7 Figure 2.24). Given the very short amount of time that the particles are in suspension, it was suspected that these large particles are predominantly comprised of unreacted $HAuCl_4$ precursor. STEM-HAADF images coupled with EDXS elemental mapping confirmed that particles of $\varnothing \geq$ 15 nm with overlapping Au and Cl signals that correlate to the particles observed in the dark field image (SI Section 2.7 Figure 2.25).

Ultrasmall AuNPs, $\varnothing$ = 1.2 ± 0.2 nm, were initially observed by TEM after four days of aging (Figure 2.4c). PXRD analysis, however, revealed a small reflection for metallic gold after just one day of aging. Therefore, we believe that ultrasmall AuNPs are present in the sample after one day of aging but in such low concentration that we could not spot them reliably by TEM. Between one and four days of aging the amount of Au(0) in the sample increases by approximately 35 % (Figure 2.2b). This causes the formation of ultrasmall AuNPs in sufficient quantity to be encountered during TEM studies. After one week of aging, the ultrasmall NPs are still visible, exhibiting a slightly larger diameter, and account for a larger fraction of the overall population (Figure 2.4d,e). Representative TEM images for RT samples (Figure 2.4) taken during the first week of aging confirm the AuNP icosahedral geometry suggested by the $I_{(200)}/I_{(111)}$ ratio calculated from the PXRD data. After two weeks of aging, the ultrasmall NP population was greatly reduced while accompanied by an increase in diameter, $\varnothing$ = 2.1 ± 0.1 nm. At the same time, the population with $\varnothing \approx$ 20 nm disappears which we ascribe to the consumption of $HAuCl_4$.

After 22 days of aging RT samples show a multimodal distribution of AuNPs with Ø $\leq$ 6.5 nm. Previously observed ultrasmall particles had grown since their first appearance in a non-uniform fashion. Finally, after six weeks the AuNPs were observed in a bimodal distribution with Ø = 5.8 ± 1.9 nm and 11.9 ± 2.6 nm.
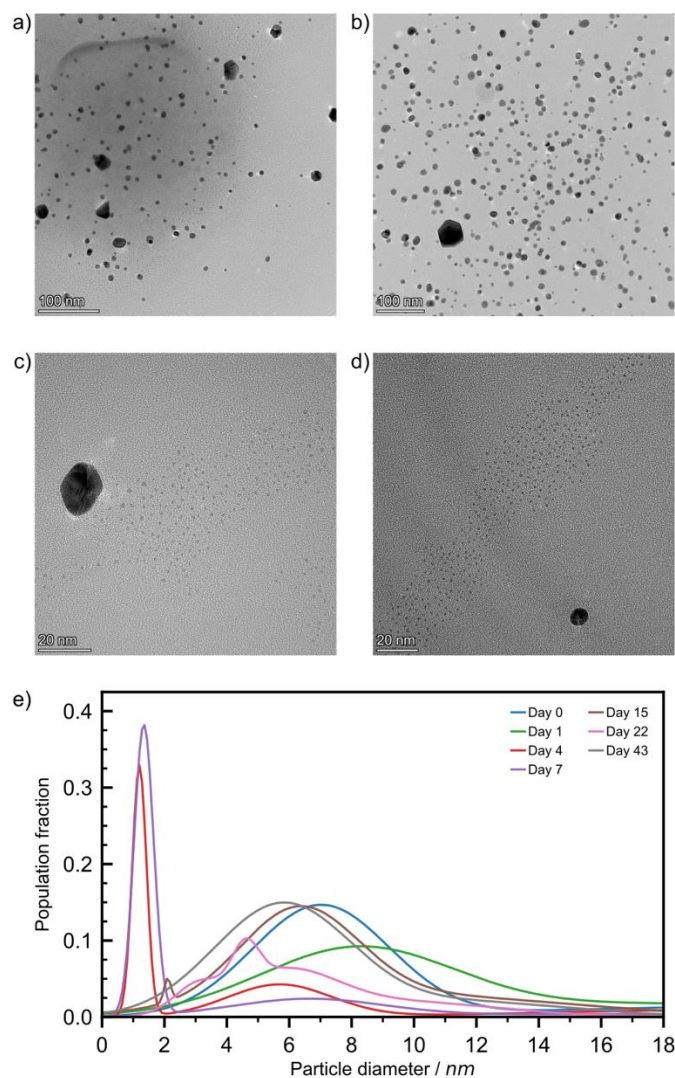


**Figure 2.4** Bright field TEM images from solution drop-cast preparation of the RT sample when aged for: a) 0, b) 1, c) 4, and d) 7 days at magnifications of x120 k, x94 k, x500 k, and x390 k, respectively. e) The AuNP size population distributions for the RT sample after aging for 0 (blue), 1 (green), 4 (red), 7 (violet), 15 (brown), 22 (pink), and 43 (grey) days.

For ET samples, TEM analysis confirms the acceleration of the reaction suggested by XPS, DRS and PXRD data. Particles after one day of aging are slightly smaller, Ø of 4.3 ± 0.9 nm, than those visible immediately after milling, Ø of 6.8 ± 1.8 nm (SI Section 2.7 Table 2.3). We believe that these particles are the result of ultrasmall AuNPs that had

formed and already grown between sampling times. Additionally, the secondary distribution at Ø ≈ 20 nm, attributed to the $HAuCl_4$ precursor disappeared, consistent with the reduction indicated by XPS (Figure 2.2b). Throughout the remainder of the aging period the particles continued to grow with multi-modal distributions. After six weeks a quad modal distribution was observed where the smallest particles had an average Ø of 6.6 ± 0.2 nm while the largest particles had a Ø of 20.3 ± 7.5 nm. Therefore, the broadening of the absorbance band in DRS spectra are caused by the polydispersity of the resulting AuNPs. While aging at elevated temperatures is advantageous for the rate of NP growth, it appears to be offset by a loss of size control. Populations profiles exhibited by LT aged samples did not show any significant growth compared to the day zero starting point (SI Section 2.7 Figure 2.26). It appears that the reaction is effectively paused at these temperatures.

While the drop-cast method was useful for statistical NP size analysis, we wanted to verify if the introduction of a solvent in the TEM sampling was not causing potential liquid state effects. We thus turned to solid-state TEM sampling to confirm that AuNPs were formed in the absence of bulk solvent. Samples were prepared by impregnating a SiOx substrate bearing (30 nm thick) copper grid with freshly milled powder. Impregnation was achieved by dragging the grid through the loose powder, after which the grid was cleaned with pressured air to remove excess material.

The resulting samples were studied using STEM-HAADF. A freshly milled powder sample featured large particles in the 100 nm range. Figure 2.5a shows a representative example, as a large, non-spherical particle of a maximum diameter ≈ 125 nm. Elemental maps of Au and Cl were constructed for this image using EDXS. The overlapping signals for Au and Cl in the EDXS analysis (Figure 2.5b,c) revealed it as $HAuCl_4$ precursor, consistent with previous analyses.
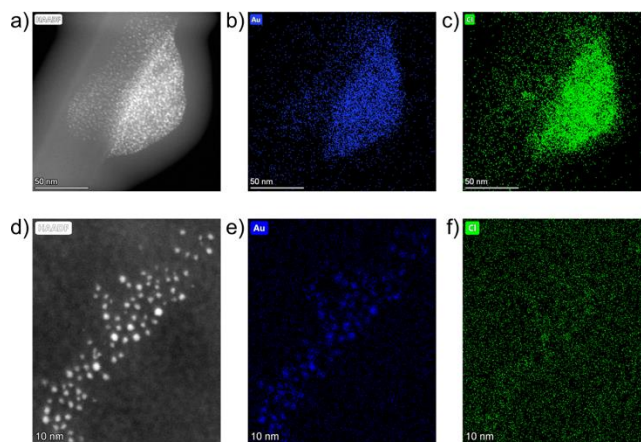
**Figure 2.5** Solid-state STEM-HAADF images and EDXS elemental maps for Au and Cl (left to right, respectively) for: (a-c) freshly milled powder at x186 k magnification and (d-f) for the powder after seven days of aging at room temperature at x740 k magnification.

After one week of aging another grid was prepared and ultrasmall AuNPs were observed in a monodisperse distribution, with Ø of 1.5 ± 0.4 nm. Elemental mapping showed localized concentrations of Au, consistent with the bright spots on the STEM-HAADF image (Figure 2.5d,e). Cl signals (Figure 2.5f) were dispersed throughout the region with minimal localized concentrations. This confirms that ultrasmall AuNPs have formed in the solid phase, and not as a result of the drop-cast process. The XPS, DRS, PXRD and TEM studies demonstrate that AuNPs can be synthesized in the solid phase through an aging process and that this reaction is temperature dependant.

The *in situ* setup enabled by this aging process allows to study the kinetics of AuNPs formation in the solid phase. Using DRS data (*vide supra*), we have plotted the intensity of the 541 nm LSPR peak for samples aged at 21 °C over 43 days (Figure 2.6a). At the onset of the reaction, between day 0 and 15, the LSPR signal grew in a linear fashion at a rate of $3.68 \times 10^{-7}$ s$^{-1}$. This is comparable to the initial rate of $4.48 \times 10^{-7}$ s$^{-1}$ at 24 °C observed during the initial 2.5 hours of the variable temperature (VT) PXRD experiment in Figure 2.6c. Past day 15, the curve saturated, as the reaction came to completion. This overall sigmoidal curve is reminiscent of solution based nanoparticle growth mechanisms, whereby autocatalytic effects are at play.[52] The curve is also a close match to the sigmoidal curve observed by the James group for mechanochemical reactions, in which feedback between rheological/mechanical effects and chemistry are at play to explain the kinetic is not simply first order.[53] Details on the fitting of the sigmoidal curve can be found

in SI 2.7.2c. To deepen our understanding, we focused on the initial stage of the reaction and performed two VT PXRD studies, focusing on the intensity of the (111) reflection of metallic gold ($2\theta = 38.2°$). Firstly, we acquired 121 patterns over 60 hours for three separate experiments performed with the thermo-coupled stage held at a constant temperature (30, 35, and 40 °C).
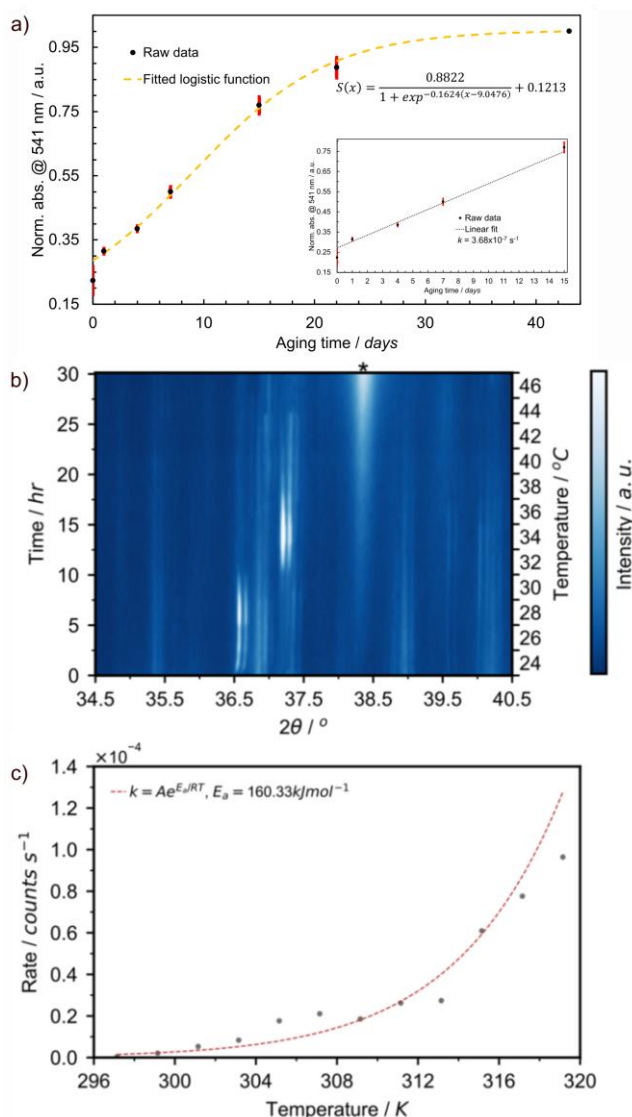


**Figure 2.6** a) Plot of normalized absorbance resulting from localized surface plasmon resonance at 541 nm for samples aged at 21 °C (black circles with red standard error bars) with a fitted logistic function (orange dashed lines). Insert shows the linear fitting of data points between 0 and 15 days of aging to obtain an initial rate of growth. b) *In situ* variable temperature PXRD analysis of AuNP formation between 24 and 46 °C where * denotes the reflection corresponding to the (111) lattice plane of elemental gold. c) Plot of the rate of increase in intensity of the reflection at $2\theta = 38.2°$ for each temperature (grey circles) with the model Arrhenius plot with parameters taken from the resolved data.

For each temperature, the reflection grew linearly, as suggested in the DRS experiment, and the rate of AuNP growth increased with temperature (SI Section 2.7 Figure 2.29a). The activation energy for AuNP growth in the presented mechanically-activated aging process was found to be 158.43 kJmol$^{-1}$.

A second VT-PXRD study was performed to confirm the exponential relationship between AuNP growth rate and aging temperature. Therein, the thermo-coupled stage was initially set to 24 °C and increased by 2 °C every 2.5 hours during a period of 30 hours with five measurements performed at each temperature. The (111) reflection, indicated by '*', increased gradually initially and proceeded to intensify more rapidly as the temperature increased (Figure 2.6b). The intensity of the reflection was measured using the five scans at each temperature and, thus, 12 rates were obtained. In this case, the activation energy for amine-stabilized AuNP growth in the solid state was found to be equal to 160.33 kJmol$^{-1}$ (SI Section 2.7 Figure 2.30). The solved Arrhenius equation was in good agreement with the 12 individually obtained growth rates (Figure 2.6c). This confirmed the exponential increase in AuNP growth rate with aging temperature. Further details on the VT-PXRD studies performed can be found in the supporting information (2.7.2f). Given the low discrepancy between the two studies (1.2 %) we calculated the average activation energy of AuNP growth in a solid-state aging process to be 159.38 kJmol$^{-1}$. Such activation energies are fairly high and explain that the reaction under these conditions happens over a few weeks. This study confirms that AuNPs can be grown under aging conditions and that the kinetics of the reaction follow a sigmoidal pattern. Initial reaction rates can be measured and feature an exponential relationship to temperature.

## 2.4    Conclusion

Herein, we have presented the mechanically-activated aging synthesis of AuNPs using a Turkevich method that was modified for the solid-state. Using octadecylamine as the stabilizing agent, $HAuCl_4 \cdot 3H_2O$ and trisodium citrate dihydrate were milled together for 60 s at -78.5 °C using a vibrational ball mill to initiate the reaction. After brief milling, the resulting powders were aged in the dark at -18, 21, and 32 °C for a period of six weeks, during which the powders were frequently analyzed using, XPS, DRS, PXRD, and TEM.

Aging at low temperature (-18 °C) effectively froze the reaction, with no observed changes for the duration of the aging period. Strong absorbance of visible light and the appearance of metallic gold lattice place reflections confirmed that AuNPs were produced in samples aged at room temperature (21 °C) and elevated temperature (32 °C). At room temperature, the process was gradual and occurred throughout the whole aging period whereas at elevated temperature the process was significantly accelerated. This was confirmed by TEM images of the samples with grids made using the drop-cast technique. Ultrasmall AuNPs where found after four days after aging at room temperature while at elevated temperatures AuNPs were observed after just one day of aging. The production of AuNPs in the absence of suspension in bulk solution was confirmed using a solid-state impregnation preparation of TEM grids that were analyzed using STEM-HAADF coupled EDXS. Therein, the formation of ultrasmall AuNPs was confirmed after a seven-day aging period. Multiple in situ temperature-controlled PXRD experiments were performed to investigate the temperature dependence of the reaction. It was found that at constant temperatures the AuNP formation is linear in fashion. When the temperature was gradually increased during the aging process the formation rate increased exponentially with temperature. The Arrhenius equation was solved from each of the in situ PXRD aging studies leading to the determination of the activation energy for AuNP formation in a solid-state aging process. With a 1.2 % discrepancy between the results, the average activation energy for the process was 159.38 kJmol$^{-1}$. Thus, by extending the timeframe of the reaction, the mechanically activated aging approach has demonstrated an ability to provide previously not accessible, macroscopic and nanoscopic details on the course of mechanically-activated AuNP synthesis.

## 2.5    Experimental Section/Methods

Tetrachloroauric(III) acid trihydrate (ACS reagent, ≥49.0% Au basis), 1-octadecylamine (technical grade, 90%), and trisodium citrate dihydrate (ACS reagent, ≥99.0%) were obtained from Sigma Aldrich and used without further purification. A 15 ml zirconia milling jar (Form-Tech Scientific), 10 mm (3.0 g) diameter zirconia milling ball, tetrachloroauric(III) acid trihydrate (0.143 g, 0.363 mmol), trisodium citrate dihydrate (0.118 g, 0.400 mmol), and 1-octadecylamine (0.490 g, 1.816 mmol) were chilled

separately over dry ice for 60 minutes to ensure a consistent starting point for each reaction. The milling jar was charged with the milling ball and solid reactants and subsequently set to shake on a Retsch MM400 mixer mill for 60 s at 29.5 Hz. All millings were performed under air. The resulting free-flowing yellow powder was transferred to sample vial, covered and stored at the desired temperature. Note: given the potential for galvanic reduction, tetrachloroauric(III) acid trihydrate and the post-milling powder were manipulated with a PTFE coated spatula. For room temperature aging, 21 °C, samples were stored inside an opaque closed box in the research lab. Low temperature aging samples were stored freezer with an internal temperature of -18 °C. For aging at elevated temperature, the samples were covered and stored in an oven with an internal temperature of 32 °C (oven thermostat set to 45 °C). All reactions were performed in triplicate to ensure reproducibility. See the Supporting Information for details of XPS, DRS, PXRD, and TEM analysis.

## 2.6    References

1.  James, S. L., Adams, C. J., Bolm, C., Braga, D., Collier, P., Friščić, T., Grepioni, F., Harris, K. D., Hyett, G., Jones, W., Krebs, A., Mack, J., Maini, L., Orpen, A. G., Parkin, I. P., Shearouse, W. C., Steed, J. W., Waddell, D. C., *Chem. Soc. Rev.* **2012,** *41* (1), 413-47. DOI 10.1039/c1cs15171a.

2.  Friščić, T., Mottillo, C., Titi, H. M., *Angew. Chem., Int. Ed.* **2020,** *59* (3), 1018-1029. DOI 10.1002/anie.201906755.

3.  Colacino, E., Delogu, F., Hanusa, T., *ACS Sustainable Chem. Eng.* **2021,** *9* (32), 10662-10663. DOI 10.1021/acssuschemeng.1c04390.

4.  McNaught, A. D., Wilkinson, A., *IUPAC. Compendium of Chemical Terminology, 2nd ed. (the "Gold Book")*. Blackwell Scientific Publications: Oxford, **1997**.

5.  Takacs, L., *Acta Phys. Pol., A* **2014,** *126* (4), 1040-1043. DOI 10.12693/APhysPolA.126.1040.

6.  Howard, J. L., Cao, Q., Browne, D. L., *Chem. Sci.* **2018,** *9* (12), 3080-3094. DOI 10.1039/c7sc05371a.

7.  Friščić, T., Halasz, I., Štrukil, V., Eckert-Maksić, M., Dinnebier, R. E., *Croat. Chem. Acta* **2012,** *85* (3), 367-378. DOI 10.5562/cca2014.

8.  Solares-Briones, M., Coyote-Dotor, G., Páez-Franco, J. C., Zermeño-Ortega, M. R., de la, O. C. C. M., Canseco-González, D., Avila-Sorrosa, A., Morales-Morales, D., Germán-Acacio, J. M., *Pharmaceutics* **2021,** *13* (6). DOI 10.3390/pharmaceutics13060790.

9.  Palazon, F., El Ajjouri, Y., Bolink, H. J., *Adv. Energy Mater.* **2019,** *10* (13). DOI 10.1002/aenm.201902499.

10. Andersen, J. M., Mack, J., *Chem. Sci.* **2017,** *8* (8), 5447-5453. DOI 10.1039/c7sc00538e.

11. Schlem, R., Burmeister, C. F., Michalowski, P., Ohno, S., Dewald, G. F., Kwade, A., Zeier, W. G., *Adv. Energy Mater.* **2021,** *11* (30). DOI 10.1002/aenm.202101022.

12. Baláž, P., Achimovičová, M., Baláž, M., Billik, P., Cherkezova-Zheleva, Z., Criado, J. M., Delogu, F., Dutková, E., Gaffet, E., Gotor, F. J., Kumar, R., Mitov, I., Rojac, T.,

Senna, M., Streletskii, A., Wieczorek-Ciurowa, K., *Chem. Soc. Rev.* **2013,** *42* (18), 7571-637. DOI 10.1039/c3cs35468g.

13. de Oliveira, P. F. M., Torresi, R. M., Emmerling, F., Camargo, P. H. C., *J. Mater. Chem. A* **2020,** *8* (32), 16114-16141. DOI 10.1039/d0ta05183g.

14. Elahi, N., Kamali, M., Baghersad, M. H., *Talanta* **2018,** *184*, 537-556. DOI 10.1016/j.talanta.2018.02.088.

15. Ghosh, P., Han, G., De, M., Kim, C. K., Rotello, V. M., *Adv. Drug Delivery Rev.* **2008,** *60* (11), 1307-1315. DOI 10.1016/j.addr.2008.03.016.

16. Guo, S., Wang, E., *Anal. Chim. Acta* **2007,** *598* (2), 181-92. DOI 10.1016/j.aca.2007.07.054.

17. Debnath, D., Kim, S. H., Geckeler, K. E., *J. Mater. Chem.* **2009,** *19* (46). DOI 10.1039/b905260g.

18. Rak, M. J., Saadé, N. K., Friščić, T., Moores, A., *Green Chem.* **2014,** *16* (1), 86-89. DOI 10.1039/c3gc41827h.

19. de Oliveira, P. F. M., Quiroz, J., de Oliveira, D. C., Camargo, P. H. C., *Chem. Commun.* **2019,** *55* (95), 14267-14270. DOI 10.1039/c9cc06199a.

20. Thanh, N. T., Maclean, N., Mahiddine, S., *Chem. Rev.* **2014,** *114* (15), 7610-30. DOI 10.1021/cr400544s.

21. LaMer, V. K., Dinegar, R. H., *J. Am. Chem. Soc.* **2002,** *72* (11), 4847-4854. DOI 10.1021/ja01167a001.

22. Ostwald, W., *Lehrbruck der Allgemeinen Chemie*. Engelmann: Leipzig, Germany, **1896**; Vol. 2 part 1.

23. Watzky, M. A., Finke, R. G., *J. Am. Chem. Soc.* **1997,** *119* (43), 10382-10400. DOI 10.1021/ja9705102.

24. Goulet, P. J., Lennox, R. B., *J. Am. Chem. Soc.* **2010,** *132* (28), 9582-4. DOI 10.1021/ja104011b.

25. Polte, J., Ahner, T. T., Delissen, F., Sokolov, S., Emmerling, F., Thunemann, A. F., Kraehnert, R., *J. Am. Chem. Soc.* **2010,** *132* (4), 1296-301. DOI 10.1021/ja906506j.

26. Daruich De Souza, C., Ribeiro Nogueira, B., Rostelato, M. E. C. M., *J. Alloys Compd.* **2019,** *798*, 714-740. DOI 10.1016/j.jallcom.2019.05.153.

27. Sengani, M., Grumezescu, A. M., Rajeswari, V. D., *OpenNano* **2017,** *2*, 37-46. DOI 10.1016/j.onano.2017.07.001.

28. de Oliveira, P. F. M., Michalchuk, A. A. L., Marquardt, J., Feiler, T., Prinz, C., Torresi, R. M., Camargo, P. H. C., Emmerling, F., *CrystEngComm* **2020,** *22* (38), 6261-6267. DOI 10.1039/d0ce00826e.

29. de Oliveira, P. F. M., Michalchuk, A. A. L., Buzanich, A. G., Bienert, R., Torresi, R. M., Camargo, P. H. C., Emmerling, F., *Chem. Commun.* **2020,** *56* (71), 10329-10332. DOI 10.1039/d0cc03862h.

30. Yang, L., Moores, A., Friščić, T., Provatas, N., *ACS Appl. Nano Mater.* **2021,** *4* (2), 1886-1897. DOI 10.1021/acsanm.0c03255.

31. Mottillo, C., Friščić, T., *Molecules* **2017,** *22* (1). DOI 10.3390/molecules22010144.

32. O'Keefe, C. A., Mottillo, C., Vainauskas, J., Fábián, L., Friščić, T., Schurko, R. W., *Chem. Mater.* **2020,** *32* (10), 4273-4281. DOI 10.1021/acs.chemmater.0c00894.

33. Budny-Godlewski, K., Justyniak, I., Leszczyński, M. K., Lewiński, J., *Chem. Sci.* **2019,** *10* (30), 7149-7155. DOI 10.1039/c9sc01396b.

34. Budny-Godlewski, K., Leszczyński, M. K., Tulewicz, A., Justyniak, I., Pinkowicz, D., Sieklucka, B., Kruczała, K., Sojka, Z., Lewiński, J., *ChemSusChem* **2021,** *14* (18), 3887-3894. DOI 10.1002/cssc.202101269.

35. Li, S., Huskić, I., Novendra, N., Titi, H. M., Navrotsky, A., Friščić, T., *ACS Omega* **2019,** *4* (3), 5486-5495. DOI 10.1021/acsomega.9b00295.

36. Bekri-Abbes, I., Srasra, E., *Mater. Sci. Semicond. Process.* **2015,** *40*, 543-549. DOI 10.1016/j.mssp.2015.07.014.

37. Malca, M. Y., Bao, H., Bastaille, T., Saadé, N. K., Kinsella, J. M., Friščić, T., Moores, A., *Chem. Mater.* **2017,** *29* (18), 7766-7773. DOI 10.1021/acs.chemmater.7b02134.

38. Ali, S. S. M., Eisa, W. H., Abouelsayed, A., *Composites, Part B* **2019,** *176*. DOI 10.1016/j.compositesb.2019.107289.

39. Turkevich, J., Stevenson, P. C., Hillier, J., *Discuss. Faraday Soc.* **1951,** *11*. DOI 10.1039/df9511100055.

40. P.-M. Adam, S. Benrezzak, J. L. Bijeon and P. Royer, *J. Appl. Phys.*, **2000**, *88*, 6919-6921.

41. Peters, S., Peredkov, S., Neeb, M., Eberhardt, W., Al-Hada, M., *Surf. Sci.* **2013,** *608*, 129-134. DOI 10.1016/j.susc.2012.09.024.

42. Sankar, M., He, Q., Morad, M., Pritchard, J., Freakley, S. J., Edwards, J. K., Taylor, S. H., Morgan, D. J., Carley, A. F., Knight, D. W., Kiely, C. J., Hutchings, G. J., *ACS Nano* **2012,** *6* (8), 6600-13. DOI 10.1021/nn302299e.

43. Radnik, J., Mohr, C., Claus, P., *Phys. Chem. Chem. Phys.* **2003,** *5* (1), 172-177. DOI 10.1039/b207290d.

44. Haiss, W., Thanh, N. T., Aveyard, J., Fernig, D. G., *Anal. Chem.* **2007,** *79* (11), 4215-21. DOI 10.1021/ac0702084.

45. Ankri, R., Fixler, D., *Nanophotonics* **2017,** *6* (5), 1031-1042. DOI 10.1515/nanoph-2017-0033.

46. Liu, S., Xu, Y. J., *Sci. Rep.* **2016,** *6*, 22742. DOI 10.1038/srep22742.

47. Jana, N. R., Gearheart, L., Murphy, C. J., *Langmuir* **2001,** *17* (22), 6782-6786. DOI 10.1021/la0104323.

48. Link, S., El-Sayed, M. A., *J. Phys. Chem. B* **1999,** *103* (40), 8410-8426. DOI 10.1021/jp9917648.

49. Shimizu, T., Teranishi, T., Hasegawa, S., Miyake, M., *J. Phys. Chem. B* **2003,** *107* (12), 2719-2724. DOI 10.1021/jp026920g.

50. Davey, W. P., *Phys. Rev.* **1925,** *25* (6), 753-761. DOI 10.1103/PhysRev.25.753.

51. Kim, F., Connor, S., Song, H., Kuykendall, T., Yang, P., *Angew. Chem., Int. Ed.* **2004,** *43* (28), 3673-7. DOI 10.1002/anie.200454216.

52. Whitehead, C. B., Özkar, S., Finke, R. G., *Chem. Mater.* **2019,** *31* (18), 7116-7132. DOI 10.1021/acs.chemmater.9b01273.

53. Hutchings, B. P., Crawford, D. E., Gao, L., Hu, P., James, S. L., *Angew. Chem. Int. Ed.* **2017,** *56* (48), 15252-15256. DOI 10.1002/anie.201706723.

54. M. Wojdyr, *J. Appl. Cryst.,* **2010**, *43* (5), 1126-1128. DOI 10.1107/s0021889810030499

55. Davey, W. P., *Phys. Rev.* **1925,** *25* (6), 753-761. DOI 10.1103/PhysRev.25.753.

56. S. Abrahams and J. Bernstein, *Acta Cryst.,* **1965**, *18* (5), 926-932. DOI 10.1107/s0365110x65002244

57. A. Fischer and G. Palladino, *Acta Crystallogr., Sect. E: Struct. Rep. Online*, **2003**, *59* (11), m1080-m1082. DOI 10.1107/s1600536803024395

## 2.7    Supplemental Information

### 2.7.1   Analytical Methods

**X-ray photoelectron spectroscopy (XPS)**

XPS was used to track the chemical transformation of Au(III) precursor to Au(0) product in the solid state. Milled powders were evenly spread over single-sided adhesive Cu tape and mounted onto the sample block. Powders aged at elevated or lowered temperatures quickly equilibrated to room temperature on the sample block, assuring a consistent scanning temperature. Samples were analyzed on a Fischer Scientific Kα X-Ray spectrometer with an excitation source of Al Kα = 1486.6 eV. The spot size was 400 μm, running three survey scans at 200 mV with 50 ms residence times, five high-resolution scans for C, and 10 high-resolution scans for other specific elements, also at residence times of 50 ms. Au scans were always the first to be performed as Au(III) is known to photoreduce during XPS analysis, likely caused by the low energy electrons emitted by the flood gun for charge balancing. Data was processed using the Avantage software. Binding energies were charge corrected by referencing to the C 1s binding energy at 284.8 eV. Peak position and deconvolution were also performed. Deconvoluted peak profiles were integrated and subsequently plotted using a custom-built Python3 script to reveal the percentage reduction of the gold salt.

**Diffuse reflectance spectroscopy (DRS)**

Milled powders were placed into clean and dry 10 mm wide quartz cuvettes for DRS analysis. Samples were analysed using a Perkin Elmer Lambda 750 UV/Vis/NIR spectrophotometer equipped with tungsten-halogen and deuterium light sources, a double holographic grating monochromator, a high sensitivity R928 photomultiplier for UV/Vis and a Peltier cooled PbS detector for NIR. Diffuse reflectance measurements from 850 to 350 nm, in 1 nm increments at a scan speed of 266.75 nm/min, were done through the Scan Lambda 750 software program. $BaSO_4$ white powder was used in place of a

Spectralon standard as a highly reflective solid upon which a 100% reflection (0 Absorbance) correction was performed. The instrument then measured the percent diffuse reflectance of the sample relative to the standard and calculated an absorbance value through a logarithmic transformation of the percent reflectance. Absorbance data was exported through the UV WinLab software and then normalized and plotted using Python3. In all cases triplicate 'b' is presented in the main text.

**Powder X-ray diffraction (PXRD)**

PXRD studies were performed using a Bruker D8 Advance diffractometer equipped with a Ni-filtered CuKα (λ = 1.5418 Å) source, 1D LYNXEYE detector, and operating at 40kV and 40 mA. Individual PXRD patterns were obtained over a $2\theta$ range of 3° to 90° in increments of 0.02° with an exposure time of 0.75 s. The neat powders were spread evenly over a silicon wafer of a low-zero background sample holder. In all cases triplicate 'b' is presented in the main text.

*In situ* aging studies were performed by fitting an Anton Paar CHC$^+$ chamber to the diffractometer, where the sample area was filled, and levelled, with freshly milled powder. For constant temperature studies diffractograms were collected over a $2\theta$ range of 5° to 50° in increments of 0.02° with an exposure time of 0.8 s in a stepwise fashion. In total 120 diffractograms were obtained for each temperature (30, 35, and 40 °C).

For the variable temperature study diffractograms were collected $2\theta$ range of 32.5° to 42.5° in increments of 0.02° with an exposure time of 2.8 s in a stepwise fashion. The initial temperature was set equal to 24 °C and was increased by 2 °C after every five consecutive measurements. The study was complete after the fifth measurement at 46 °C.

**Transmission electron microscopy (TEM)**

The TEM and scanning transmission electron microscopy (STEM) studies were performed using a Thermo Scientific Talos F200X transmission electron microscope equipped with a high-brightness XFEG Schottky source, operated at 200 keV.

TEM grids were prepared using the drop-cast method whereby a 7.5 μL of a 1.0 mg mL$^{-1}$ solution of the milled powder in toluene was drop-cast onto a 400 mesh Cu grid allowed

to dry. Images were captured in the bright field mode. Individual particles were sized using the ImageJ software in populations of N ≥ 600 and the resulting size distribution analysis was performed using Microsoft Excel. The resulting population profiles from the number distributions were fitted to Gaussian functions in the Fityk program[54] and plotted using Python3. Uncertainties in the form of standard deviations were pulled from the fitted Gaussian functions made by Fityk.

STEM sample grids were prepared in the solid-state. A 200 mesh Cu grid with a 15 nm thick SiOx substrate coating was impregnated with the milled powder by introducing the grid into the sample and agitating the recipient. Once impregnated, pressurized air was used to remove excess sample from the grid. The sample was analyzed using STEM coupled with the high-angle annular dark field (HAADF) detector.

The energy dispersive X-ray spectroscopy (EDXS) analyses were performed using a SDD Super-X detector at 200 keV. The total acquisition time was 15 min per sample using drift correction to compensate the shift after each scan.

### 2.7.2  Results and discussion

#### a.  Visual Inspection

The colors of the powders shown in Figure 2.7 exhibit some variation to those observed in real life, caused by differences in lighting and by the automatic brightness and contrast adjustments performed by the camera. This is particularly true for samples aged at 32 °C where the samples darkened consistently after seven days of aging to appear dark purple/black after 43 days.

**Figure 2.7** Macroscopic photos showing the changing color of the milled powders over the aging period. Powders were aged at a) -18 °C, b) 21 °C, and c) 32 °C.

### b. X-ray photoelectron spectroscopy

**Investigating the photoreduction of HAuCl$_4$·3H$_2$O**

The propensity of Au(III) salts to undergo photoreduction during XPS analysis increases the difficulty in tracking the reaction using the technique. To better understand the process analyses were performed on HAuCl$_4$·3H$_2$O as received from the supplier. Granules of the solid reactant were pressed onto the adhesive Cu tape with a flat PTFE coated spatula, to avoid galvanic reduction. Two spots of the sample were selected for analysis. On the first, five scans of Au were performed, (Figure 2.8a), which was then repeated to give a total of ten scans, (Figure 2.8b). On the second, ten scans of Au were performed in a single step, (Figure 2.8c). The reduction of Au(III) to Au(0) is clear in each of the three analyses. After five scans (a), the gold salts has been reduced by 14 %, given by the area of the purple and blue peaks which represent the Au(0) doublet. After the second five scans (b) the gold salt was further reduced, for a total of 20 %. When ten scans were performed sequentially (c) the same amount of reduction was observed, 20 %. Given the high levels of reduction observed after just five scans, 14 %, which is increased by just 6 % after the further five scans, we believe that the reduction depends on the amount of

time the sample is being measured rather than the number of scans. Given that the ten-scan run gives the same amount of reduction, we suspect that the low energy electron emitting flood gun, used for charge correction in the sample, is responsible for the observed reduction.
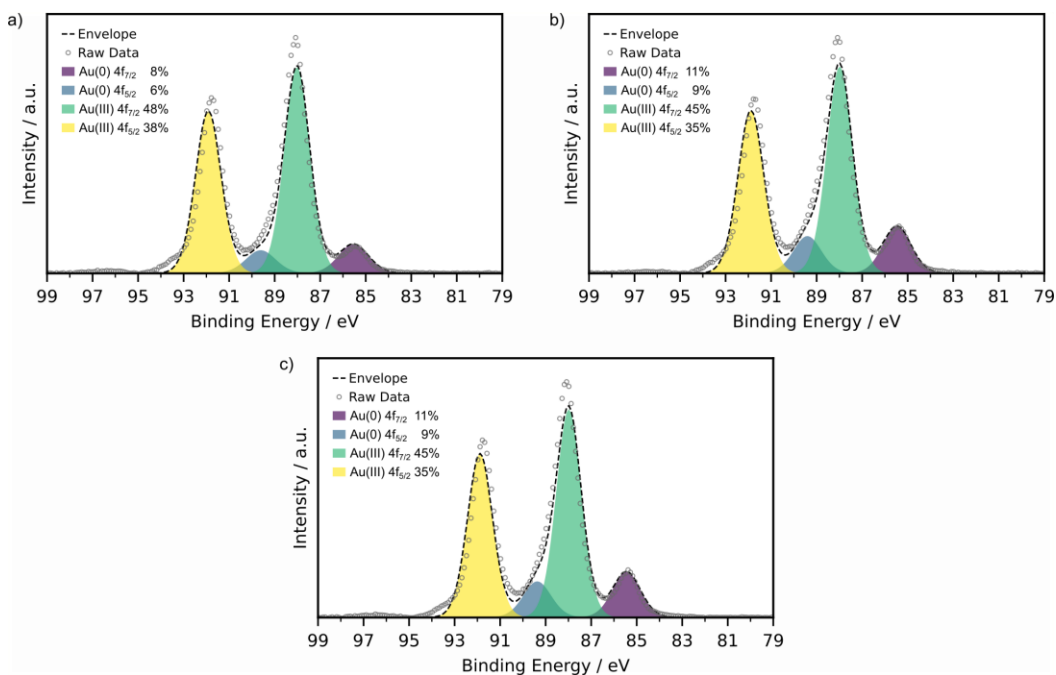


**Figure 2.8** Normalized deconvolutions of the XPS spectra for HAuCl₄·3H₂O after a) five scans, b) a further five scans of the same spot, and c) ten scans of another region. Purple and blue peaks represent the Au(0) 4f$_{7/2}$ and 4f$_{5/2}$ signals, respectively, while green and yellow peaks represent the Au(III) 4f$_{7/2}$ and 4f$_{5/2}$ signals, respectively.

Attempts were made to perform the analyses with the flood gun turned off in an effort to avoid the photoreduction of the gold salt. Three spots were analyzed for a sample of freshly milled powder, Figure 2.9. If it evident that turning off the flood gun had adverse effects on the obtained data. Peaks were shifted considerably and inconsistently which also resulted in a great deal of peak broadening. The combination of these effected rendered the charge correction and deconvolution of the raw peaks into the Au(0) and Au(III) doublets impossible.
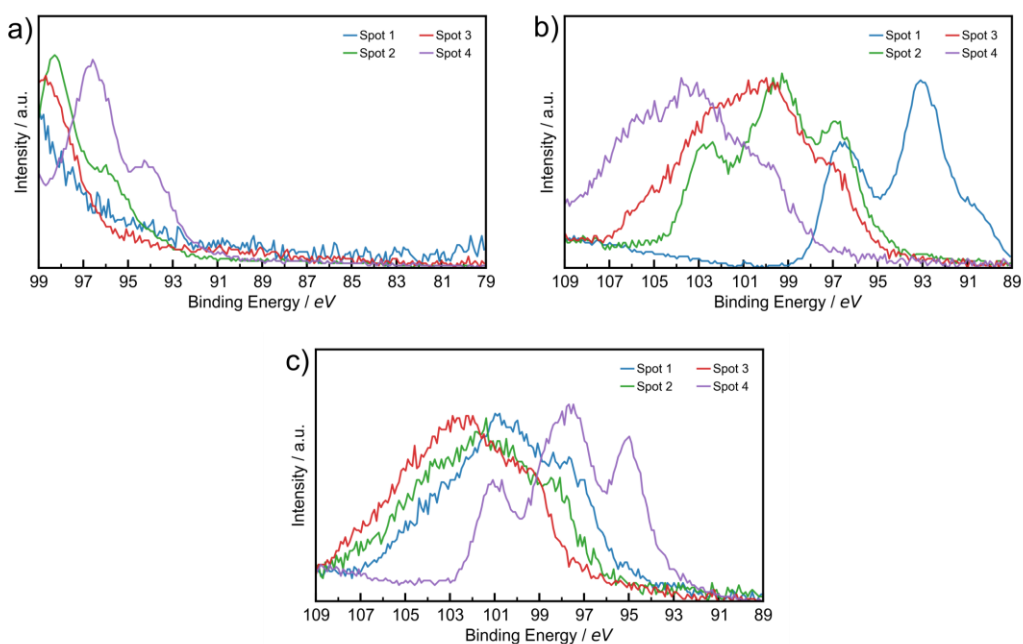
**Figure 2.9** XPS results of a standard day 0 milled powder with the low energy electron emitting flood gun turned off. Plots a), b), and c) represent three individual samples of the milled powder.

## XPS monitoring of samples during the six-week aging period
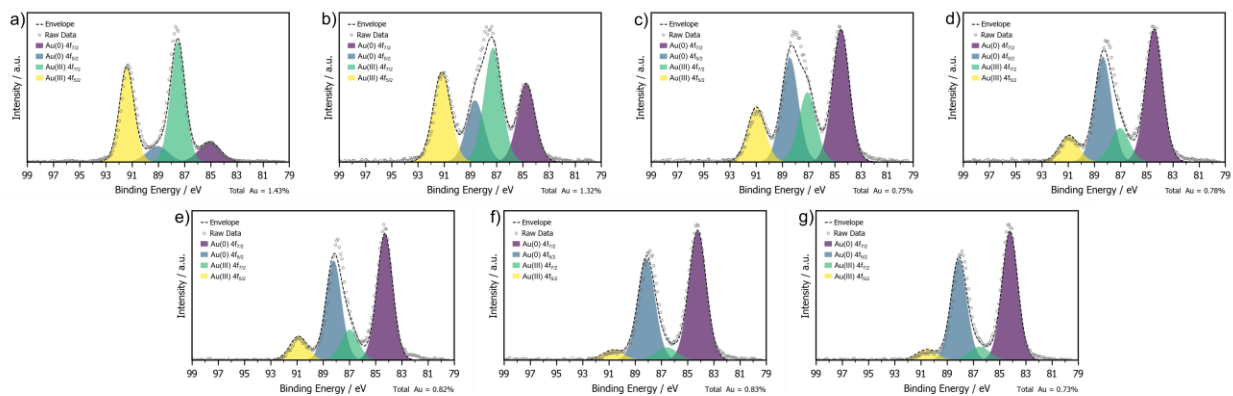


**Figure 2.10** Normalized deconvolutions of the XPS data for milled powder aged at 21 °C. The purple and blue peaks represent the Au(0) $4f_{7/2}$ and $4f_{5/2}$ signals, respectively. The green and yellow peaks represent the Au(III) $4f_{7/2}$ and $4f_{5/2}$ signals, respectively. Plots correspond to aging times of a) 0 days, b) 1 day, c) 4 days, d) 7 days, e) 15 days, f) 22 days, and g) 43 days.
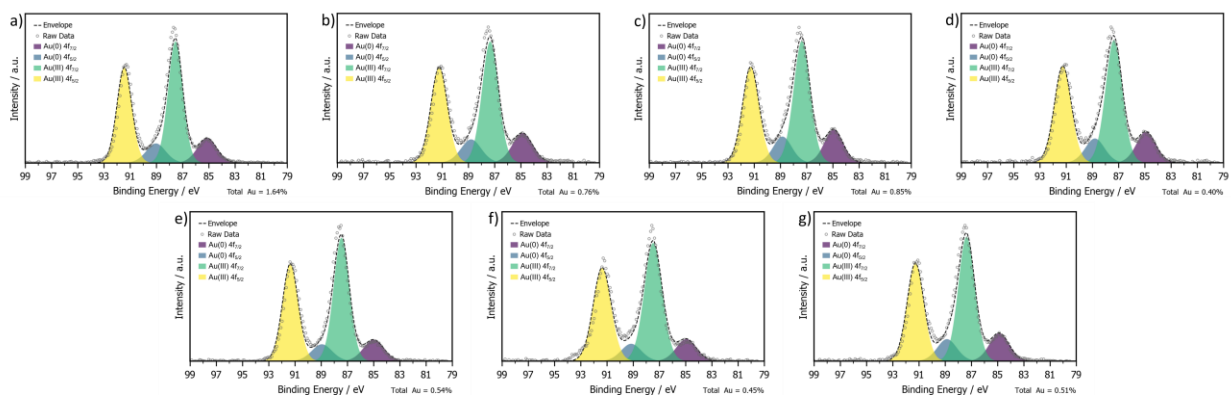
**Figure 2.11** Normalized deconvolutions of the XPS data for milled powder aged at -18 °C. The purple and blue peaks represent the Au(0) 4f$_{7/2}$ and 4f$_{5/2}$ signals, respectively. The green and yellow peaks represent the Au(III) 4f$_{7/2}$ and 4f$_{5/2}$ signals, respectively. Plots correspond to aging times of a) 0 days, b) 1 day, c) 4 days, d) 7 days, e) 15 days, f) 22 days, and g) 43 days.
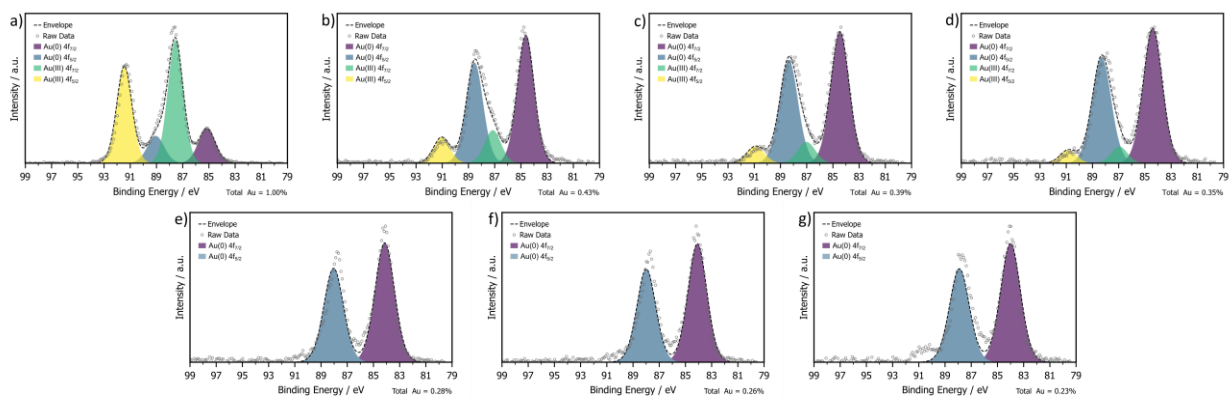


**Figure 2.12** Normalized deconvolutions of the XPS data for milled powder aged at 32 °C. In plots a-d, the purple and blue peaks represent the Au(0) 4f$_{7/2}$ and 4f$_{5/2}$ signals and the green and yellow peaks represent the Au(III) 4f$_{7/2}$ and 4f$_{5/2}$ signals, respectively. In plots e-g, the best fitting was found without any Au(III) peak. Plots correspond to aging times of a) 0 days, b) 1 day, c) 4 days, d) 7 days, e) 15 days, f) 22 days, and g) 43 days.

## c. Diffuse reflectance spectroscopy
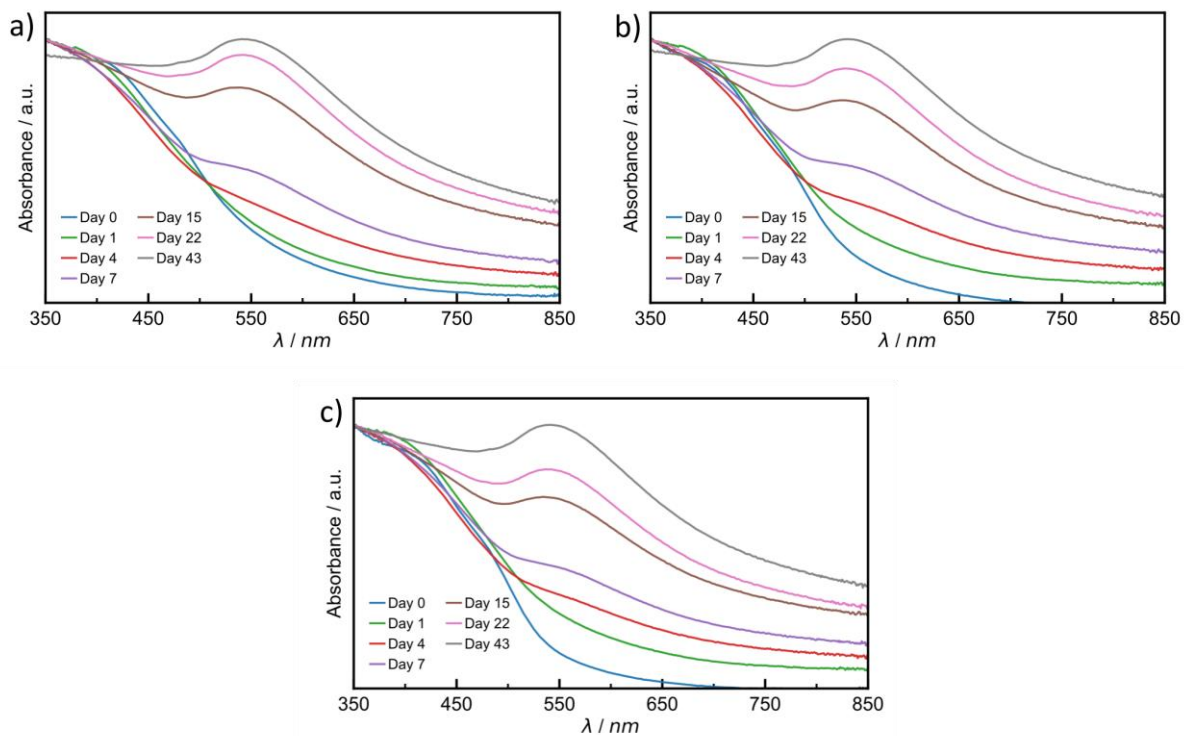


**Figure 2.13** DRS plots for triplicates a, b, and c aged at 21 °C. Samples were analyzed after 0 (blue), 1 (green), 4 (red), 7 (violet), 15 (brown), 22 (pink), and 43 (grey) days of aging.
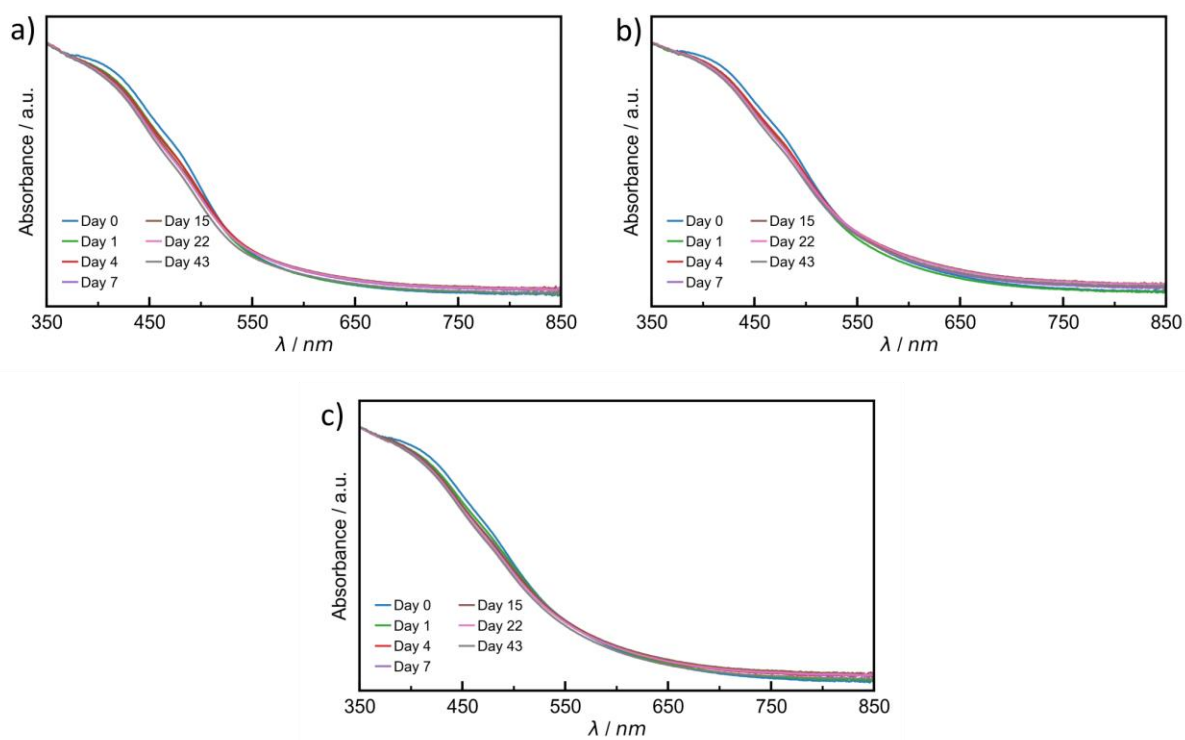
**Figure 2.14** DRS plots for triplicates a, b, and c aged at -18 °C. Samples were analyzed after 0 (blue), 1 (green), 4 (red), 7 (violet), 15 (brown), 22 (pink), and 43 (grey) days of aging.
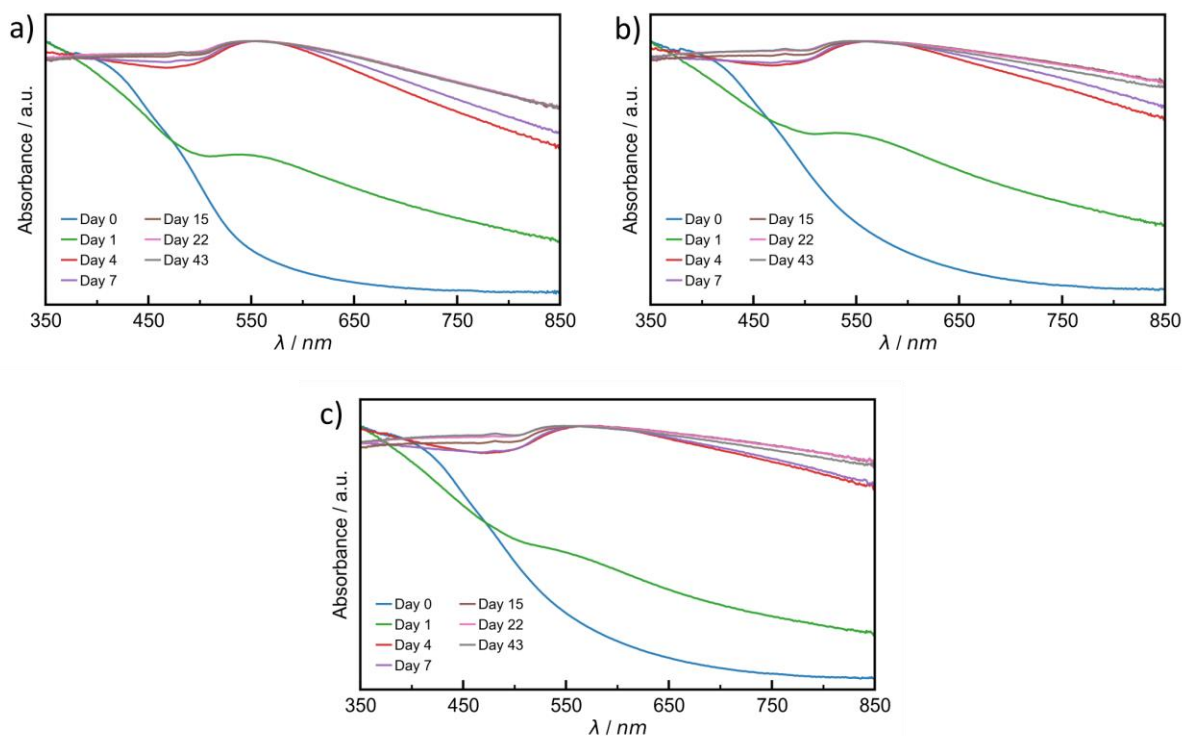
**Figure 2.15** DRS plots for triplicates a, b, and c aged at 32 °C. Samples were analyzed after 0 (blue), 1 (green), 4 (red), 7 (violet), 15 (brown), 22 (pink), and 43 (grey) days of aging.

The absorption activity between the wavelengths of 750 nm to 350 nm is overwhelmingly due to the Au(III) and Au(0) species and does not originate from other materials, precursor or by-product, in the solid (Figure 2.16).
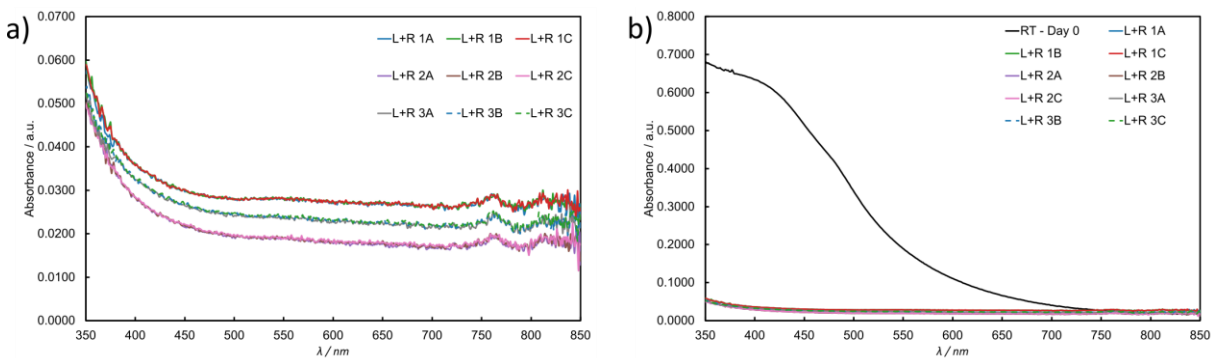


**Figure 2.16** a) DRS raw data plot of a 5:1.1 molar mixture of octadecylamine (L = ligand) and trisodium citrate dihydrate (R = reductant). b) The same plot nominally compared to a standard day 0 absorbance curve of the milled powder with the gold-salt.

The DRS study showed gradual increase in absorbance observed for samples aged at 21 °C. Plotting the normalized absorbance values at 541 nm, the position of maximum absorbance reveals a sigmoidal relationship. As the data does not begin at exactly zero, a logistic function (Equation 2.1) was fitted to the data using Fityk.

$$S(x) = \frac{L}{1 + exp^{-k(x-x_0)}} + b \qquad \textbf{Equation 2.1}$$

Where L scales the function to the range of the input absorbance data, $k$ indicates the steepness of the curve, $x_0$ is the midpoint of the sigmoid in $x$, and $b$ accounts for the offset in the absorbance data which is not initially 0 for freshly milled powder.

The resulting logistic function was found to be,

$$S(x) = \frac{0.8822}{1 + exp^{-0.16244(x-9.048)}} + 0.1213 \qquad \textbf{Equation 2.2}$$

With an $r^2$ value of 0.992 for the fitting.

Data points between 0 and 15 days of aging showed a linear trend, these were fitting to a straight line in Fityk. The gradient of the resulting straight line gave a rate of growth of $k = 3.68x10^{-7}$ s$^{-1}$. In this case, $r^2 = 0.983$.

## d. Powder X-ray diffraction
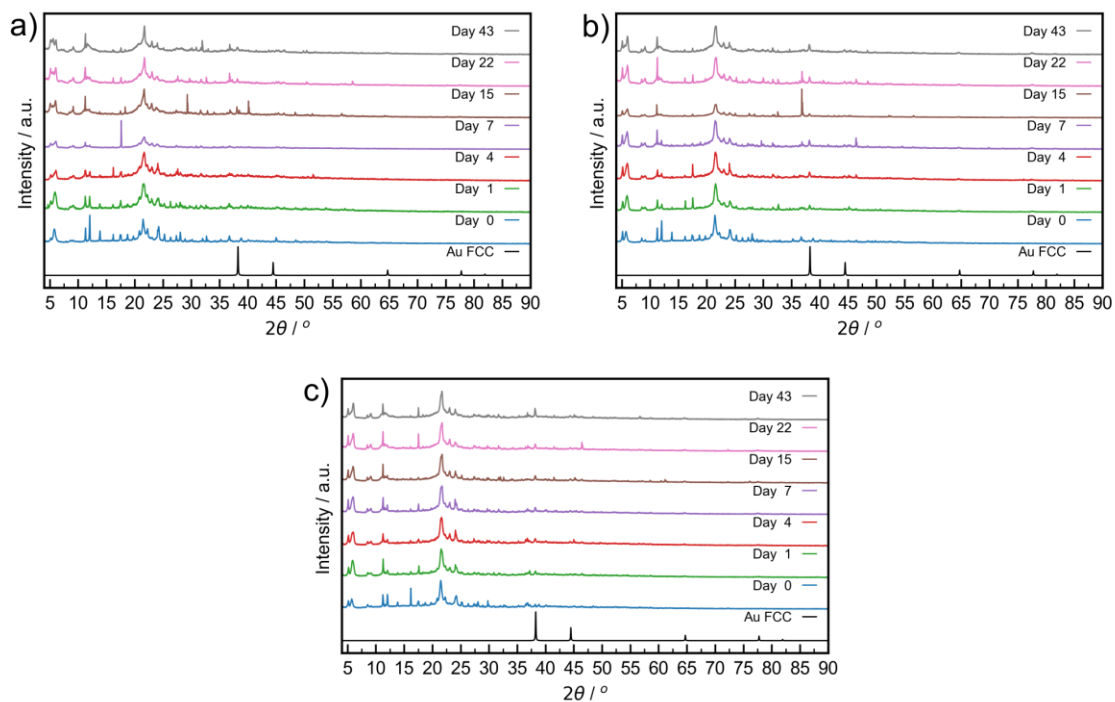


**Figure 2.17** PXRD plots for triplicates a, b, and c at 21 °C. Samples were analyzed after 0 (blue), 1 (green), 4 (red), 7 (violet), 15 (brown), 22 (pink), and 43 (grey) days of aging. The simulated pattern for elemental gold in the FCC lattice[55] is plotted in black.
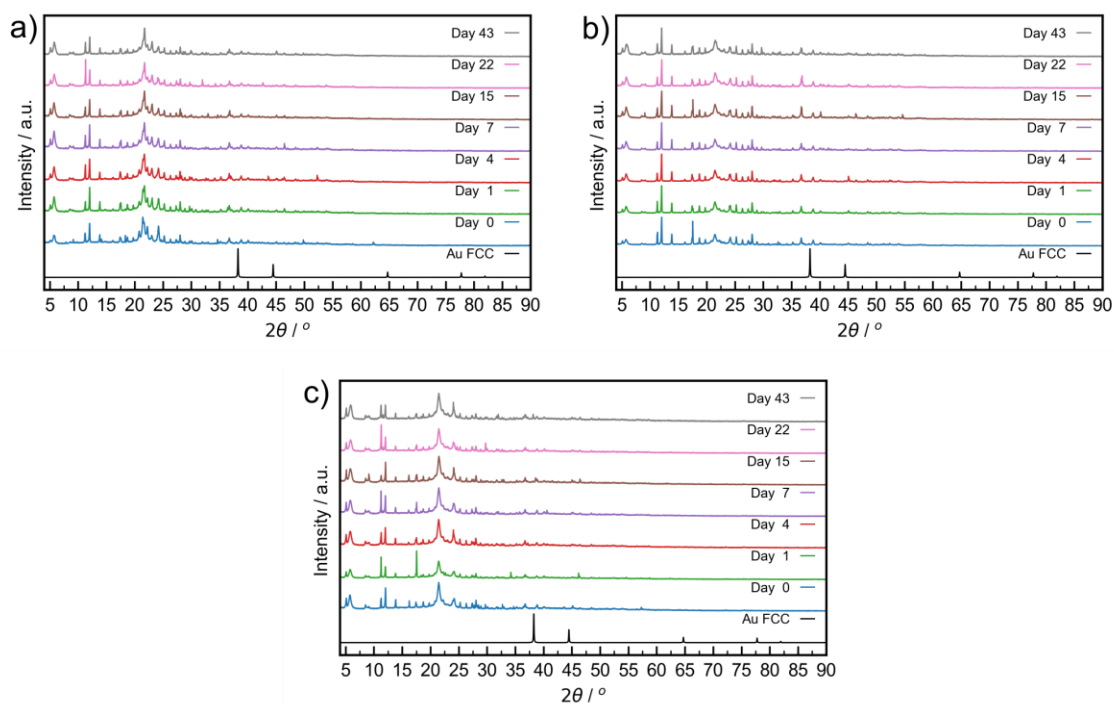
**Figure 2.18** PXRD plots for triplicates a, b, and c aged at -18 °C. Samples were analyzed after 0 (blue), 1 (green), 4 (red), 7 (violet), 15 (brown), 22 (pink), and 43 (grey) days of aging. The simulated pattern for elemental gold in the FCC lattice[55] is plotted in black.
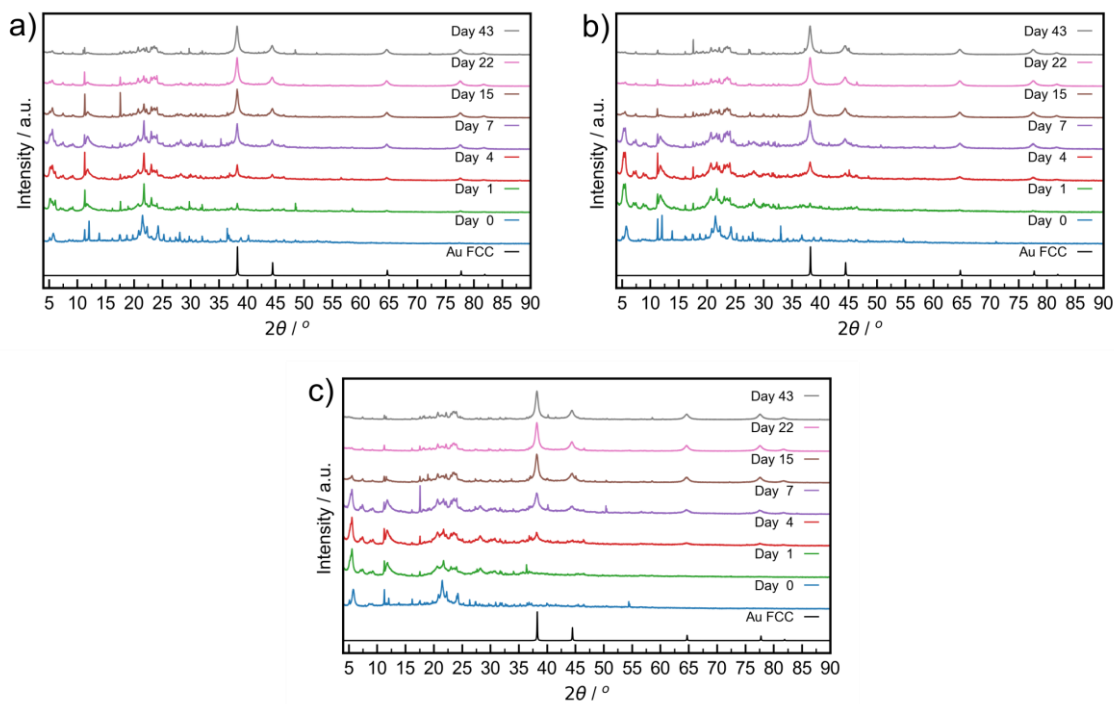


**Figure 2.19** PXRD plots for triplicates a, b, and c aged at 32 °C. Samples were analyzed after 0 (blue), 1 (green), 4 (red), 7 (violet), 15 (brown), 22 (pink), and 43 (grey) days of aging. The simulated pattern for elemental gold in the FCC lattice[55] is plotted in black.
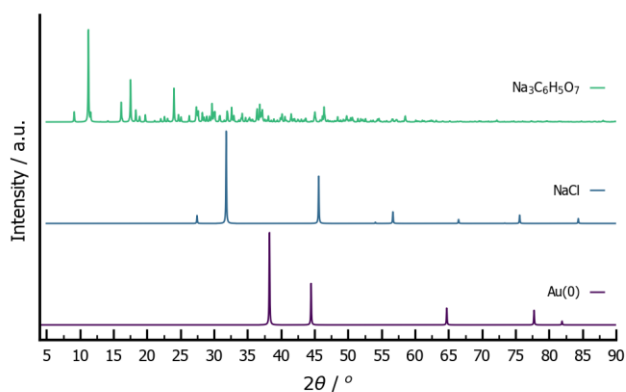
**Figure 2.20** Simulated PXRD patterns of elemental gold in the FCC lattice (purple),[55] NaCl (blue),[56] and trisodium citrate dihydrate (green).[57]

## e. Transmission electron microscopy
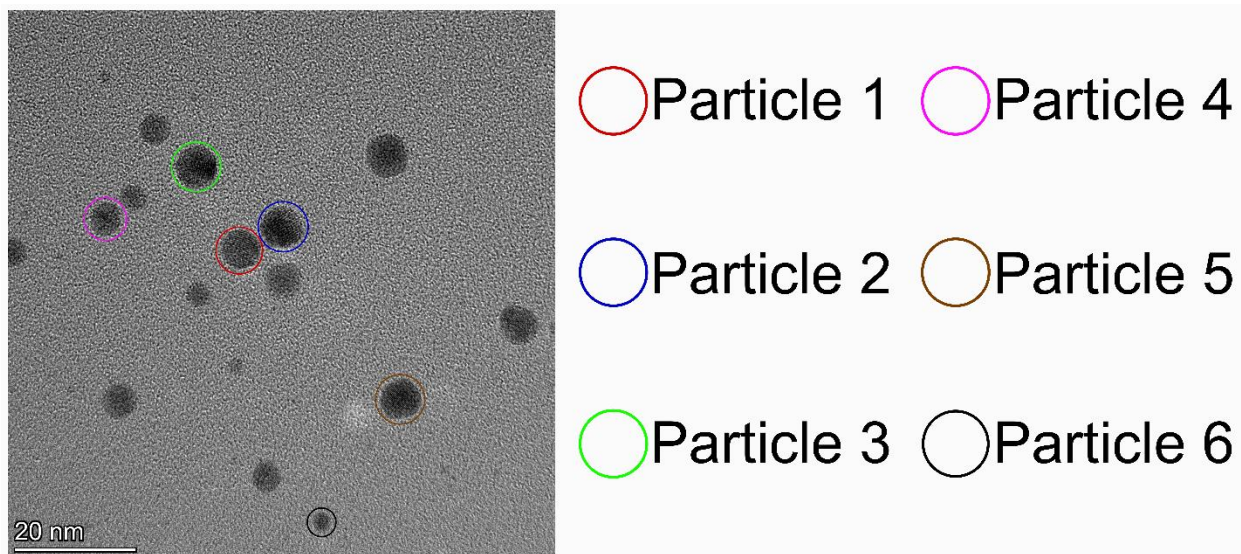


**Figure 2.21** High resolution TEM micrograph of AuNPs with a spherical morphology. Particles with good diffraction have been picked out, circled, and have had their lattice fringes measured. All particle were found to be in good agreement with the (111) d-spacing of FCC Au(0).
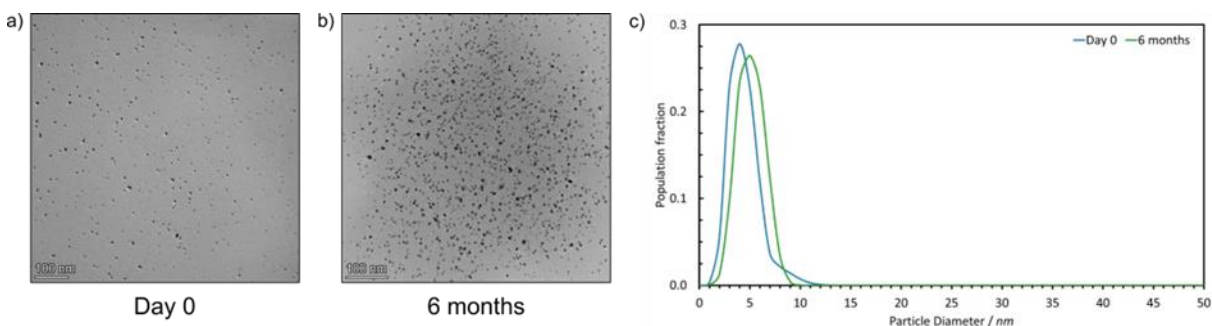
**Figure 2.22** TEM drop-cast images (a, b) and population sizing (c) of nanoparticles produced via a solution control test. Tetrachloroauric acid trihydrate, octadecylamine, and trisodium citrate dihydrate (1:5:1.1 molar ratios) were added to 100 mL of toluene at a solid-to-liquid ratio of 1 mg mL$^{-1}$ and stirred at 400 rpm for 2 minutes at room temperature (21 °C), simulating the drop-casting process. On day 0 (blue), nanoparticles averaged 4.05 ± 1.66 nm in diameter. After 6 months of aging (green), nanoparticles averaged 4.71 ± 1.34 nm.
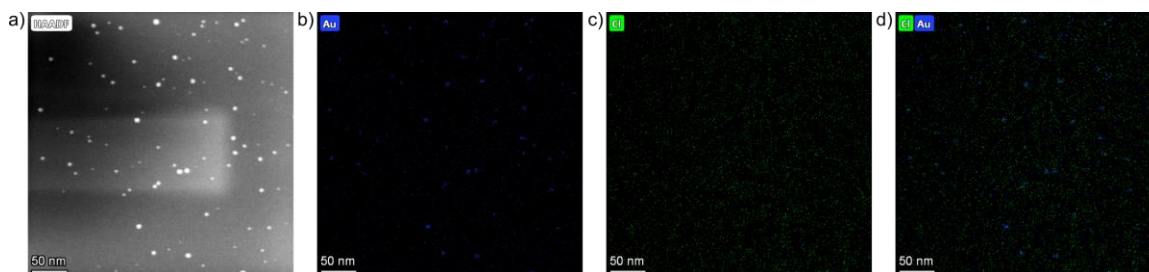


**Figure 2.23** STEM-HAADF images and EDXS elemental maps for Au, Cl, and Au combined with Cl (left to right, respectively) for the solution control sample where the three reactants were stirred in toluene for 120 s before drop casting.
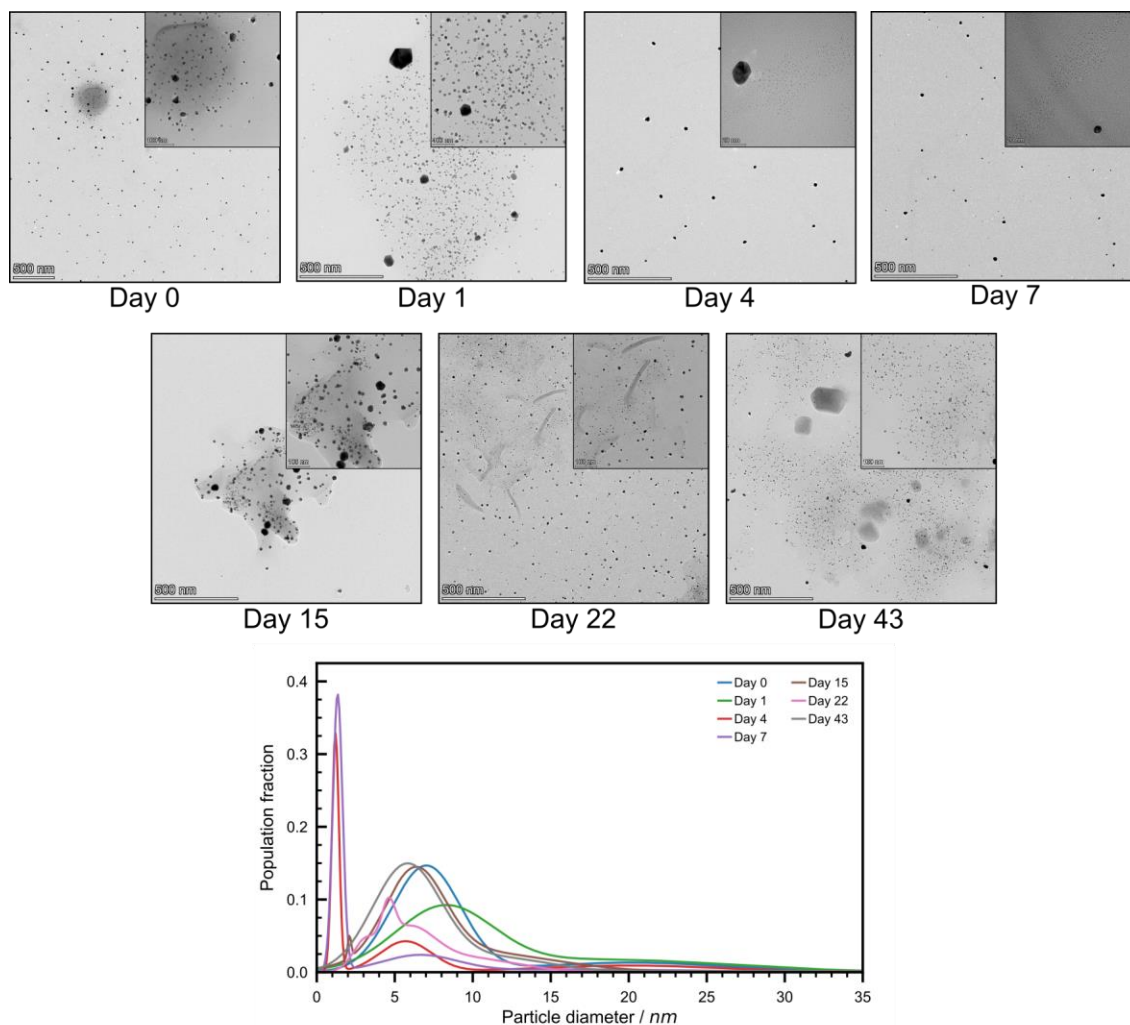
**Figure 2.24** TEM results of room temperature aged milled powder. Representative TEM images and the population distribution profile of sized particles are shown for each day. Samples were analyzed after 0 (blue), 1 (green), 4 (red), 7 (violet), 15 (brown), 22 (pink), and 43 (grey) days of aging.

**Table 2.1** Drop cast TEM peak table for nanoparticle distributions aged at 21 °C.

| | Diameter (nm) | | | | | | |
|---|---|---|---|---|---|---|---|
| Peak[a] | Day 0 | Day 1 | Day 4 | Day 7 | Day 15 | Day 22 | Day 43 |
| 1 | 7.0 ± 1.9 | 8.2 ± 2.6 | 1.2 ± 0.2 | 1.3 ± 0.3 | 2.1 ± 0.1 | 3.0 ± 0.6 | 5.8 ± 1.9 |
| 2 | 20.2 ± 5.1 | 18.3 ± 6.9 | 5.7 ± 1.4 | 6.6 ± 2.1 | 6.3 ± 1.6 | 4.6 ± 0.4 | 11.9 ± 2.6 |
| 3 | - | - | 20.0 ± 5.1 | 17.2 ± 5.8 | 9.7 ± 4.5 | 5.8 ± 1.4 | - |
| 4 | - | - | - | - | - | 9.6 ± 2.7 | - |

[a] Ordered from smallest diameter to largest.
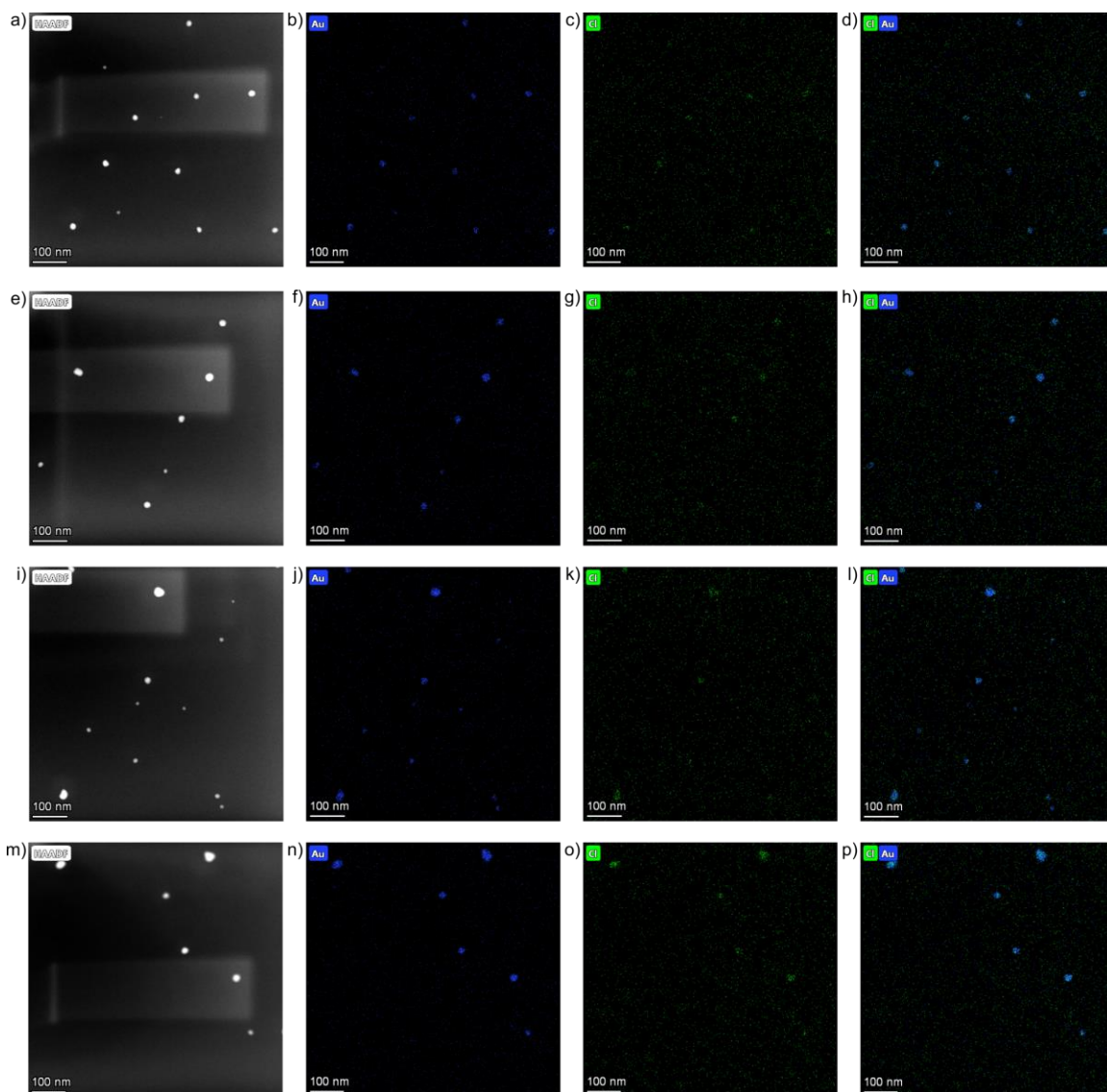
**Figure 2.25** STEM-HAADF images and EDXS elemental maps for Au, Cl, and Au combined with Cl (left to right, respectively) for freshly milled powder (a-d), after one day of aging (e-h), after four days of aging (i-l), and after seven days of aging (m-p).
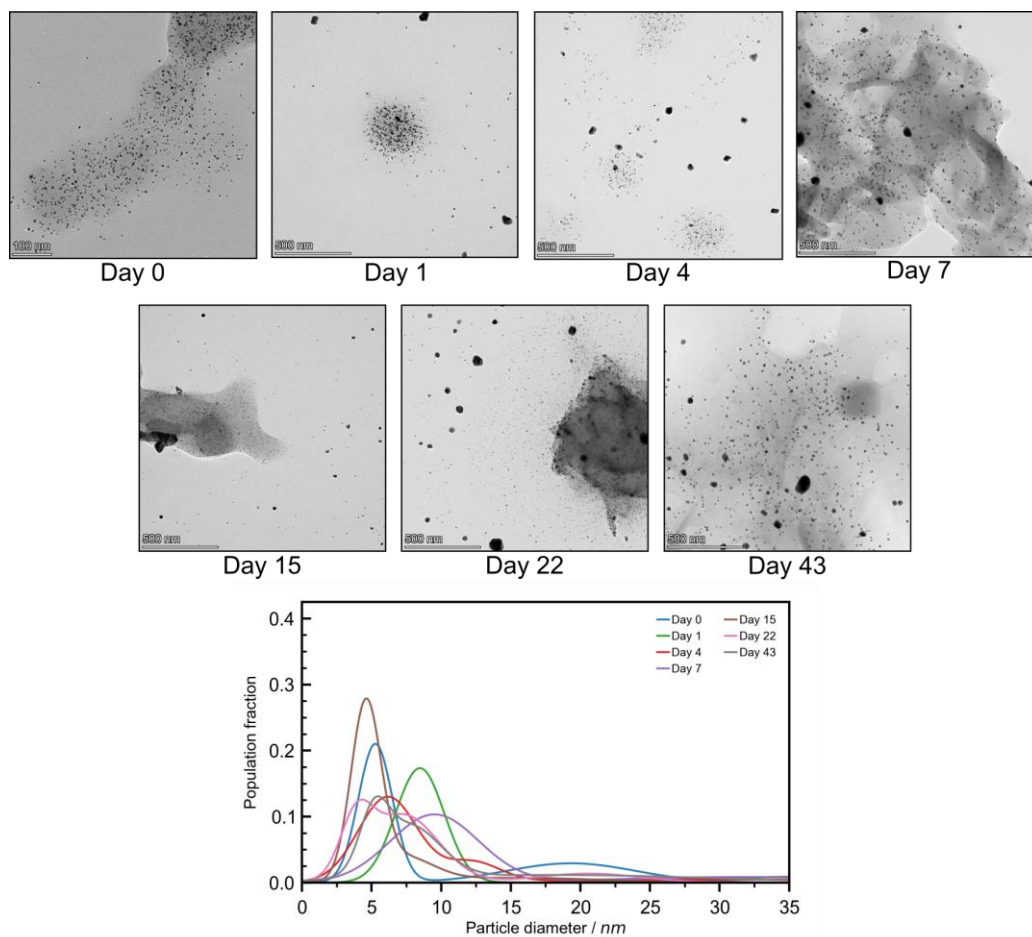
**Figure 2.26** TEM results of low temperature aged milled powder. Representative TEM images and the population distribution profile of sized particles are shown for each day. Samples were analyzed after 0 (blue), 1 (green), 4 (red), 7 (violet), 15 (brown), 22 (pink), and 43 (grey) days of aging.

**Table 2.2** Drop cast TEM peak table for nanoparticle distributions aged at -18 °C.

| Peak[a] | Diameter (nm) | | | | | | |
|---|---|---|---|---|---|---|---|
| | Day 0 | Day 1 | Day 4 | Day 7 | Day 15 | Day 22 | Day 43 |
| 1 | 5.3 ± 1.0 | 8.5 ± 1.5 | 6.2 ± 1.8 | 9.5 ± 2.7 | 4.6 ± 0.9 | 3.9 ± 1.0 | 5.2 ± 0.9 |
| 2 | 19.3 ± 3.9 | 37.8 ± 6.6 | 12.2 ± 1.7 | 31.4 ± 7.7 | 7.2 ± 1.8 | 7.3 ± 2.2 | 7.7 ± 1.9 |
| 3 | - | - | 32.7 ± 13.9 | - | 15.4 ± 5.1 | 20.6 ± 3.2 | 18.2 ± 9.4 |

[a] Ordered from smallest diameter to largest.
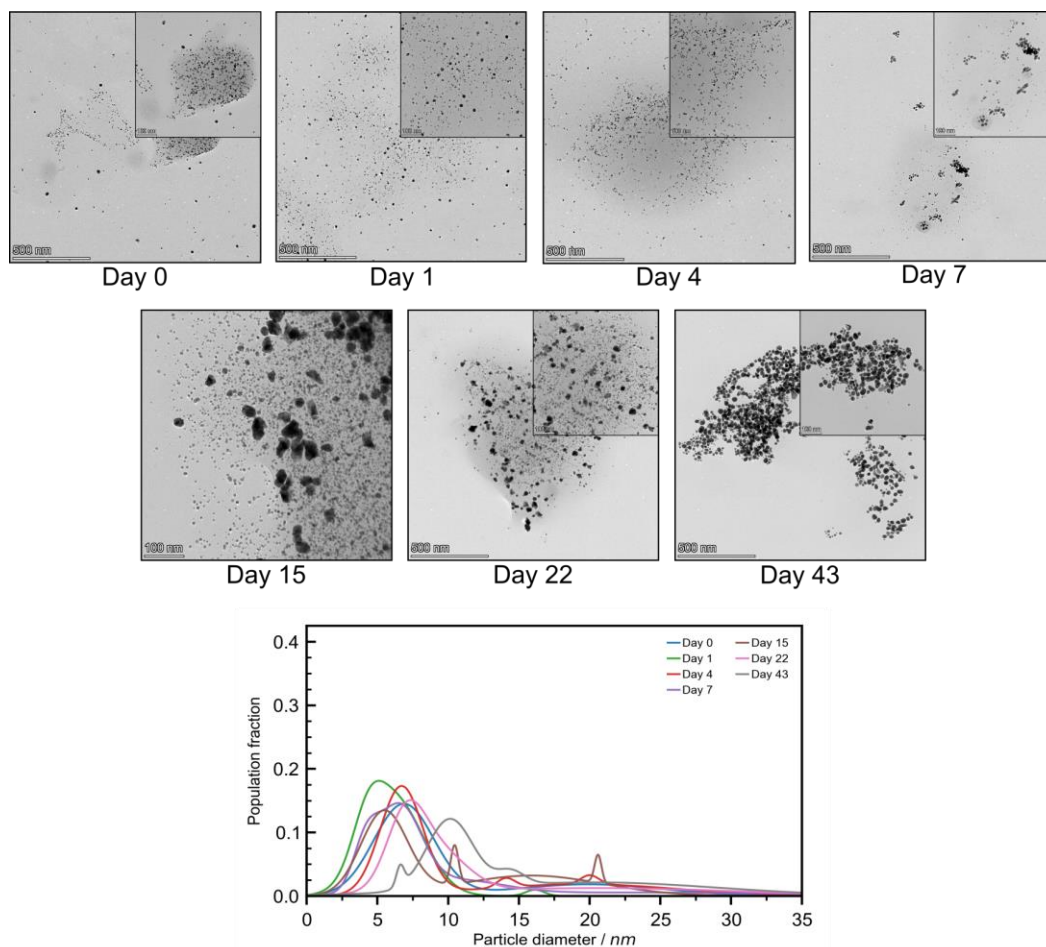
**Figure 2.27** TEM results of elevated temperature aged milled powder. Representative TEM images and the population distribution profile of sized particles are shown for each day. Samples were analyzed after 0 (blue), 1 (green), 4 (red), 7 (violet), 15 (brown), 22 (pink), and 43 (grey) days of aging.

**Table 2.3** Drop cast TEM peak table for nanoparticle distributions aged at 32 °C.

<div align="center">Diameter (nm)</div>

| Peak[a] | Day 0 | Day 1 | Day 4 | Day 7 | Day 15 | Day 22 | Day 43 |
|---------|-------|-------|-------|-------|--------|--------|--------|
| 1 | 6.9 ± 1.8 | 4.3 ± 0.9 | 6.7 ± 1.3 | 4.2 ± 0.8 | 5.5 ± 0.7 | 7.0 ± 1.1 | 6.6 ± 0.2 |
| 2 | 19.9 ± 4.4 4 | 6.2 ± 1.8 | 14.1 ± 0.5 | 6.5 ± 1.3 | 10.5 ± 0.2 | 9.1 ± 1.8 | 10.1 ± 1.4 |
| 3 | - | 16.1 ± 0.6 | 19.4 ± 5.8 | 10.6 ± 2.8 | 15.9 ± 4.2 4 | 20.5 ± 8.5 | 14.4 ± 0.8 |
| 4 | - | - | 20.0 ± 0.6 | 23.0 ± 9.8 | 20.6 ± 0.2 | - | 20.9 ± 7.5 |

[a] Ordered from smallest diameter to largest.

### f.  Activation energy of gold nanoparticle formation

## Constant temperature aging
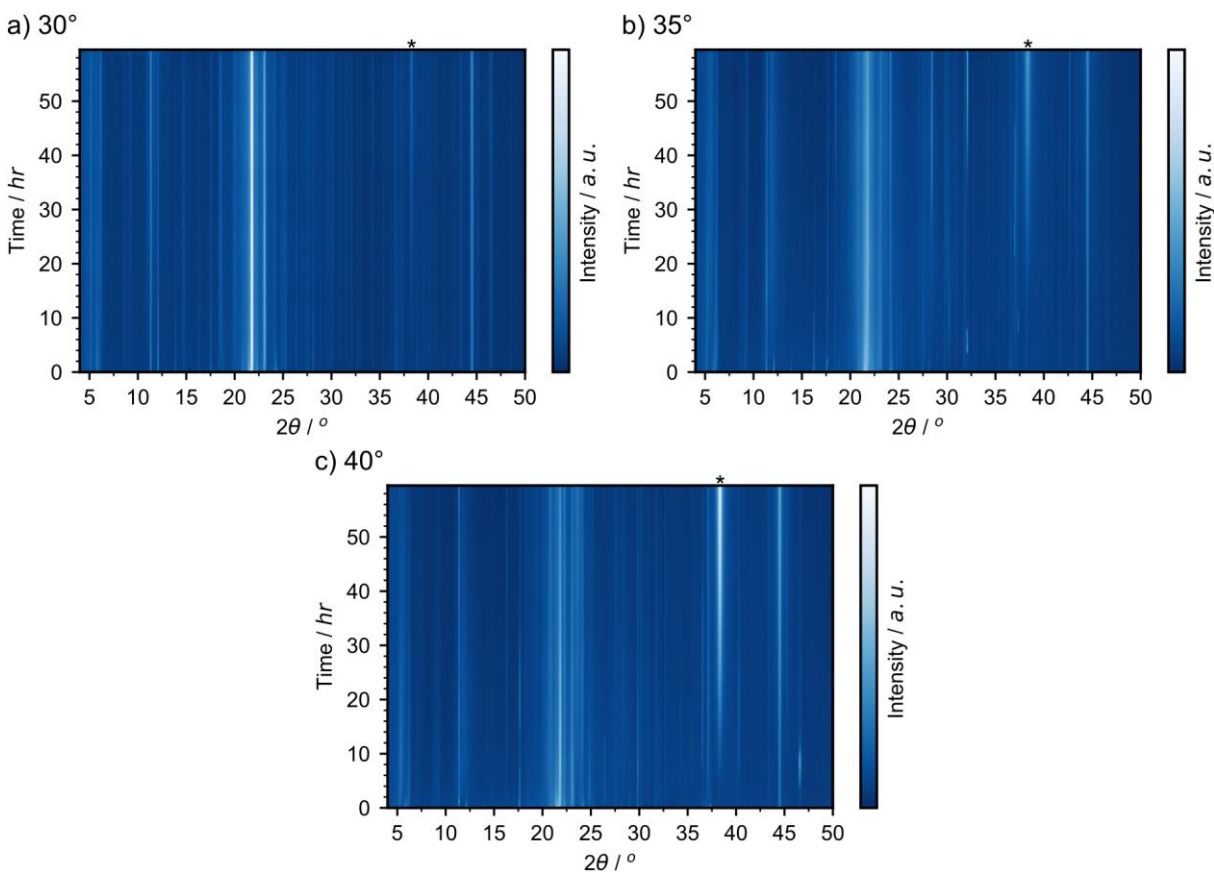


**Figure 2.28** *In situ* constant temperature powder X-ray diffraction analyses of AuNP formation at a) 30 °C, b) 35 °C, and c) 40 °C where * denotes the reflection corresponding to the (111) lattice place of elemental gold.

By integrating the diffractograms between 37.8° and 38.2° *2θ* the increase in intensity with respect to time was obtained, (Figure 2.29a), for each temperature. These were then fitted to a linear trendline, the gradient of which gives the rate of intensity increase for the gold temperature which is directly related to the formation of AuNPs. Plotting the natural logarithms of these rates against the inverse of the aging temperature allows for the activation energy to be obtained from the Arrhenius equation, Equation 2.3.

$$k = A\ exp^{-E_a/RT}$$  **Equation 2.3**

Where $k$ is the rate, A is the pre-exponential factor, $E_a$ the activation energy, $R$ the molar gas constant, and $T$ the temperature. Taking the natural log of both sides of the equation gives Equation 2.4.

$$ln(k) = ln(A) - E_a/RT$$   **Equation 2.4**

Therefore, the gradient of the linear relationship in Figure 2.29b, is equal to $-E_a/R$.
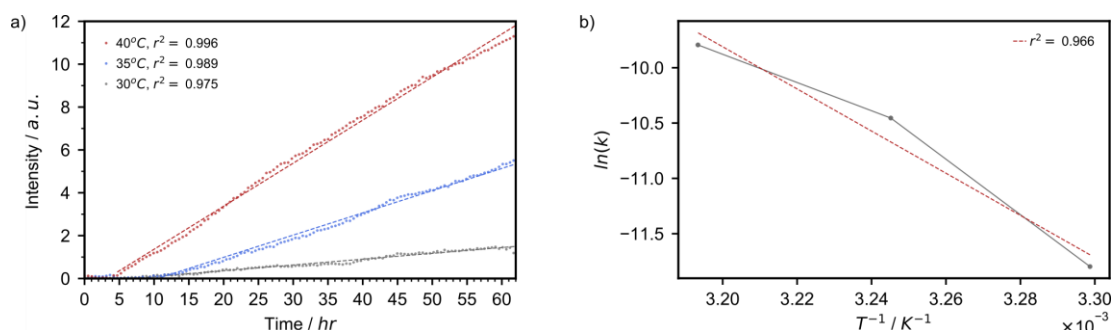


**Figure 2.29** a) Plot of the increase in intensity at 38.2° $2\theta$, i.e. the reflection corresponding to the (111) lattice plane of metallic gold, as a function of time when aged at 30 °C (grey), 35 °C (blue), and 40 °C (red) along with the corresponding linear fits. The linear fitting begins after five hours due to some sampling artefacts in the 35 °C experiment. b) Plot of the natural log of the rate of intensity increase, the gradient of the linear fits in panel (a), against the inverse of the aging temperature.

The activation energy for AuNP growth from the constant temperature PXRD studies was determined to be equal to 158.43 kJmol$^{-1}$.

**Variable temperature aging**

A similar analysis was performed for the variable temperature aging study (Figure 2.30a). Given the linear relationship between the intensity of the reflection at 38.2° $2\theta$ observed in the constant temperature studies, linear fitting was performed for every five scans, leading to 12 individual rates. Each of which corresponding to one of the temperatures studied. Once again, the natural logarithms of these rates were plotted against the inverse of the temperature (Figure 2.30b).
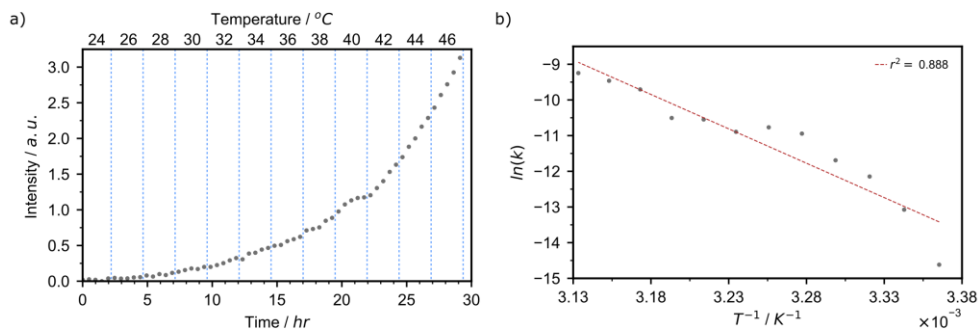
**Figure 2.30** a) Plot of the increase in intensity at 38.2° *2θ*, i.e. the reflection corresponding to the (111) lattice plane of metallic gold, as a function of time during variable temperature aging between 24 °C and 46 °C where the temperature is increased by 2 °C after every five consecutive measurements. b) Plot of the natural log of the rate of intensity increase against the inverse of the aging temperature.

Using the gradient of the linear trend in Figure 2.30b, the activation energy of AuNP growth was determine using Equation 2.4. In this case an activation energy of 160.33 kJmol$^{-1}$ was obtained.

The activation energies are in excellent agreement between the two studies.

$$\Delta E_a = E_a(VT) - E_a(CT) = 1.9 kJmol^{-1}$$

$$\langle E_a \rangle = 0.5[E_a(VT) + E_a(CT)] = 159.38 kJmol^{-1}$$

$$\%Err = 100(\delta/\langle E_a \rangle) = 1.20\%$$

### g. Entropy of activation

Plots of the natural logarithms of these rates against the inverse of the aging temperature for the constant temperature (Figure 2.29b) and variable temperature (Figure 2.30b) PXRD aging studies can also be used to solve the Eyring equation (Equation 2.5) to obtain the entropy of activation.

$$k = \frac{\kappa k_B T}{h} exp^{\frac{\Delta S^{\ddagger}}{R}} exp^{-\frac{\Delta H^{\ddagger}}{RT}}$$  **Equation 2.5**

Where $k$ is the rate constant, $T$ is the temperature, $\Delta H^{\ddagger}$ is the enthalpy of activation, $R$ is the molar gas constant (8.3145 m$^2$ kg s$^{-2}$ K$^{-1}$ mol$^{-1}$),$\kappa$ is the transmission coefficient, $k_B$ is the Boltzmann constant (1.3806 x10$^{-23}$ m$^2$ kg s$^{-2}$ K$^{-1}$), $h$ is Planck's constant (6.6261 x10$^{-}$

[34] m$^2$ kg s$^{-1}$), and $\Delta S^{\ddagger}$ is the entropy of activation. $\kappa$ is assumed to be equal to one as it reflects the probability of the reaction proceeding after reaching the activated state. The Eyring equation can be solved through the line of best fit in Figure 2.29b and Figure 2.30b when rewritten as,

$$ln\left(\frac{k}{T}\right) = \frac{-\Delta H^{\ddagger}}{RT} \cdot \frac{1}{T} + ln\left(\frac{\kappa k_B}{h}\right) + \frac{\Delta S^{\ddagger}}{R}$$ **Equation 2.6**

The *y* intercept (C) of the trend line is given by,

$$C = ln\left(\frac{\kappa k_B}{h}\right) + \frac{\Delta S^{\ddagger}}{R}$$ **Equation 2.7**

$\Delta S^{\ddagger}$ can be obtained as,

$$\Delta S^{\ddagger} = R\left[C - ln\left(\frac{\kappa k_B}{h}\right)\right]$$ **Equation 2.8**

$$\Delta S^{\ddagger} = 8.3145 \cdot (C - 23.7601)$$ **Equation 2.9**

Therefore, the entropy of activation was calculated to be 227.73 J·mol$^{-1}$ K$^{-1}$ and 230.31 J·mol$^{-1}$ K$^{-1}$ for the constant temperature and variable temperature PXRD aging studies, respectively. Thus, the average entropy of activation for the mechanically-activated aging formation of AuNPs is 229.02 J·mol$^{-1}$ K$^{-1}$. The positive entropy of activation confirms that the underlying process is dissociative in nature.

# 3 Direct observation by high resolution transmission electron microscopy of gold (III) particle transformation during aging reduction reaction

This chapter is based upon a published article and is reprinted with permission from the Royal Society of Chemistry. The work in this chapter used the same aging mechanosynthesis reaction as that of the previous chapter, however with a different goal. The previous work established the aging mechanosynthesis of AuNPs as a method to investigate solid-state bottom-up nanoparticle mechanosynthesis in better detail; in this work we sought to learn more about the mechanically activated aging process and the composition and mobility of the reagent species in the solid. This chapter is an extension of the original investigation, with a focus on the reduction process that was previously only observed via XPS analysis. We used advanced scanning transmission electron microscopy (STEM) techniques to gain spatial-elemental and morphological information on the transformation of $AuCl_4^-$ to $Au^0$ through reduction with sodium citrate in an octadecylamine medium. Concepts of comminution, mechanical activation, chemical reduction and aging are important to the framework of this chapter.

M. Ferguson[†], A. J. Richard[†], J. Valdez, B. G. Fiss, H. M. Titi, N. Provatas, T. Friščić and A. Moores, *Faraday Discuss.*, 2022, Accepted.

[†] These authors contributed equally to this work.

## 3.1    Abstract

We used a gold nanoparticle synthesis as a model system to study the morphological and compositional changes in gold(III) precursor particles, while reduction was taking place in an aging setting after mechanical activation. Scanning transmission electron microscopy coupled with a high-angle annular dark field detector revealed the nanoscale changes in particle morphology while electron energy loss spectroscopy mapped the changes in the chemical landscape during the reduction process. Tracking a specific region of interest on the sample grid allowed for comparisons to be made of the same particles across a two day monitoring period. High-angle annular dark field images permitted the visualization of particle size reduction of the gold salt while electron energy loss spectroscopy captured the surprising mobility of the lighter chlorine and sodium ions in a solid matrix during the reduction process. This system offers unique insight into precursor particle reactivity in the solid phase, which is relevant for many mechanochemical and aging-based reactions.

## 3.2    Introduction

Mechanochemistry, which boasts advantages such as the avoidance of bulk solvent, increased reaction efficiency, and the potential to synthesise previously unobtainable products,[1–4] has demonstrated great potential in meeting the Twelve Principles of Green Chemistry.[5,6] With a surge in interest over the past two decades researchers in the field have developed a wide range of synthetic applications which include, pharmaceutical co-crystals,[7] small molecule organics,[8,9] coordination polymers,[10] solid-state electrolytes,[11] catalysis,[12] and nanoparticles.[13,14] Therefore, it has been said that mechanochemical approaches may provide pathways to meet the United Nations Sustainable Development Goals (UN SDGs).[15,16] For mechanochemistry to take a prominent role in addressing the SDGs, wide-scale industrial adoption of the approach is required. However, there is a key barrier standing in the way, the incomplete understanding of solid-state reactivity. A question that is particularly acute in the context of nanoparticle synthesis.

A wide range of nanoparticles have been synthesised through mechanochemical approaches as recently reviewed.[13] In 2009, Debnath *et al.* reported the first

mechanochemical route to stabilised gold nanoparticles (AuNPs) using NaBH$_4$ to reduce KAuCl$_4$ in the presence of polyvinylpyrrolidone (PVP).[17] In 2014, we demonstrated a mechanosynthesis of ultrasmall (1.5–2.0 nm) monodisperse AuNPs through the galvanic reduction of HAuCl$_4$ using long chain amines as the stabilising agent,[18] while Monflier, Hapiot and coworkers showed that cyclodextrins were also capable of producing ultrasmall AuNPs in the solid state.[19] Later, de Oliveira *et al.* used the mechanochemical strategy to create AuNP seeds that form nanotadpoles when grown in a colloidal solution.[20] With wide ranging applications, from electronics to photodynamic therapies,[21] and an increasing number of mechanochemical strategies to sustainably produce AuNPs,[13,22] more emphasis is being placed on understanding the underlying processes of AuNP growth.

The last decade has seen tremendous developments towards the mechanistic understanding of mechanochemical reactions through the development of *in situ* methods. *In situ* powder X-ray diffraction (PXRD) protocols using synchrotron radiation, developed in 2013,[23] have proven to greatly enhance our ability to understand mechanochemical reactivity.[24] This was quickly followed by the development of *in situ* Raman spectroscopy in 2014[25] and the two were quickly combined together to achieve tandem measurements in 2015.[26] Since then, the range of techniques to directly observe the solid reactions has expanded to include fluorescence,[27] X-ray absorption[28] and nuclear magnetic resonance spectroscopy.[29] These developments have provided a wealth of insight into mechanochemical reactions and have been recently discussed at length by Michalchuk & Emmerling.[30] In the context of AuNP synthesis, the groups of Camargo & Emmerling have investigated the kinetics of gold salt reduction through both *ex situ* PXRD,[31] and by tandem *in situ* PXRD-X-ray absorption near edge spectroscopy (XANES) measurements.[28] The XANES protocol allowed the redox state of gold to be followed as it was reduced while PXRD measurements tracked the growth of the resultant nanoparticles. Finally, on the theoretical side, our group recently developed a structural-phase-field-crystal model with the goal of exploring how AuNPs emerge from a solid matrix of longchain amines.[32] Despite these developments, we are still lacking the means to directly observe events at the nanoscale, especially morphological changes and

amorphous matter. Transmission electron microscopy (TEM) is a key technique for analysing nanoparticles, providing direct visualisation of the size and morphology of the resultant particles, but it can only be applied *ex situ* after samples are suspended in a solvent and drop-cast. An *in situ* TEM set up, while samples are subject to the constant agitation that is common to mechanochemical reactions, is unpractical, since the maximum thickness of the sample should in the range of 200–300 nm[33] and must remain as still as possible [34]. However, this does not rule out TEM as a technique for the *in situ* analysis of solid state reactivity. Notably, Da Silva *et al.* observed *in situ*, electron beam induced surface crystallisation of $BiFeO_3$ perovskites that were synthesised mechanochemically.[35] Aging reactions, whereby reaction systems are initially mixed and then are allowed to develop over time, present a possible solution.[36] By mixing the reaction components and then casting them onto a TEM sample grid, we can treat that grid as an individual aging reactor. We thus took inspiration from various reports of mechanically-activated aging syntheses of nanomaterials[37] to slow down the mechanochemical synthesis of AuNPs and allow a TEM study of particle growth in the solid state. We recently developed such a methodology, milling $HAuCl_4 \cdot 3H_2O$, sodium citrate (NaCt) dihydrate, and octadecylamine (ODA) for 60 s in a vibrational ball mill. The samples were then aged for a period of six weeks at -18 °C, 21 °C and 32 °C.[38] Analysis of the resulting powders by X-ray photoelectron spectroscopy (XPS), diffuse reflectance spectroscopy (DRS), PXRD and TEM, allowed a deep mechanistic analysis of the reaction. We could track the growth of nanoparticles, track gold reduction and evaluate an activation energy for this reaction.

As a follow up to this work, we focused on the study of the precursor particle morphological and compositional changes at the beginning of this reaction. Herein we present a solid-state TEM study of the mechanically activated aging reduction of $HAuCl_4 \cdot 3H_2O$, Figure 3.1, which occurs in the initial stages of the formation of amine stabilised AuNPs. Scanning electron transmission microscopy (STEM) combined with electron energy loss spectroscopy (EELS) allowed us to observe the reduction in precursor particle size and directly observe and map the reduction process.
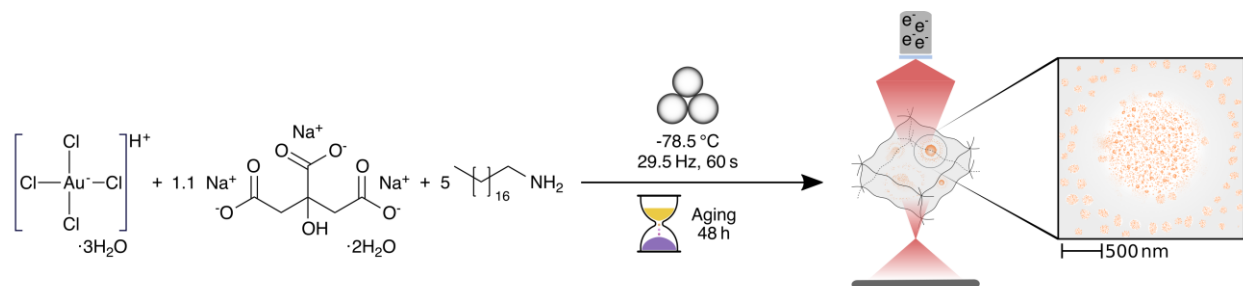
**Figure 3.1** Synthesis of amine-stabilised AuNPs through the brief mechanical activation and subsequent aging of the reaction components.

## 3.3    Experimental

### 3.3.1  Synthesis

All chemicals were obtained from MilliporeSigma and used without further purification. The AuNPs formed in this study were produced in a similar fashion to that of our previous work.[38] Typically, a 15 mL zirconia milling jar (Form-Tech Scientific), one 10 mm zirconia milling ball, 47.7 mg of $HAuCl_4·3H_2O$ (0.121 mmol), 163.2 mg of 1-octadecylamine (0.605 mmol), and 39.2 mg of trisodium citrate dihydrate (0.133 mmol) were chilled separately over dry ice for approximately one hour. Then, the milling ball and three solid reactants were added to the jar which was sealed and shaken on a Retsch MM400 mixer mill at 29.5 Hz for 60 s, upon which a free flowing yellow powder was obtained. The powder was transferred to a sample vial and stored in the dark at room temperature (21 °C). Note: to avoid the potential for galvanic reduction, $HAuCl_4·3H_2O$ and the resulting milled powder were manipulated with a PTFE coated spatula.

### 3.3.2  Transmission electron microscopy

STEM studies were performed using a Thermo Scientific Talos F200X transmission electron microscope equipped with a high brightness XFEG Schottky source, operated at 200 keV. Electron energy loss spectroscopy measurements were performed using an Enfinium ER977 dual-EELS gatan imaging filter (GIF) camera. Due to difference in the electron loss signals, EELS analyses for chlorine were collected separately from gold and sodium. For chlorine, which has a lower electron loss signal, the spectrum image was collected with an energy dispersion of 0.1 eV per channel and an exposure time of 0.5 s

per pixel. Gold and sodium have higher electron loss signals and therefore the spectral images were collected with an energy dispersion of 1 eV per channel and an exposure time of 0.8 s per pixel.

STEM sample grids were prepared in the solid-state. A 200 mesh Cu grid with a 15 nm thick SiOx substrate coating was introduced into the milled powder and impregnated with sample by agitating the recipient. Once impregnated, pressurised air was used to remove excess sample from the grid. The sample was analysed using STEM coupled with the high-angle annular dark field (HAADF) detector. The positional coordinates of regions of interest on the grid were recorded to permit their tracking at different stages during the aging period. When not loaded in the instrument, the grid remained in the sample holder to ensure that the previously recorded coordinates would lead back to the same region of interest.

## 3.4    Results and Discussion

### Solid State Reduction of HAuCl$_4\cdot$3H$_2$O

Typically, S/TEM grids for NP observations are prepared by dropcasting, a method by which NPs are suspended in a solvent to ease NP deposition and spreading. Yet solvent dispersion can induce morphological and chemical changes in NPs.[38] Therefore, to monitor the changes to the HAuCl$_4$ particles during the solid-state process, we employed the solid-state grid preparation outlined in the experimental section.

Freshly milled powder was deposited on the grid and excess powder removed. The grid was mounted to the sample holder and a first TEM measurement was performed. Thereafter, the sample-holder with the grid on it was removed from the microscope, covered and stored at room temperature for a total of 48 h. Two other TEM measurements took place, at 24 and 48 h. At t=0 h, the precursor particles are typically in the order of ≈5 $\mu$m.[39]

Therefore, STEM-HAADF analyses were performed at a magnification of ×16.3 k– ×36 k, and EELS measurements were used to perform the elemental mapping of the gold and chlorine in the sample. EELS was preferred over energy dispersive X-ray

spectroscopy (EDXS),[40] which may cause losses in spatial resolution when analysing samples at lower magnification.[41] When the prepared grid for the freshly milled powder was studied, a large approximately spherical particle, $\phi$ 1.35 $\mu$m, was found, Figure 3.2(a). Interestingly, the particle was surrounded by a ring of smaller particles. There was evidence of similar encirclements in other areas of the sample. EELS mapping for Au and Cl atoms, Figure 3.2(b-c), confirmed that these particles were comprised of $HAuCl_4$, through the strong signal of each element and a high degree of overlap of the signals. Upon confirmation that this was indeed the Au(III) precursor, the position of the camera was recorded to permit its relocation in the future. After 24 h the particle was successfully relocated albeit with a slight rotation,[h] Figure 3.2(e). The elemental map for gold appears similar in intensity while for chlorine there is a clear reduction, Figure 3.2(f-g). This is more evident when looking at the encircling particles as the Cl signal is visibly much weaker than the previous day. This trend was confirmed by calculating the normalised electron count per element from the EELS data, Figure 3.2(m), where the relative gold signal increased by 6% whereas the chlorine signal decreased by 71%. This is a clear sign of chlorine loss in the central particle region. After a further 24 h the normalised Cl intensity was consistent with the previous day, but with an increased dispersion throughout the sample area, Figure 3.2(i). In contrast, the signal for gold remained spatially consistent with those of the previous day, Figure 3.2(j-k). This is further evidenced in Figure 3.2(n) which shows minimal change in the relative distribution of the Au signals over the two day aging period. The significant decrease of chlorine signal with respect to gold demonstrates a clear difference in the solid-state diffusivity of the species. We attribute this to the mass difference between the species, gold being five and a half times heavier than chlorine likely reduces its ability to move through the wider solid matrix of NaCt and ODA.

---

[h] This slight rotation is caused by subtle movements of the TEM grid when the sample holder is inserted into, and removed from, the instrument.
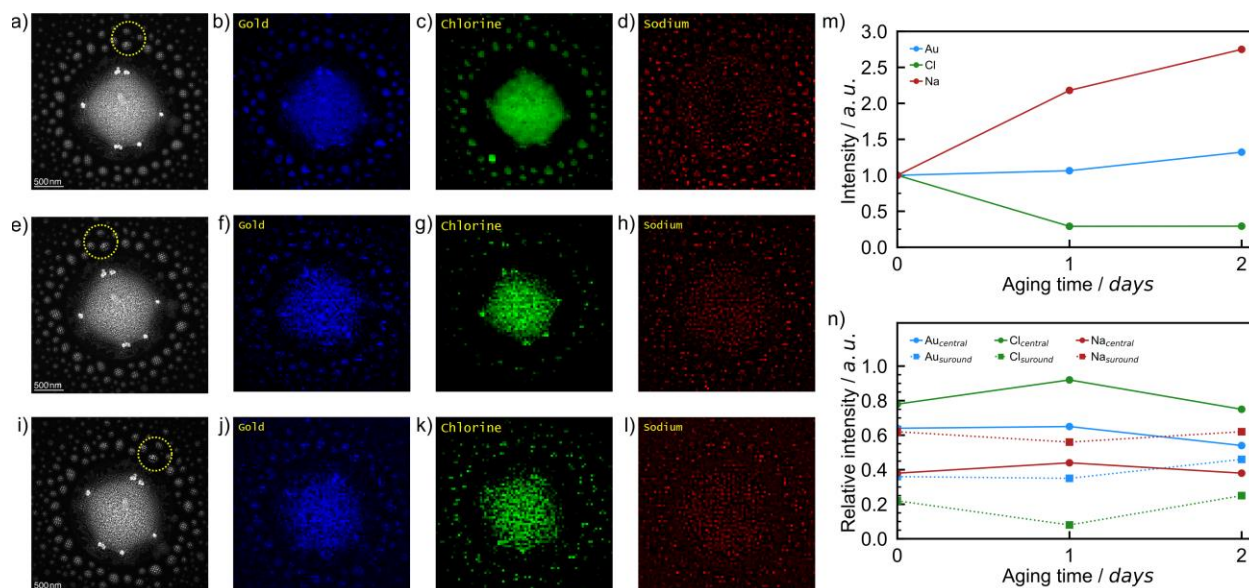
**Figure 3.2** STEM-HAADF images and EELS elemental maps for Au, Cl, and Na (left to right, respectively) for freshly milled powder (a-d), after 24 h of aging (e-h), and after 48 h of aging (i-l). In all cases the same particle was studied. The total intensity of each element in EELS images are given in (m) normalised to the freshly milled powder. The relative EELS intensities for each element over the central particle (solid lines) and its surroundings (dotted lines) are shown in (n). Gold, chlorine, and sodium are represented by blue, green, and red, respectively. Yellow circles (a,e,i) indicate a group of nanoscale particles that we are also examined during the aging process.

Studying the EELS mapping images for sodium provides further insights. The spectral image for sodium of the freshly milled powder, Figure 3.2(d), shows more prominent distributions in the area surrounding the main particle in the image with intensities over the central region that are much lower than those observed for Au or Cl. This is consistent with the idea that the central particle is almost entirely inorganic in nature. Upon aging, the sodium signal increased in intensity over the principal particle in the region of interest, where the total electron count for sodium more than doubled after 24 h and almost tripled after 48 h. This suggests that NaCl molecules have enough mobility, even at room temperature, to move through the solid material on the grid where they presumably react with gold(III). This gradual solid-state reduction is further confirmed by the significant decrease in Cl intensity during the same aging period. The principal particle in the STEM-HAADF images of Figure 3.2 and the corresponding elemental maps provide the microscale view of the solid-state reduction. We then focused on the small particles that encircle the main particle, Figure 3.2 yellow circles, we were able to visualise the reduction process on the nanoscale. The selected area contained several clusters of

particles, Figure 3.3(a), which were successfully relocated after 24 h and 48 h of aging, Figure 3.3(b) and (c), respectively. To facilitate the relocation and analysis on the nanoscale, we selected the cluster that appeared to exhibit the highest intensity in the image, Figure 3.3 (a-c) cyan circles, which corresponds to the cluster that contains the most gold. Within the selected clusters there was a formation of three particles that we focused on to study the changes in morphology and HAADF intensity with aging. Each of which have diameters of ≈ 20 nm, Figure 3.3 (d-f). Image orientation was adjusted so patterns were preserved from one image to the next, to allow for direct comparison. Visual inspection of the images shows a significant loss of signal in the areas surrounding the particles as time progresses. Taking the leftmost particle of the three, its effective diameter appears to remain consistent between days zero (d) and one (e), but appears reduced after two days (f) of aging. The central and rightmost particles, however, appear to be discrete in the freshly milled powder (d) but their HAADF signals become more continuous with aging (e-f).
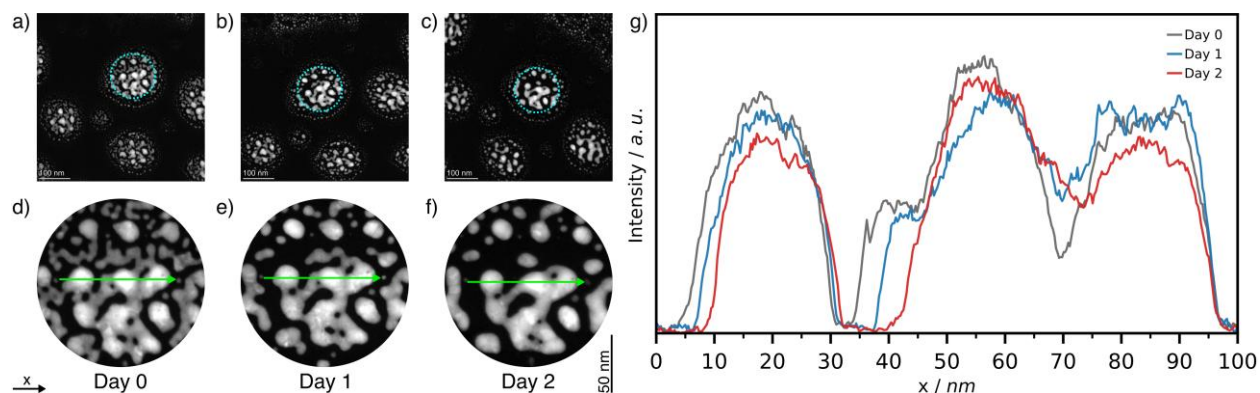


**Figure 3.3** STEM-HAADF images of small clusters of precursor particles for freshly milled powder (a), after 24 h (b), and after 48 h of aging (c) accompanied by a zoomed image of a selected cluster for each aging period (d-f). The normalised HAADF intensities (g) over 100 nm line scans (green arrows) for freshly milled powder (grey), after 24 h (blue), and after 48 h (red) of aging.

To further understand these effects we performed HAADF intensity analysis using line scans over the three chosen particles. Scans were performed over a 100 nm line running through the centre of the three particles, Figure 3.3(d-f) green arrows, with resulting normalised HAADF intensities for the three samples plotted in Figure 3.3(g). The leftmost particle, appearing in the x range of 5.0–32.5 nm, decreased in size after each day of aging. The plots reveal that the particle's diameter decreased by ≈3.4 nm after 48

h of aging. There is also a defined decrease in the maximum HAADF intensity as the sample ages, suggesting that the remainder of the particle that is visible in the image has reduced in mass. HAADF intensity corresponding to the surroundings of the three chosen particles can be found at x ≈37.5 nm, which after the two day aging period in this study was reduced to zero. This indicates the inherent mobility of particles in the solid matrix while at room temperature (21 °C). The remaining two of the chosen particles are represented by the intensity signals where x ≥45 nm. While the breadth of the signal remains consistent over the three measurements, there is a decrease in maximum intensity after 48 h. In the case of the freshly milled powder, there is a significant drop in intensity at x =70 nm. The intensity at this point increased with aging which acts to confirm that the two particles appear to merge over time. We suggest that this is a result of the particles reacting with NaCt and the resulting Au(0) atoms/clusters merging. Once again, this shows a remarkable amount of mobility in a solid-system that is not being actively mixed or agitated.

Gold salts are prone to reduction during XPS and XAS measurements,[42,43] and by direct exposure to electron beams.[44] To control for this, we impregnated a STEM grid with freshly milled powder before capturing a STEM-HAADF image and EELS spectral images for Au, Cl, and Na three times, with no intermittent aging. This exposed the grid to the same electron beam dosage as samples aged for 48 h. Images and elemental maps, Figure 3.4, remain identical between the initial (a-d), second (e-h), and third (i-l) collections, indicating no significant changes in the sample upon exposure to the beam. The normalised intensity of the signals for Cl, Figure 3.4(m), relative to the initial scan, showed a reduction after three scans (17%), significantly less than when the sample is aged between data collection scans (71%). This confirms that the majority of the reduction observed in the sample aged for 48 h is aging-induced.
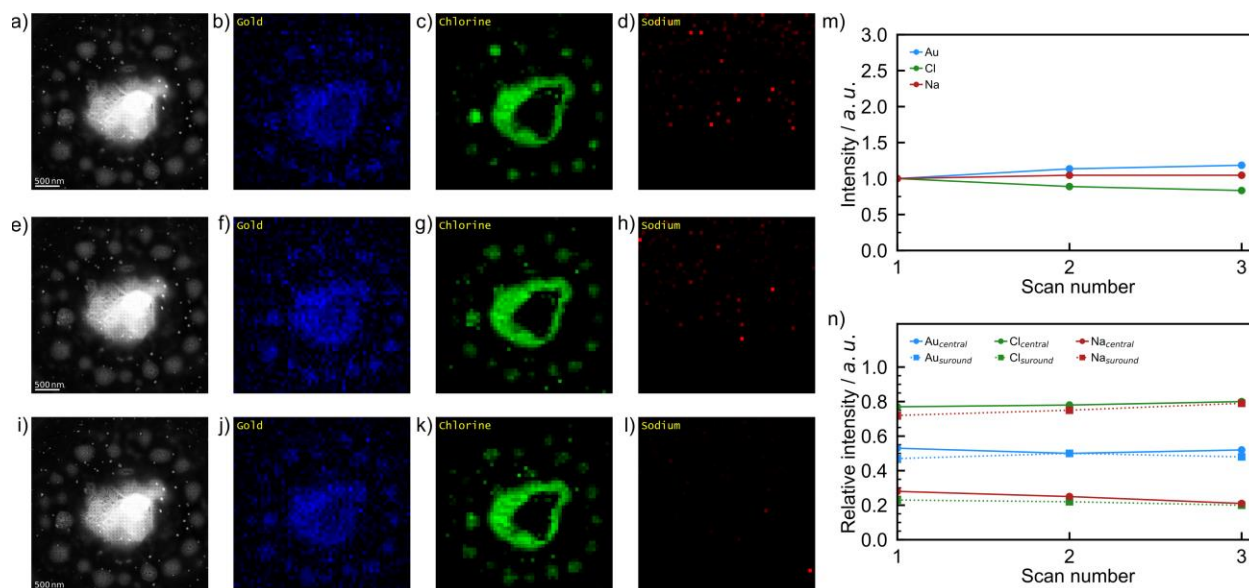
**Figure 3.4** STEM-HAADF images and EELS elemental maps for Au, Cl, and Na (left to right, respectively) for freshly milled powder (a-d), immediately after the initial measurements (e-h), and after a second set of measurements (i-l) to control for electron beam induced reduction of the precursor. In all cases the same particle was studied. The total intensity of each element in EELS images are given in (m) normalised to the freshly milled powder. The relative EELS intensities for each element over the central particle (solid lines) and its surroundings (dotted lines) are shown in (n). Gold, chlorine, and sodium are represented by blue, green, and red, respectively.

## 3.5 Conclusions

The present study demonstrated the use of transmission electron microscopy as a means to study solid-state aging reactions. More specifically, the reduction of $HAuCl_4 \cdot 3H_2O$ by sodium citrate (NaCt) dihydrate in the presence of a long chain (C18) primary amine that was induced by brief milling (60 s) in a vibrational ball mill. With sample grids prepared in the solid-state, STEM coupled with a HAADF detector was employed to track a specific grouping of precursor particles over the course of the aging period. In tandem, EELS spectral images were collected for the tracked particles and their immediate surroundings which permitted the study of the local distributions of key elements in the sample, Au, Cl, and, Na. Visual analysis of the collected images clearly showed the high degree of mobility of the reaction components in the solid-state, when not being continuously agitated. Combining the visual analysis with HAADF and EELS spectral image intensities provided a series of images that captured morphological and compositional changes at the micro and nanoscales during the reduction of $HAuCl_4$ under a mechanically-activated

aging process. This study provides a unique insight into the mobility in the solid phase during aging.

## 3.6 References

1. S. L. James, C. J. Adams, C. Bolm, D. Braga, P. Collier, T. Friščić, F. Grepioni, K. D. M. Harris, G. Hyett, W. Jones, A. Krebs, J. Mack, L. Maini, A. G. Orpen, I. P. Parkin, W. C. Shearouse, J. W. Steed and D. C. Waddell, *Chem. Soc. Rev.*, 2012, **41**, 413–447.

2. A. A. L. Michalchuk, E. V. Boldyreva, A. M. Belenguer, F. Emmerling and V. V. Boldyrev, *Front. Chem.*, 2021, **9**, 685789.

3. T. Friščić, C. Mottillo and H. M. Titi, Angew. *Chem., Int. Ed.*, 2020, 59, 1018–1029.

4. L. Takacs, *Chem. Soc. Rev.*, 2013, **42**, 7649–7659.

5. K. J. Ardila-Fierro and J. G. Hernández, *ChemSusChem*, 2021, **14**, 2145–2162.

6. P. T. Anastas and J. Warner, *Green chemistry*, Oxford University Press, London, England, 1998.

7. M. Solares-Briones, G. Coyote-Dotor, J. C. Páez-Franco, M. R. Zermeño-Ortega, C. M. de la O Contreras, D. Canseco-González, A. Avila-Sorrosa, D. Morales-Morales and J. M. Germán-Acacio, *Pharmaceutics*, 2021, **13**, 790.

8. G.-W. Wang, *Chem. Soc. Rev.*, 2013, **42**, 7668–7700.

9. D. Margetić and V. Štrukil, *Organic Synthesis*, IntechOpen, Rijeka, 2020, ch. 3.

10. T. Stolar and K. Užarević, *CrystEngComm*, 2020, **22**, 4511– 4525.

11. R. Schlem, C. F. Burmeister, P. Michalowski, S. Ohno, G. F. Dewald, A. Kwade and W. G. Zeier, *Adv. Energy Mater.*, 2021, **11**, 2101022.

12. A. Porcheddu, E. Colacino, L. D. Luca and F. Delogu, *ACS Catal.*, 2020, **10**, 8344–8394.

13. B. G. Fiss, A. J. Richard, G. Douglas, M. Kojic, T. Friščić and A. Moores, *Chem. Soc. Rev.*, 2021, **50**, 8279–8318.

14. P. Baláž, M. Achimovičová, M. Baláž, P. Billik, Z. Cherkezova- Zheleva, J. M. Criado, F. Delogu, E. Dutková, E. Gaffet, F. J. Gotor, R. Kumar, I. Mitov, T. Rojac, M. Senna, A. Streletskii and K. Wieczorek-Ciurowa, *Chem. Soc. Rev.*, 2013, **42**, 7571– 7637.

15. E. Colacino, F. Delogu and T. Hanusa, *ACS Sustainable Chem. Eng.*, 2021, **9**, 10662–10663.

16. United Nations, *Transforming Our World: The 2030 Agenda for Sustainable Development*, UN General Assembly, New York, USA, 2015.

17. D. Debnath, S. H. Kim and K. E. Geckeler, *J. Mater. Chem.*, 2009, **19**, 8810–8816.

18. M. J. Rak, N. K. Saadé, T. Friščić and A. Moores, *Green Chem.*, 2014, **16**, 86–89.

19. S. Menuel, B. Léger, A. Addad, E. Monflier and F. Hapiot, *Green Chem.*, 2016, **18**, 5500–5509.

20. P. F. M. de Oliveira, J. Quiroz, D. C. de Oliveira and P. H. C. Camargo, *Chem. Commun.*, 2019, **55**, 14267–14270.

21. V. Voliani, *Gold Nanoparticles*, De Gruyter, Berlin, Germany, 1st edn, 2020.

22. A. Moores, *Curr. Opin. Green Sustainable Chem.*, 2018, **12**, 33–37.

23. (*a*) I. Halasz, S. A. J. Kimber, P. J. Beldon, A. M. Belenguer, F. Adams, V. Honkimäki, R. C. Nightingale, R. E. Dinnebier and T. Friščić, *Nat. Protoc.*, 2013, **8**, 1718–1729; (*b*) T. Friščić, I. Halasz, P. J. Beldon, A. M. Belenguer, F. Adams, S. A. Kimber, V. Honkimäki and R. E. Dinnebier, *Nat. Chem.*, 2013, **5**, 66–73.

24. (*a*) L. S. Germann, A. D. Katsenis, I. Huskić, P. A. Julien, K. Užarević, M. Etter, O. K. Farha, T. Friščić and R. E. Dinnebier, *Cryst. Growth Des.*, 2019, **20**, 49–54; (*b*) L. S. Germann, M. Arhangelskis, M. Etter, R. E. Dinnebier and T. Friščić, *Chem. Sci.*, 2020, **11**, 10092–10100; (*c*) K. Užarević, N. Ferdelji, T. Mrla, P. A. Julien, B. Halasz, T. Friščić and I. Halasz, *Chem. Sci.*, 2018, **9**, 2525–2532; (*d*) G. I. Lampronti, A. A. L. Michalchuk, P. P. Mazzeo, A. M. Belenguer, J. K. M. Sanders, A. Bacchi and F. Emmerling, *Nat. Commun.*, 2021, **12**, 6134; (*e*) J. A. Alonso, P. Kayser, B.-K. Hong, M. C. Álvarez Galván, F. Fauth and C. Alberto López, *Materials*, 2021, **14**, 6039.

25. D. Gracin, V. Štrukil, T. Friščić, I. Halasz and K. Užarević, *Angew. Chem. Int. Ed.*, 2014, **53**, 6193–6197.

26. L. Batzdorf, F. Fischer, M. Wilke, K.-J. Wenzel and F. Emmerling, *Angew. Chem., Int. Ed.*, 2015, **54**, 1799–1802.

27. P. A. Julien, M. Arhangelskis, L. S. Germann, M. Etter, R. E. Dinnebier, A. J. Morris and T. Friščić, *ChemRxiv*, 2021, This content is a preprint and has not been peer–reviewed.

28. P. F. M. de Oliveira, A. A. L. Michalchuk, A. G. Buzanich, R. Bienert, R. M. Torresi, P. H. C. Camargo and F. Emmerling, *Chem. Commun.*, 2020, **56**, 10329–10332.

29. M. Leger, J. Guo, B. MacMillan, H. M. Titi, T. Friščić, B. Blight and B. Balcom, *ChemRxiv*, 2021, This content is a preprint and has not been peer–reviewed.

30. A. A. L. Michalchuk and F. Emmerling, *Angew. Chem., Int. Ed.*, 2022, **61**, e202117270.

31. P. F. M. de Oliveira, A. A. L. Michalchuk, J. Marquardt, T. Feiler, C. Prinz, R. M. Torresi, P. H. C. Camargo and F. Emmerling, *CrystEngComm*, 2020, **22**, 6261–6267.

32. L. Yang, A. Moores, T. Friščić and N. Provatas, *ACS Appl. Nano Mater.*, 2021, **4**, 1886–1897.

33. *Transmission electron microscopy*, ed. C. B. Carter and D. B. Williams, Springer International Publishing, Cham, Switzerland, 1st edn, 2016.

34. L. Jones and P. D. Nellist, *Microsc. Microanal.*, 2013, **19**, 1050–1060.

35. K. L. D. Silva, D. Menzel, A. Feldhoff, C. Kübel, M. Bruns, A. Paesano, A. Düvel, M. Wilkening, M. Ghafari, H. Hahn, F. J. Litterst, P. Heitjans, K. D. Becker and V. Šepelák, *J. Phys. Chem. C*, 2011, **115**, 7209–7217.

36. C. Mottillo and T. Friščić, *Molecules*, 2017, **22**, 144.

37. (*a*) C. A. O'Keefe, C. Mottillo, J. Vainauskas, L. Fábián, T. Friščić and R. W. Schurko, *Chem. Mater.*, 2020, **32**, 4273–4281; (*b*) S. Li, I. Huskić, N. Novendra, H. M. Titi, A. Navrotsky and T. Friščić, *ACS Omega*, 2019, **4**, 5486– 5495; (*c*) I. Bekri-Abbes and E. Srasra, *Materials Science in Semiconductor Processing*, 2015, **40**, 543–549; (*d*) M. Y. Malca, H. Bao, T. Bastaille, N. K. Saadé, J. M. Kinsella, T. Friščić and A. Moores, *Chem. Mater.*, 2017, **29**, 7766– 7773; (*e*) S. S. Ali, W. H. Eisa and A. Abouelsayed, *Composites Part B*, 2019, **176**, 107289; (*f*) K. Budny-Godlewski, I. Justyniak, M. K. Leszczyński and J. Lewiński, *Chem. Sci.*, 2019, **10**, 7149–7155; (*g*) K. Budny-Godlewski, M. K. Leszczyński, A. Tulewicz, I. Justyniak, D. Pinkowicz, B. Sieklucka, K. Kruczała, Z. Sojka and J. Lewiński, *ChemSusChem*, 2021, **14**, 3887–3894.

38. A. J. Richard, M. Ferguson, B. G. Fiss, H. M. Titi, J. Valdez, N. Provatas, T. Friščić and A. Moores, *ChemRxiv*, 2022, This content is a preprint and has not been peer–reviewed.

39. *Mixer Mill MM 400 A true multipurpose mill*, https://www.retsch.com/products/milling/ball-mills/mixer-mill-mm-400/function-features/, (accessed April 2022).

40. V. Šepelák, S. M. Becker, I. Bergmann, S. Indris, M. Scheuermann, A. Feldhoff, C. Kübel, M. Bruns, N. Stürzl, A. S. Ulrich, M. Ghafari, H. Hahn, C. P. Grey, K. D. Becker and P. Heitjans, *J. Mater. Chem.*, 2012, **22**, 3117–3126.

41. J. Titchmarsh, *Ultramicroscopy*, 1989, **28**, 347–351.

42. (*a*) M. Sankar, Q. He, M. Morad, J. Pritchard, S. J. Freakley, J. K. Edwards, S. H. Taylor, D. J. Morgan, A. F. Carley, D. W. Knight, C. J. Kiely and G. J. Hutchings, *ACS Nano*, 2012, **6**, 6600–6613; (*b*) J. Radnik, C. Mohr and P. Claus, *Phys. Chem. Chem. Phys.*, 2003, **5**, 172–177.

43. Y. Ohkubo, T. Nakagawa, S. Seino, J. Kugai, T. A. Yamamoto, H. Nitani and Y. Niwa, *J. Synchrotron Radiat.*, 2014, **21**, 1148–1152.

44. Y. Kim, W. Song, S.-I. Lee, S. Youb Lee, M.-J. Cha, D. Sung Jung and C.-Y. Park, *Appl. Phys. Lett.*, 2013, **102**, 223116.

# 4    Discussion and Conclusion

This chapter will extend the discussions of Chapters 2 and 3, posing questions and communicating findings that may be of interest to this thesis but ultimately did not have a suitable place in the more concise manuscripts. Connections between these works and preceding works will also be made, touching on commentary made by others in the field of bottom-up nanoparticle mechanosynthesis. Concluding remarks are made and suggestions will be given to direct future work on the subject.

## 4.1    Discussion of Findings

First, certain conclusions from the work in Chapter 2 will be reviewed in comparison with conclusions from related works. There exists an interesting discrepancy between the findings of Chapter 2 and those from the work of Emmerling and co-workers investigating different reducing agents for the mechanosynthesis of AuNPs.[1] Their group found that the strength of reducing agents did not follow conventional solution state understanding, that being $NaBH_4$ > AA > HQ > NaCt, where $NaBH_4$ is the strongest and fastest acting reducer, and NaCt is the weakest and slowest acting reducer. Rather, they discovered that the reductants obeyed a different order of strength: HQ > AA > NaCt > $NaBH_4$ (Figure 4.1). Most astoundingly, $NaBH_4$ went from being the most powerful to the weakest of the reductants tested.
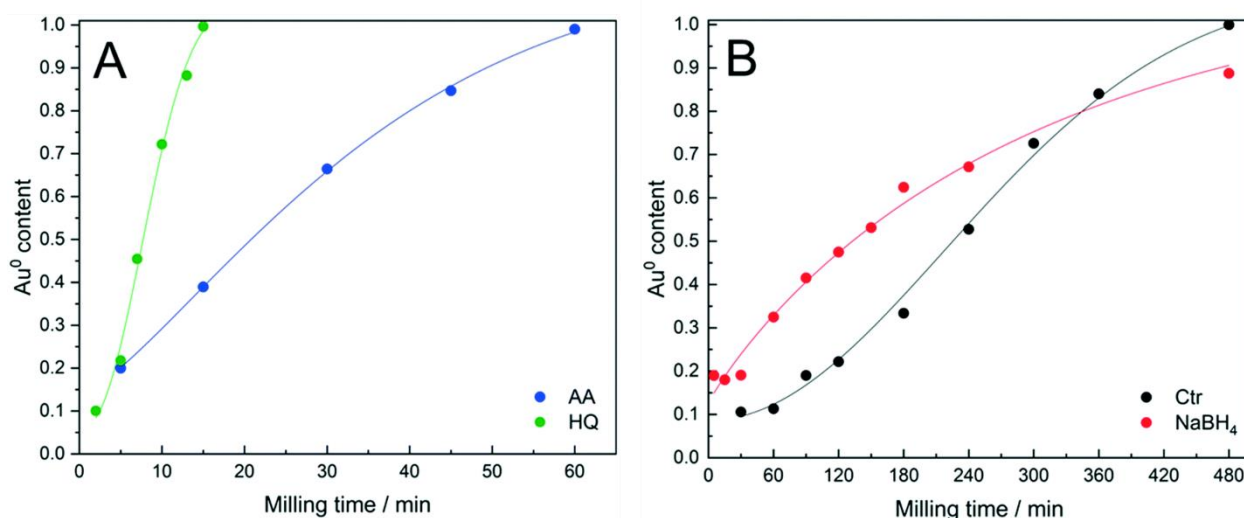


**Figure 4.1** Apparent rates of AuCl reduction towards AuNP formation. Reactions are shown for (A) $R_A$ = AA and HQ; (B) $R_A$ = NaCt (AuCl : NaCt molar ratio 1 : 1/3), $NaBH_4$. Reproduced from Ref. 1 with permission from the Royal Society of Chemistry.[1]

In our preliminary studies to create an aging reaction for AuNP mechanosynthesis, we used this work as inspiration and tested all these reductants in their capacity to function as slow progressive reducers. Our experiments showed that $NaBH_4$ was too strong of a reducing agent to support an aging reaction, certainly stronger than NaCt which was ultimately used as the reductant of choice for aging. Whether milled in a ball mill for 1 minute, 5 minutes, or 90 minutes, samples that contained $NaBH_4$ consistently turned a purple-to-black colour. Contrastingly, when samples were milled with NaCt for 1 or 5

minutes the powder always emerged a golden yellow or orange colour, and even after milling for 90 minutes the solid would at most turn brown. Only when left to age for days to weeks would the solid mixture with NaCt darken further and begin to resemble its $NaBH_4$ counterpart. To account for this disagreement, we considered the differences between experimental conditions and hypothesized that the most likely culprit is the choice of ligand. Emmerling and co-workers had used PVP, a polymeric ligand, while the work herein used ODA, a molecular ligand. In solid-state mechanochemical reactions such as these, when ligands are employed in high excess they may double as both a capping agent for the nanoparticle product and as a dispersant for the reaction mixture. Thus, the properties of the solid medium likely reflect those of the pure ligand and may dictate species mobility, mixture density, electrical permeability, degree of crystallinity and more. It is known that in solution-state reactions the choice of solvent has influence over reaction behavior.[2-5] Therefore while a similar behavior between the solid and solution states is observed, the manner through which this behavior manifests is possibly also a source of difference between the two.

In Moores and co-workers' 2017 work on $Bi_2S_3$ NPs, they found that it did not matter whether the mechanical activation was done with a ball mill or using a pestle and a mortar: the reaction was activated regardless of the tool and the resulting nanoparticle size and size dispersity was largely unaffected.[6] It was found that the aging reaction of AuNPs designed in Chapter 2 was only weakly activated by using a mortar with a pestle, resulting in a much lower plasmonic signal compared to activation with a ball mill. Samples made via 1 minute of grinding or milling were analysed with DRS, both immediately after milling and after one week of aging, to observe the changing LSPR peak (~ 550 nm) from newly formed AuNPs (Figure 4.2). Half of the solid powder from each preparation technique was kept at room temperature for aging (21 °C), while the other half was aged in an oven at an elevated temperature (32 °C). Interestingly, the growth of AuNPs in powder aged at room temperature was strongly dependent on the choice of mechanical energy input but the growth of AuNPs in powder aged at the elevated temperature was not.
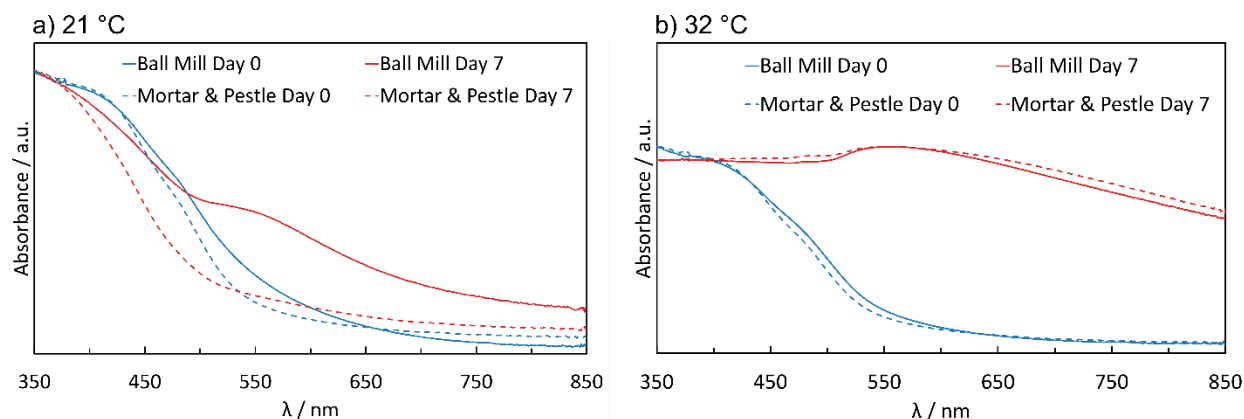
**Figure 4.2** DRS profiles of solid mixtures prepared by ball-milling and mortar & pestle grinding. Scans were taken immediately after milling/grinding and again after 7 days of aging at a) 21 °C or b) 32 °C.

In the concluding remarks of M. Y. Malca's 2017 M.Sc. thesis, the first author of the aging synthesis of $Bi_2S_3$ paper, he wrote that the observation of ultrasmall and monodisperse nanoparticles produced during an aging period implies mediation through sporadic defect formation or amorphization and that mechanisms such as these would produce a more polydisperse product.[7] He continued by saying that the ability to initiate a reaction with mild grinding in a mortar and pestle alludes to the reaction being dependent on reagent mixing or the reaction having a low activation energy barrier. The former comment is notable because our AuNP synthesis does produce polydisperse sizes of particles and because defects such as contact twinning, stacking faults, and grain boundaries have all been observed in our AuNPs. This suggests that the mechanochemical reactions to form $Bi_2S_3$ NPs and AuNPs may be mediated by different mechanisms.

The latter comment is relevant for two reasons, firstly because we know through the STEM characterization in Chapter 3 that an inhomogeneous milled mixture will still spontaneously reduce the metal salt precursor. Attempting to lower the milling frequency to 20 Hz and shrink the milling ball size to 7 mm both afforded visibly worse mixing; however, the solid still changed colour within days, bringing into question the dependency on the degree of mixing. Secondly, based on the data in Figure 4.2, an 11 °C increase in ambient aging temperature appeared enough to overcome the energy barrier that moderate grinding using a mortar and pestle could not. As suggested by Malca, it is likely that there is a small, but important activation barrier.

TEM investigation of the aging AuNP reaction was marked by obstacles that have thus far gone undiscussed in the literature. Most notable is the observation of precursor particles alongside product particles. Using simple brightfield TEM or STEM-HAADF microscopy, it is mostly impossible to tell one from the other. One could use lattice fringes to confirm the d-spacings of an Au nanocrystal, however ultra high-resolution magnifications are impractical for statistical sizing. Spatially resolved elemental analysis with STEM-EELS and STEM-EDX techniques would allow discrimination between a noble metal and a metal salt nanoparticle. However, the presence of a wide polydisperse population of particles, necessitating imaging at different magnifications, means that taking S/TEM micrographs is significantly more time and cost efficient than capturing elemental maps. The solution presented in Chapter 2 was to analyze the change in the population distribution over the aging period. This approach successfully generated a semi-quantitative measure of precursor size depletion and product size growth behaviors but was unable in most cases to quantify average particles sizes for an isolated species. This speciation problem occurred whether sampling was done in the solid state or by solution dropcasting, although the latter may also introduce solution interference such as rapid partial-reduction.

By-product particles may also make particle distinguishability difficult. Early in the work described in Chapter 2, it was discovered through dropcast-prepared brightfield TEM that the mechanosynthesis reaction to produce AuNPs was also producing nanocrystals of NaCl salt. Fortunately for this analysis, the NaCl was easily distinguishable from the Au-based precursor and product due to a strong difference in contrast stemming from electron-matter interactions. However, this led us to question what kind of reduction and formation process was occurring within the solid. Does the NaCl by-product form before or after the main AuNP product, and at what rate? Or was the formation of NaCl simply a result of the brief solution dispersion for dropcast TEM sample preparation? When solid-state TEM sampling was employed to verify the presence of AuNPs in the powder, it was found that the NaCl did in fact co-exist as a distinct nanosized species. Unlike AuNPs the NaCl nanocrystals were observable

immediately after milling, demonstrating a fast and strong tendency for NaCl formation that does not depend on AuNP formation (Figure 4.3).
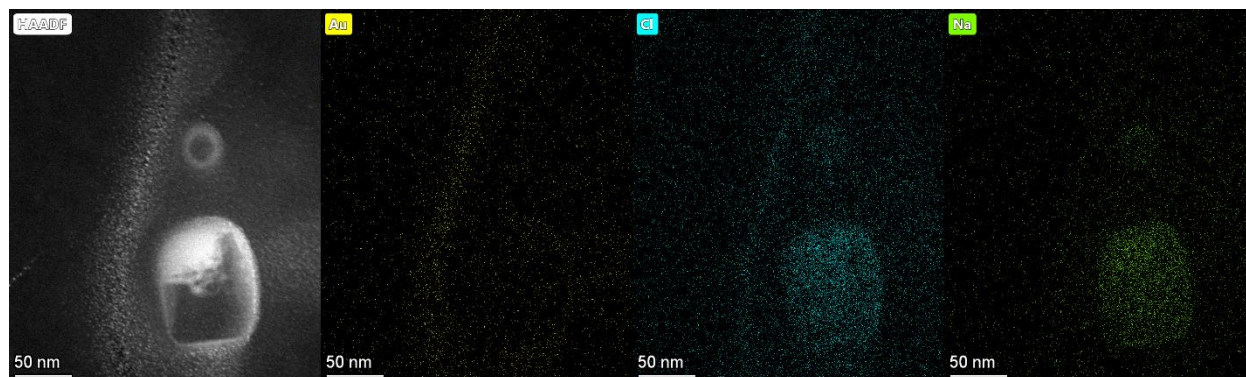


**Figure 4.3** STEM-EDX micrographs of a freshly milled powder. A long stream of small HAuCl$_4$ precursor particles can be seen running vertically to the left of two large NaCl salt structures.

In Chapter 3, when discussing reasons for the observed difference in species mobility, the difference in species mass was singled out as a probable factor of influence. It was noted that the mass of gold is five and a half times heavier than the mass of chlorine. However, the EELS data presented in Figure 3.2m showed that the sodium signal intensity, representative of the NaCt species, increased by roughly two times more than the gold signal intensity after 48 hours of aging. How then can one account for the greater observed mobility of the sodium-based species given that the mass of the NaCt species is 31% heavier than gold? One possibility is a strong electrostatic attraction between the sodium cations found in the organic species and the chlorine anions found in the inorganic species, an interaction that causes an accelerated migration of the sodium species inward and an outward migration of chlorine. Another possibility is that the ligand, which is also initially absent from the region occupied by the inorganic material, pulled along the NaCt as it diffused into the inorganic structures. In Figure 4.4, the EELS maps for C that were collected alongside the elemental maps of Figure 3.2 show the strong segregation of the inorganic species (HAuCl$_4$) from the organic species (ODA and NaCt). Because the ODA in the solid was used in much higher amounts than the other carbon containing species, NaCt, it was more appropriate to use Na to track the reductant and C to track the combined ligand and reductant. The apparent strong migration of C into the regions occupied by the inorganic precursor could potentially be responsible for the strong observed migration of NaCt into these same regions.
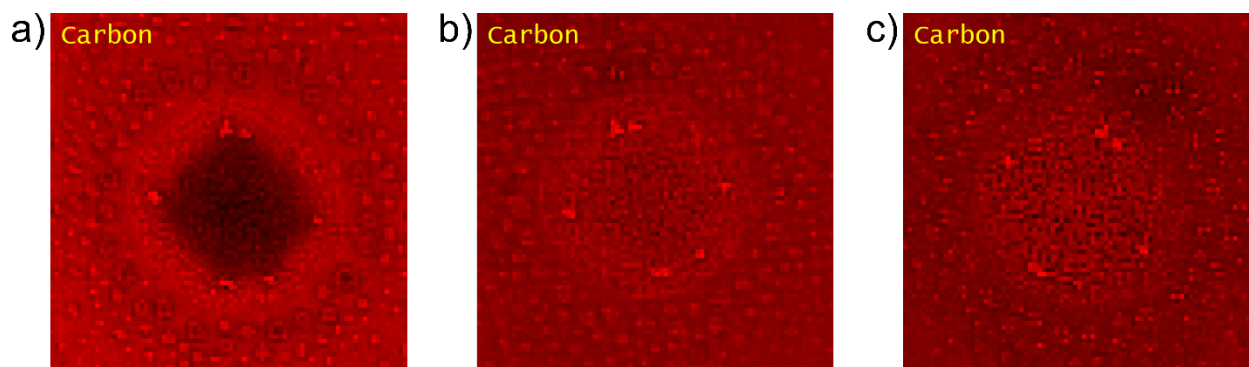
**Figure 4.4** Carbon EELS maps collected alongside the elemental maps for chlorine from Figure 3.2. Here is seen the qualitative assessment of C intensity on days a) zero, b) one, and c) two of aging.

The high-resolution STEM-HAADF micrograph analysis from Figure 3.3 appears to show material that disappears altogether. Though this was touched on in the discussion of Chapter 3, the explanation offered was limited to acknowledging that the $HAuCl_4$ was likely reacting with the NaCt and causing inorganic particles to breakdown. However, this does not explain why the material vanishes instead of simply moving or morphing in some way. During the initial 48 hours of reduction before the first AuNPs can be observed, the smallest precursor particles and the edges of the larger particles experienced the most visually distinguishable change. Since from the EELS maps the gold species were observed not to be very mobile on the micrometer scale, it may be that at this much higher magnification the movement of the smallest particles of gold precursor is much more perceptible. It could be argued then that the reduced material (<1 nm) spreads out into the empty space between particles through diffusion and by consequence of being much less densely packed is less likely to exhibit a strong signal. It is also important to remember that this is a 3-dimensional space, and that material can move upwards or downwards out of focus of the electron beam.

## 4.2    Concluding Remarks and Future Work

An aging bottom-up mechanosynthesis of AuNPs was designed in the solid state using tetrachloroauric (III) acid, a long chain amine ligand, and trisodium citrate dihydrate as a slow-acting reductant. Under brief high-energy and low temperature milling a well-mixed free-flowing and mechanically activated yellow powder was produced. Initially unreduced, the reaction between the gold salt and the reducer was observed to persist

for days to weeks, although most of the reduction occurred within the first couple days. Formation of the resulting AuNPs continued for weeks beyond the first observation of newly nucleated nanoparticles. Visibly, the milled powder changed colour from bright yellow to a dull and faded yellow, then to a reddish brown, before settling on a deep purple characteristic of nano-gold. The aging process was highly dependent on the surrounding thermal energy, which could be used to completely halt the reaction at low temperatures or greatly accelerate the reaction at elevated temperatures.

The reduction and formation processes were followed and quantified using mostly solid-state techniques that avoided solution interference effects. Sigmoidal growth kinetics extracted from DRS analysis were intriguingly reminiscent of previous mechanochemical literature that studied the dynamic material properties of milled solids. An exponential dependence on aging temperature was recorded from VT-PXRD analysis and an average activation energy for AuNP growth in the solid state of 159.38 kJmol$^{-1}$ was calculated. The two different approaches used to experimentally calculate growth activation energy from the Arrhenius equation fell within a comfortable 1.2% discrepancy of each other. This kind of quantitative kinetic and growth data is important to furthering our understanding of bottom-up mechanosynthesis in the solid state. Presuming that similar aging systems can be created using other metals, it would be formative to the field to begin comparing kinetics and growth activation energies of different MNPs in the solid state.

Where dispersion in solvent was necessary for brightfield electron microscopy, it was possible to gain information not from the absolute sizes but from changes in the size distribution throughout the aging period. This led to the discovery of the earliest observable AuNPs around 1 nm in diameter after only 48 hours of aging at room temperature. In turn, this discovery inspired the solid-state STEM-EELS investigation wherein the localization and mobilities of different organic and inorganic species in the milled solid were tracked through spatially resolved elemental analysis. Chlorine and sodium were found to be particularly mobile whereas gold remained relatively stationary and highly locally concentrated. It would be fascinating to study the formation of binary nanoparticles under these circumstances and attempt to observe a coalescence of

species as opposed to a dissociation. Because of the strong influence of the ligand as the majority constituent of the solid, future work may find interest in studying how changing certain qualities of the ligand such as the anchoring group or tail shape may affect solid-state mobility, as well as reduction and formation rates. Thiol-based ligands are commonly employed for AuNP syntheses but have thus far not been investigated in the solid state as simple long chain thiols akin to the long chain amines explored to date. It is likely that to study different metals in the solid state there will be a need to screen through a variety of different ligand shapes, sizes, and charges.

## 4.3 References

1. P. F. M. de Oliveira, A. A. L. Michalchuk, J. Marquardt, T. Feiler, C. Prinz, R. M. Torresi, P. H. C. Camargo and F. Emmerling, *CrystEngComm*, 2020, **22**, 6261-6267.

2. M. H. Hussain, N. F. Abu Bakar, A. N. Mustapa, K.-F. Low, N. H. Othman and F. Adam, *Nanoscale Res. Lett.*, 2020, **15**, 140.

3. F. Chen, G.-Q. Xu and T. S. A. Hor, *Mater. Lett.*, 2003, **57**, 3282-3286.

4. I. Ojea-Jiménez, F. M. Romero, N. G. Bastús and V. Puntes, *J. Phys. Chem. C*, 2010, **114**, 1800-1804.

5. V. Khare, Z. Li, A. Mantion, A. A. Ayi, S. Sonkaria, A. Voelkl, A. F. Thünemann and A. Taubert, *J. Mater. Chem.*, 2010, **20**, 1332-1339.

6. M. Y. Malca, H. Bao, T. Bastaille, N. K. Saadé, J. M. Kinsella, T. Friščić and A. Moores, *Chem. Mater.*, 2017, **29**, 7766-7773.

7. M. Y. Malca, MSc, McGill University, 2017.